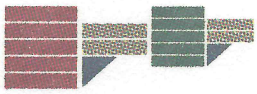

UNIVERSITÁ DEGLI STUDI DELLA CALABRIA

Scuola di Dottorato B. Telesio

Dottorato in:

Scienze e Tecnologie delle Mesofasi e dei Materiali Molecolari

ciclo XXIII°

TURBULENCE AND STOCHASTIC PROCESSES IN NEMATIC LIQUID CRYSTALS

PH.D. STUDENT:
FRANCESCO CARBONE

COORDINATOR:
PROF. CARLO VERSACE

SUPERVISOR:
DR. GIUSEPPE STRANGI

Francesco Carbone: *Turbulence and Stochastic Processes in Nematic Liquid Crystals*, Universitá degli Studi della Calabria, November, 2010.

E-MAIL:
francesco.carbone@fis.unical.it

Chi ha raggiunto lo stadio di non
meravigliarsi piú di nulla dimostra
semplicemente di aver perduto
l'arte del ragionare e del riflettere.

Max Planck

ABSTRACT

In this work we studied the electrohydrodynamics instabilities (EHD) from a different point of view. We used the traditional tools, belonging to the traditional fluid turbulence framework, to the world of liquid crystals. This tools in addition, for the first time, a 3D scanning of the NLC sample driven in these turbulent regimes, give us some interesting results. As an example a fragmentation of the large scale structures (Williams Domains) whit characteristics similar to the Richardson cascade. We also studied, for the first time, the intensity fluctuation at different depth z inside the sample, and we found a strong non gaussianity in the probability density function of this fluctuation. Further information has been obtained by by studying the decorrelation processes in EHD. We found a local transition between two different regimes: the classical Kolomokorov K41 law in the y direction, and a random sweeping decorrelation in the opposite x direction. Finally we study the weak localization of light obtained during the EHD. We found a drastic reduction in the scattering mean free path $\ell^\star$ and a strong enhancement of the backscattering cone.

SOMMARIO

In questo lavoro di tesi ci siamo occupati dello studo dei processi di electrohydrodynamics (EHD) da un punto di vista della turbolenza usuale. Utilizzando le tecniche classiche appartenenti al mondo della fluido dinamica e, per la prima volta, effettuando una scansione 3D del campione guidato in questi stai turbolenti, sono stati portai alla luce interessanti aspetti, ed analogie tra i due mondi. Un esempio é la frammentazione delle grandi scale (Williams Domains) in un modo simile alla cascata di Richardson. Inoltre, per l prima volta, sono state studiate le fluttuazioni di intensitá a diverse profonditá z all'interno del campione. Come risultato si é ottenuta una deviazione da una distribuzione gaussiana nelle densitd́i probabilitd́i quetse fluttuazioni. Altre interessanti informazioni sono state ottenute dallo studio dei processi di decorrelazione in EHD. Da questo studio si evince una transizione locale fra due regimi distinti: la classica legge K41 di Kolmorov nella direzione y, ed una decorrazione di typo random sweeping nella direzione opposta x. Infine sono state studiate le proprietá di localizzazione della luce di questi sistemi, ottenendo come risultato una drastica riduzione nel libero cammino medio di scattering $\ell^\star$ ed un forte aumento del cono di backscattering.

CONTENTS

1 PREFACE 1

2 LIQUID CRYSTALS 3
- 2.1 Anisotropy of Electric and Optical Properties of Liquid Crystals 5
- 2.2 Electric Field Effects in Nematic Liquid Crystals 8
  - 2.2.1 Deformation by an Electric Field 8
- 2.3 Continuum Theory for Deformation Induced by an Electric Field 9

3 TURBULENCE 13
- 3.1 What is Turbulence? 13
- 3.2 History of Turbulence 14
- 3.3 The Nature of the Turbulence Problem 16
- 3.4 Statistical Approach and Phenomenology 16
  - 3.4.1 Small-scales of Turbulence and Universality 17
  - 3.4.2 Structure Functions and Intermittency 17
  - 3.4.3 The Multifractal Model 18

4 ELECTROHYDRODYNAMICS INSTABILITIES IN NLC 21
- 4.1 Williams Domain and the Helfrich Interpretation 21
  - 4.1.1 Analytical Determination of the Threshold Voltage for the Williams Domains 23
  - 4.1.2 Frequency Dependence 24
  - 4.1.3 Extension to Higher Frequencies 24
- 4.2 Theoretical Consideration for Onset of Convection and Threshold Behavior in EHD 26

5 EXPERIMENTAL OBSERVATION OF EHD TURBULENCE 31
- 5.1 The Fragmentation Model 31
- 5.2 Evolution of EHD Instabilities 32
  - 5.2.1 Undulation, Zig-Zag, and Oblique Rolls 32
  - 5.2.2 The bimodal Structure (Rectangular cells) 33
  - 5.2.3 Remarks on the Nature of The Transition to the Bimodal 35
- 5.3 Transition to a Weak Turbulence Regime 35
- 5.4 The Dynamic Scattering Mode 2 36
- 5.5 Chaoticity? The Lyapunov exponents 39
  - 5.5.1 Lyapunov Exponent for the DSM2 40

6 CONFOCAL FLUORESCENCE MICROSCOPY OBSERVATION OF EHD 43
- 6.1 History 43
- 6.2 Modern Confocal Microscopy 44
  - 6.2.1 Fluorescence 44
- 6.3 Fluorescence Microscopy 45
- 6.4 How Does a Confocal Microscope Work? 46
- 6.5 3d Visualization 47
- 6.6 Other Consideration 48
  - 6.6.1 Resolution 48
  - 6.6.2 Pinhole Size 48

6.6.3 Intensity of Incident Light 49
6.6.4 Fluorophores 49
6.6.5 Photobleaching 49
6.7 Confocal Fluorescence Microscopy in EHD Instabilities 50
6.7.1 Clustering of Elastic Distortion Energy 51

7 ANOMALOUS SCALING OF INTENSITY FLUCTUATIONS DISTRIBUTION IN EHD 57
7.1 Intermittency 57
7.1.1 The PDF Within the K41 Framework 59
7.1.2 The PDF for a Simple Intermittency Model 59
7.2 Probability Density Function of Intensity Fluctuations 61
7.2.1 A Model for the Scaling Behavior of PDFs 62
7.3 Scaling of EHD Turbulence 62

8 THE PROPER ORTHOGONAL DECOMPOSITION 69
8.1 Basic Concepts 69
8.2 On Domains and Averaging 72
8.3 Proper Orthogonal Decoposition of EHD Turbulence 72

9 DECORRELATION PROCESSES IN EHD TURBULENCE 79
9.1 Straining and Sweeping Decorrelation Processes 80
9.2 Experimental Analysis of Decorrelation in EHD Turbulence 81

10 DYNAMICAL LOCALIZATION OF LIGHT IN NLC 87
10.1 Coherent Backscattering and Weak Localization of Light 87
10.2 A Simple Model for the CBS Description 88
10.3 The Cone Shape 90
10.4 Weak Localization in EHD Turbulence 91
10.4.1 CBS Experiments in EHD 92

11 CONCLUSION AND REMARKS 97

A PROPERTIES OF THE POD 103
A.1 Span of the Empirical Basis 103
A.2 Optimality 106
A.3 Symmetry 108
A.4 Attractors 110

B DIRECTED PERCOLATION 115
B.1 Directed Percolation at First Glance 115
B.2 Directed Percolation as a Stochastic Process 119
B.2.1 Basic Scaling Behavior 119
B.2.2 Universality and the DP Conjecture 120
B.2.3 Simple Mean-Field Approximation 121
B.2.4 Phenomenological Langevin Equation 122

BIBLIOGRAPHY 123

1 PREFACE

Processes related to light scattering in matter have a long history in physics, our understanding has progressed to a self consistent electromagnetic theory that incorporates all known physical processes related to interaction between radiation and matter. Light scattering experiments have enjoyed a renaissance since the invention of the laser and have gained further prominences as potential applications of quantum optics, nonlinear optical materials and photon localization. In the framework of Anderson's localization, the possibility of achieving photon localization in random materials has spurried interest in coherent backscattering of light. In particular, the self-interference effect which leads to an enhancement of the intensity cone in the backscattering direction, is a compelling topic in nonlinear optics. This property is not an interference due to the properties of single scattering event, but relies in the multiple scattering effect of light in a random medium.

The retro reflection enhancement of light can be also observed when a liquid crystal sample is subject to an oscillating electric field which induces electrohydrodynamic (EHD) instabilities. In this framework, investigating stochastic properties of this medium, can help us to better understand the dynamics of anisotropic coherent backscattering. The thesis mainly deals with the characterization of some properties of EHD instabilities as the intensity of the external electric field is varied. In this case, a sequence of spatio-temporal phenomena can be recognized and investigated in detail. In particular, as we will show, statistical properties of fluctuations rensemble some gross features of turbulence which has been investigated in usual fluid flows and sometime in complex flows like hydromagnetic medium. In this thesis we investigate these properties, as a first step towards a better determination of dynamical properties of EHD turbulence. However, as we will show, statistical properties of fluctuations in EHD instabilities are interesting in itself, because a liquid crystal drived by an oscillating electric field shows a richness of physical processes like universal scaling behavior, intermittency, fragmentation models and emergence of recurrent pattern. Yet, in this medium excellent experiments can be easily performed and, at variance to usual fluid flows, both spatial and temporal chaotic dynamics can be investigated in detail.

The plan of the thesis is as follows. In the first three Chapters I will introduce some basic information about the structure of liquid crystalline phases (Chapter 2), the physics of turbulence in usual fluid flows (Chapter 3) and the effects of electric fields on the dynamics of liquid crystals (Chapter 4). In Chapter 5 I investigate in detail some standard experiments on the dynamics of a Nematic Liquid Crystal (NLC) under the action of an externally imposed oscillating electric field. In particular the transition to a a turbulent dynamics where fluctuations of the transmitted intensity are observed at all scales, due to a sequence of bifurcations within Electro-Hydro-Dynamics (EHD) instabilities, is investigated. In Chapters 6 and 7 EHD instabilities are studied through confocal fluorescent microscopy observations, a technique which allows to measure intensity fluctuations on different planes inside the sample. This technique allows us to obtain three-dimensional information on the dynamics of fluctuations within the sample. We showed that the elastic distortion energy is strongly clusterized at higher applied voltages and can be described within the multifractal approach (Chapter 6), thus inducing anomalous scaling laws of the fluctuations of the transmitted intensity (Chapter 7). A model which is able to describe the anomalous scaling laws can be obtained from a fragmentation process, based on the fact that at high aplied voltages small-scale fluctuatons are generated. The presence of small-scales and their properties have been evidenced by using the Proper Orthogonal Decomposition on the spatio-temporal be-

havior of the transmitted light intensity (Chapter 8). The process leading to the presence of fluctuations, which is the main characteristic of turbulence, rapidly destroy correlations. The process of decorrelation in EHD turbulence is investigated in detail in Chapter 9. Almost surprisingly, measurements showed that the classical straining effect, introduced by Kolmogorov as the main physical process of decorrelation in classical turbulence, has been recovered at smaller voltages, while at higher voltages the physical decorrelation process seems to be mainly due to a random sweeping (Chapter 9). Finally, in Chapter 10 we present some experiments on the light backhscattering in EHD turbulence regimes, and in Chapter 11 some final remarks on the characterization of EHD turbulence in nematic liquid crystals.

2 LIQUID CRYSTALS

CONTENTS

2.1 Anisotropy of Electric and Optical Properties of Liquid Crystals 5
2.2 Electric Field Effects in Nematic Liquid Crystals 8
2.2.1 Deformation by an Electric Field 8
2.3 Continuum Theory for Deformation Induced by an Electric Field 9

Liquid crystals are liquids in which a definite ordered arrangement of molecules exists. In fact, even if the center of gravity of NLC molecules have no long-range order, the average molecular orientation tends to be parallel to a common axis, defined by a unit vector named molecular director $\mathbf{n}(\mathbf{r})$ (or the optic axis of the NLC). The characteristics of anisotropy, say differences of physical patterns in the parallel and perpendicular directions with respect to $\mathbf{n}(\mathbf{r})$, are reflected in all macroscopic tensor properties *i.e.* mechanical, electric, magnetic, and optical. The liquid-crystalline state arises under certain conditions in organic substances having sharply anisometric molecules, *i.e.*, molecules that have a clearly marked elongation in one of the directions, or are flat. A good example of such a substance is *p-methoxybenzylidene-p'-n-butylaniline*, abbreviated MBBA, which shows a liquid-crystalline phase of the simplest type (*nematic*) over a certain temperature range $T \in (294 - 320^\circ\ K)$.

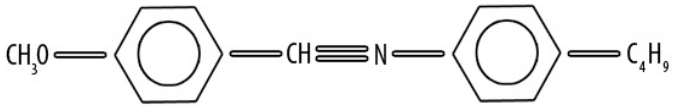

Nematic liquid crystals (NLC) are characterized by long-range orientational order and complete translational freedom of the centers of gravity of the individual molecules in space, as well as freedom of rotation of the molecules about their long (and sometimes also short) axes (see Fig. 1a, where the dashes denote the molecules of a NLC). A model of a nematic phase might be a pencil box that one gently shakes to imitate thermal motion: if one doesn't shake it very hard, the pencils shift around, but remain parallel to one another. Upon strong shaking, the box will contain complete disorder. The thermotropic[1] NLC behave similarly: they are usually solid crystals at low temperatures; a phase transition to a nematic state (*melting point*) occurs with rising temperature; and a second phase transition occurs at a still higher temperature to an isotropic-liquid state (*clearing point*). *Nematic liquid crystals*

Cholesteric liquid crystals (CLC) are a variety of nematic substances. Here also, orientational but not translational order exists. However, the CLC are formed by substances having optically active molecules (which rotate the plane of polarized light). The asymmetry of these molecules leads to a twisted structure in the liquid crystal. In Fig. 1b the solid dashes show the arrangement of molecules in the layer of the CLC closest to the observer, while the molecules in a deeper layer are rotated by a small angle ϕ with respect to the molecules *Cholesteric liquid crystals*

1 There are also lyotropic liquid crystals that are formed in concentrated (generally aqueous) solutions of certain dyes, soaps, biological materials, etc. Their optical properties have hardly been studied, [80] and we shall discuss henceforth only therotropic liquid crystals.

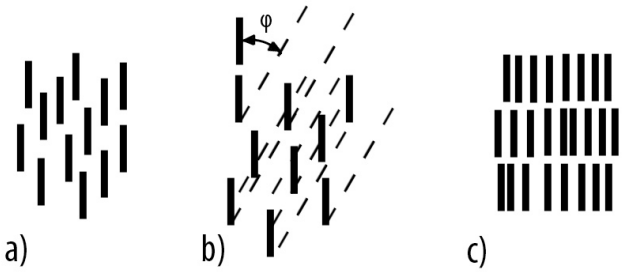

Figure 1: Structure of liquid crystals of the nematic a), cholesteric b), and smectic c) types.

of the first layer (this is shown by the dotted dashes). The angle ϕ increases for successive layers, and the specimen as a whole forms a helix with an axis perpendicular to the axes of the molecules and the plane of the drawing). Examples of substances that form CLC are the esters of cholesterol or the optically active isomers of compounds of the type: where the op-

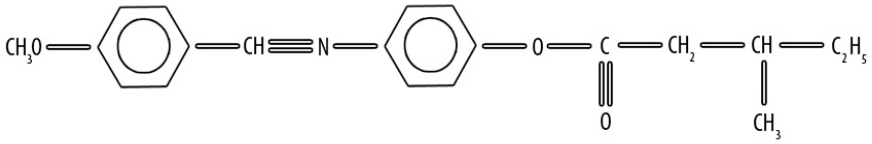

tical activity is caused by the asymmetric arrangement of the CH_3 groups in the long tail of the molecule (the temperature range of the cholesteric phase of this substance is $308-349^\circ$ K).

Smectic liquid crystals

A second important class of liquid-crystalline substances is the *smectic liquid crystals* (SLC), which are characterized by one-dimensional translational order as well as orientational order (Fig. 1c). A SLC is closest in structure to solid crystals, and in substances that form both a nematic and a smectic phase, it is not fortuitous that the sequence of phase changes upon lowering the temperature is:

$$\text{isotropic liquid} \rightarrow \text{NLC} \rightarrow \text{SLC} \rightarrow \text{solid crystal}.$$

An example is the following substance, with a range of existence of the metastable smectic phase of $334-08^\circ$ K:

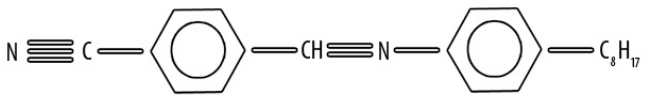

Liquid-crystalline phase formation

It is pertinent to ask what are the concrete substances that tend to form a liquid-crystalline state. People have tried repeatedly to devise a molecular-statistical theory of liquid crystals, i.e., infer their thermodynamic properties from the electronic structural features of the molecules. It is now generally thought that dispersion (van der Waals) attractive forces between the molecules and steric repulsive forces play defining roles in producing the liquid-crystalline state. The most important molecular characteristic that governs the tendency of

a concrete substance to form a liquid-crystalline state is anisotropy of electronic polarizability. In this sense, long, rod-like molecules with benzene molecules lying in a row are most favored. A positive factor is the existence of a conjugated chain (alternation of single and double chemical bonds) along the entire skeleton of the molecule, because the conjugation enhances the longitudinal component of the molecular polarizability. Apparently, existence of a permanent dipole moment in molecules is not correlated with ability of the substance to form liquid crystals, although it often determines their electric and electro-optical properties. The shape of the end groups of the molecules (the steric factor) is highly essential. For example, as a rule, the butyl group ($n^- C_4 H_9^-$) facilitates getting liquid crystals at very low temperatures: elongation of the end groups reduces the anisotropy of the polarizability, owing to "*twisting*" of the molecule, while shorter groups bind the molecules too rigidly, and thus raise the phase-transition temperature.

2.1 ANISOTROPY OF ELECTRIC AND OPTICAL PROPERTIES OF LIQUID CRYSTALS

Orientational order parameter

Quantitatively, the degree of order of a liquid crystal sample is defined by the orientational order parameter S introduced by Zwetkoff [1]:

$$S = \frac{3}{2}(\langle \cos^2 \theta \rangle - 1) \tag{2.1}$$

Here θ is the angle between the axis of an individual molecule of the liquid crystal and the preferred direction of the entire ensemble, while the averaging is performed both over the ensemble and over time. The preferred direction coincides with the optic axis of a liquid single crystal, and it must be fixed by an external factor (the wall of the cuvette, a field, or a flux). In line with the sense of the definition, the degrees of order are $S = 1$ for solid crystals and $S = 0$ for an isotropic liquid phase. In a liquid crystal, $0 < S < 1$, and S fully determines the anisotropy of the electric and optical properties. In particular, the anisotropy of the diamagnetic susceptibility, as well as the electronic part of the dielectric constant of a liquid nematic crystal, are determined in terms of the anisotropy of the same substances in the solid phase (*e.g.*, in *p-azoxyanisole*):

$$\begin{aligned} \Delta\chi_{NLC} &= \chi_{\parallel} - \chi_{\perp} = S\Delta\chi_{solid} \\ \Delta\alpha_{NLC} &= \alpha_{\parallel} - \alpha_{\perp} = S\Delta\alpha_{solid} \end{aligned} \tag{2.2}$$

More complicated relationships hold for the anisotropy of the refractive index ($\Delta n = n_{\parallel} - n_{\perp}$), which is connected to $\Delta\alpha$ by the Lorenz-Lorentz relation, for that of the total dielectric constant, which includes an orientational component ($\Delta\epsilon = \epsilon_{\parallel} - \epsilon_{\perp}$), and for the anisotropy of the electric conductivity ($\Delta\sigma = \sigma_{\parallel} - \sigma_{\perp}$). However, the general rule of monotonic decline is maintained for all of these quantities: Δn, $\Delta\epsilon$, $\Delta\sigma \to 0$ as $S \to 0$. The viscosity and elasticity of liquid crystals are also anisotropic.

Temperature dependence of physical properties

Figure 2a shows the typical temperature dependences of the order parameter S, of the refractive index measured with the direction of polarization of the light parallel ($n_{\parallel}$) and perpendicular ($n_{\perp}$) to the optic axis of a NLC, and of the electric conductivity for an electric field parallel ($\sigma_{\parallel}$) and perpendicular ($\sigma_{\perp}$) to the optic axis, and the analogously-defined components of the dielectric constant ($\epsilon_{\parallel}$ and $\epsilon_{\perp}$). We should note that $\Delta n > 0$ in all known NLC and SLC, in line with the anisotropy of the electronic polarizability of the molecules. Yet the sign of $\Delta\sigma$ differs for NLC and SLC in agreement with the anisotropy of the viscosity, which determines the anisotropy of mobility of the charge carriers. In a NLC (with rare exceptions [2]), $\Delta\sigma > 0$, because the charge carriers migrate more readily in the direction of

the long axes of the molecules. Conversely, in a SLC the mobility of the charge carriers is higher in a direction along the smectic layers, *i.e.*, perpendicular to the axes of the molecules, and hence $\Delta\sigma < 0$.

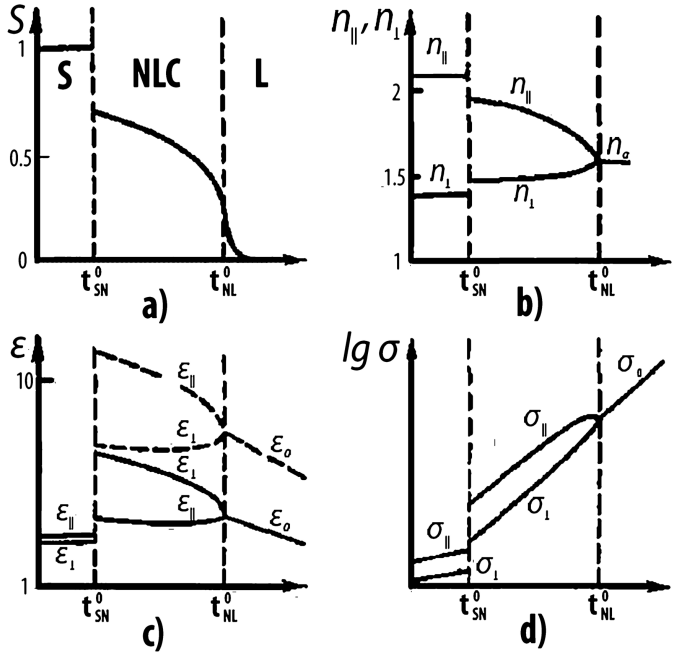

Figure 2: Characteristic temperature dependence of order parameter S a), refractive index n b), dielectric constant ϵ c), and the electric conductivity σ d) of NLC. t^0_{SN} and t^0_{NL} are the temperatures of the phase transition solid $\rightarrow$ NLC and NLC $\rightarrow$ isotropic liquid respectively [3].

Dielectric anisotropy

The dielectric anisotropy of liquid crystals can be either positive (dotted curves in Fig. 2c) or negative (solid curves in Fig. 2c). This depends on the relationship between the anisotropy of polarizability of the molecule and the value of the permanent dipole moment, and also on the angle Φ between the dipole moment and the long molecular axis. A positive $\Delta\epsilon$ is characteristic of molecules having a longitudinal dipole moment ($\Phi \rightarrow 0$); $\Delta\epsilon < 0$ happens when the angle Ψ is large, *e.g.*, $\Psi \rightarrow 90°$. Figure 3 gives the frequency-dependences of $\epsilon_\parallel$ and $\epsilon_\perp$ for two typical NLC that have $\Delta\epsilon(\omega \rightarrow 0) > 0$ (Fig. 3a) and $\Delta\epsilon(\omega \rightarrow 0) < 0$ (Fig. 3b). We see that the sign of $\Delta\epsilon$ can change in the frequency range of Debye dipole relaxation, and as will be shown below, this is just what determines the electrooptical behavior of liquid crystals.

External field effects

Any process of switching of NLC optical properties by an external electric field is divided into three stages:

1. Owing to the anisotropy of the dielectric constant and of the electrical conductivity, a liquid mono-crystal (analogously to a solid crystal) will experience a torque that tends to reduce the energy of the anisotropic object in the electric field. For example, when $\sigma = 0$, the crystal tends to rotate in such a way that the direction of the maximum dielectric constant coincides with the direction of the field.

2. Owing to the relatively small viscosity and internal friction of the liquid, the torque actually reorients the liquid mono-crystal in a relatively short time (this would not happen with solid crystals because of the frictional forces).

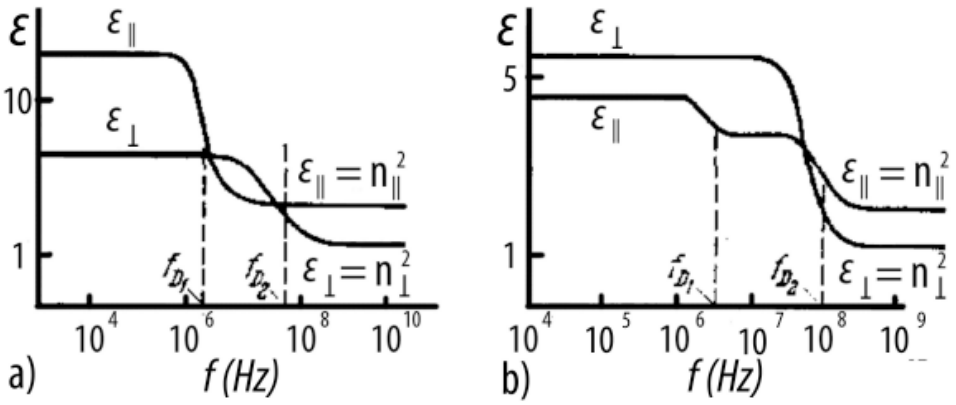

Figure 3: Typical frequency dependences of the dielectric constant of NLC for $\Delta\epsilon > 0$ a) and $\Delta\epsilon < 0$ b). The Debye relaxation frequencies differ for rotation of the molecules about the short (f_{D_1}) and long(f_{D_2}) axes [3].

3. Owing to the large anisotropy of the optical properties (the refractive indices and the absorption coefficient), any change in the structure of the specimen is easily established optically, in full analogy with the properties of solid crystals.

2.2 ELECTRIC FIELD EFFECTS IN NEMATIC LIQUID CRYSTALS

Early studies

The first studies of the effect of an electric field on NLC were carried out as early as 1918 [4]. In this and in subsequent studies of the twenties and thirties [5], fundamental attention was paid to the mechanism of orientation of NLC by an electric field and the interpretation of this phenomenon on the basis of the theory of *"dipole swarms"*, which has now lost currency. At that time, optically transparent electrodes had not yet been invented, and this greatly hampered electro-optical experimentation with thin layers of NLC. Freedericksz and Zwetkoff [6] carried out very reliable experiments by using polarized light and wire net electrodes. Unfortunately, these studies have been little cited in the articles of the sixties and the seventies, although they anticipated many of the ideas that the modern theory and applications of the electro-optical effects are based on. Thus, in [6] they describe the intense movement ("*boiling*") of a NLC of *p-azoxyanisole* in low-frequency fields, which is accompanied by strong light scattering, *i.e.*, in essence a "*dynamic scattering effect*", which was discovered anew in 1968 [7, 8].

Frequency dependence, threshold phenomena

They also showed in [6] that there was a critical frequency of the field above which movement vanished, and that the threshold voltage is *independent* of the thickness of the layer of liquid crystal. They noted [6] the role of space charge and the orientational action of the flow of the liquid in the mechanism of anomalous orientation of a NLC having negative dielectric anisotropy. And finally, an important criterion for electrohydrodynamic instability of a NLC was first formulated in [6], namely that $\Delta\epsilon < 0$, as is shown experimentally by varying the size and sign of $\Delta\epsilon$ by adding *methoxycinnamic acid* to *p-azoxyanisole*.

2.2.1 Deformation by an Electric Field

Sample cell fabrication

The basis of practically all experimental studies of the electric fields effects on liquid crystals (nematic, cholesteric, and smectic) is the thin-film cell (Fig. 4a) of thickness $d = 5 \div 100$ μm with two transparent electrodes 1 (usually an *ITO* deposition) on glass substrates 2.

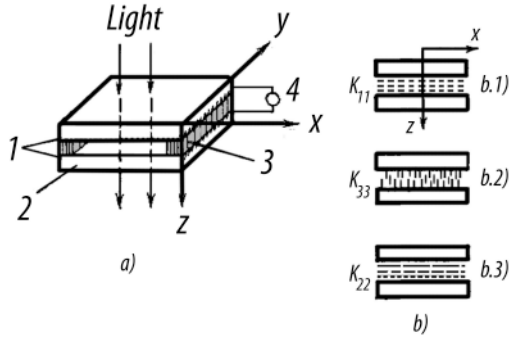

Figure 4: a) Sketch of a sample NLC cell, b) different cases of deformation of a NLC: b1) S-deformation, b2) B-deformation, and b3) T-deformation.

There is a capillary gap between the electrodes that is fixed by dielectric spacers 3. One can apply to the electrodes a d.c, sinusoidal, or pulsed voltage 4. In order to study the NLC distortion induced by an electric field, a polarized light wave[a], or in a number of cases a monochromatic light wave, can be employed. The light front passes through the sample along the z axis and sense the deformation of the director field which is in related to Δn.

a Usually this step can be performed using a traditional optical microscope.

Depending on the sign of the dielectric anisotropy and the initial orientation[2] of the molecules of the NLC, one can observe three varieties of deformations:

Splay deformation

1. $\Delta\epsilon > 0$: while the initial orientation of the molecules (Fig. 4b.1) is characterized by an arrangement of $\mathbf{n}(\mathbf{r})$ parallel to the electrodes ($\mathbf{n}(\mathbf{r}) \perp z$). Then the layer of NLC shows

2 The molecular alignment is due to a deposition of a polymeric surfactant on the ITO-glass substrate.

birefringence with the definite value Δn. The electric field acts against the elastic force of interaction of the molecules with the wall to give rise to a "*transverse bending*" deformation of the NLC (S-deformation, also known as *splay*), which is characterized by the elastic modulus K_{11} [9]. If the field is strong enough, the reorientation is along the z axis, and the birefringence vanishes ($\Delta \to 0$). This effect is known as *S-effect* [10, 11].

2. $\Delta\epsilon < 0$: while the arrangement of the molecules is perpendicular to the electrodes direction ($\mathbf{n}(\mathbf{r}) \parallel z$) in the initial state (Fig. 4b.2). In this case the birefringence vanishes, but reappears when the field is applied to the layer of liquid crystal. The field tends to set the director $\mathbf{n}(\mathbf{r})$ perpendicular to the z axis (because $\Delta\epsilon < 0$). In some cases (*e.g.*, with the additional application of a magnetic field or special treatment of the electrode), it tends to set it along a definite direction x or y. The consequent "*longitudinal bending*" deformation is characterized by the elastic modulus K_{33} [9] (B-deformation, also known as *bend* deformation [12], deformation of a vertical aligned phase). We shall call this effect the *B-effect*. *Bend deformation*

3. A third type of deformation arises when $\Delta\epsilon > 0$ and the initial orientation is $\mathbf{n}(\mathbf{r}) \parallel x$ at one electrode and $\mathbf{n}(\mathbf{r}) \parallel y$ at the other (Fig. 4b.3)*. Consequently the NLC acquires an optically-active structure twisted by one-fourth turn. This structure rotates the plane of polarization of the transmitted light beam by exactly 90° [13]. The electric field tends to set the director along the axis z ($\Delta\epsilon > 0$), giving rise to a deformation in which the rotational elastic modulus K_{22} plays an important role[3] (T-deformation, also known as *twist* deformation) [9]. The optical activity vanishes after the NLC has become reoriented; the corresponding effect is called the twist effect (the *T-effect* in our classification). *Twist deformation*

$\star$ We can also imagine a reverse twist effect for the case of the orientation $\mathbf{n}(\mathbf{r}) \parallel z$ and $\Delta\epsilon < 0$, with special preparation of the glass substrate for a preferential orientation of the NLC in the electric field along x at one electrode and along y at the other. However, such an effect has not been described in the literature [3].

2.3 CONTINUUM THEORY FOR DEFORMATION INDUCED BY AN ELECTRIC FIELD

The theory of deformation of a NLC by an electric field and the birefringence calculation [10, 11, 14] have been constructed by analogy with the treatment of the deformation of a NLC by a magnetic field [15]. The difference consists in the fact that we cannot consider the anisotropy of the dielectric constant to be small in comparison with the mean dielectric constant [10, 11, 14], as happens with the magnetic analog. The way to perform the calculation is: first one writes the expression for the free energy of the liquid crystal F as a function of the molecular director $\mathbf{n}$ of the director and the electric field E (in the CGSE system): *Free energy density functional*

$$F = \frac{1}{2}\int \left\{ K_{11}(\nabla \cdot \mathbf{n})^2 + K_{22}(\mathbf{n}\nabla \times \mathbf{n})^2 + K_{33}(\mathbf{n} \times \nabla \times \mathbf{n})^2 - \frac{\Delta\epsilon}{4\pi} E(\mathbf{n})^2 \right\} dv, \tag{2.3}$$

Here $\Delta\epsilon = \epsilon_{\parallel} - \epsilon_{\perp}$, while we have discussed the meaning of the elastic constant K_{ii} in section 2.2.1.

3 This modulus characterizes the pure torsional deformation that would arise in the layers next to the wall in an electric field rotating about the axis z.

Then we solve the Euler's equation corresponding to the functional F, with account taken of the boundary conditions (the different cases of initial orientation of the NLC). We get thereby the steady-state solution that relates the orientation angle θ of the director to the coordinate along the z axis (see Fig. 4) and to the external field. Here it turns out that the process of reorientation of the liquid crystal shows threshold[4] behavior, and the voltage $V^\star$ across the cell at which reorientation begins is determined by the expression

Threshold voltage for the reorientation process

$$V^\star = \pi\sqrt{\frac{4\pi K_i}{\Delta\epsilon}}, \tag{2.4}$$

where for an initial S-orientation (the system is prepared in a situation of S-deformation 4b.1) $K_i = K_{11}$, $K_i = K_{33}$ for a B-orientation (Fig. 4b.2), and $K_i = K_{11} + {}^1/_4(K_{33} - 2K_{22}$ [16] for a T-orientation (Fig. 4b.3).

It's easy to understand the meaning of eq. 2.4 from simple physical notions: reorientation begins at the voltage $V^\star = E_0 d$ (where d is the sample thickness) at which the density of electrostatic energy $\Delta\epsilon E/8\pi$ gained by reorientation matches the energy $Kq_1^2/2$ spent for drive the system to the "*smoothest*" of all the possible deformations under the given boundary conditions in the cell. This deformation is characterized by a Fourier component having a minimum ($m = 1$) value of the wave vector $q_m = m\pi/d$ (with $m = 1, 2, \dots$). The condition $\Delta\epsilon E^2/8\pi = K\pi^2/2d^2$ implies that the threshold voltage for reorientation of the NLC is independent of the thickness of the cell (eq. 2.4).

Distribution of the refractive index and phase difference

As result of Eq. 2.3 we have an expression for the orientation angle of the optic axis $\theta(z)$ as a function of the field. In this way we find the distribution of the refractive index across the thickness d:

$$n(z) = \frac{n_\perp n_\parallel}{\sqrt{n_\perp^2 \cos^2\theta(z) + n_\parallel^2 \sin^2\theta(z)}}, \tag{2.5}$$

and then we find the phase difference between the ordinary and extraordinary $\Phi(E)$ at the exit face of the sample cell, which depends as a parameter on the field intensity E, in terms of $\theta(z)$ [11]:

$$\Phi(E) = \frac{2\pi}{\lambda}\int_0^d n(z)dz = \frac{2\pi d\langle\Delta n(E)\rangle}{\lambda}. \tag{2.6}$$

It's interesting to notice that the amount of phase retardation determines the intensity of the light transmitted through the cell and analyzer:

$$I = I_0 \sin^2 2\beta \cdot \sin^2\left(\frac{\Phi}{2}\right), \tag{2.7}$$

where I_0 is the intensity of linearly polarized light incident on the cell, and β is the angle between the polarization vector of the incident ray and the optic axis ($\mathbf{n}(\mathbf{r})$) of the NLC. Depending on the voltage of the steady-state (d.c. or sinusoidal) electric field, and hence on the phase retardation $\Phi(E)$, the light intensity at the output of the analyzer have an oscillating behavior[5].

Time switching of the deformation effects

In order to study the transition processes of switching on and off of the deformation effects, we must solve the equation of motion for the molecular director [18], in which the viscous frictional torque (the left-hand side) is equated to the sum of the dielectric and elastic torques (the case E = 0 has been treated in [10, 11, 14]):

$$K_i\frac{\partial^2\theta}{\partial z^2} - \gamma_1\frac{\partial\theta}{\partial t} + \frac{\Delta\epsilon E^2}{4\pi}\theta = 0 \tag{2.8}$$

4 As discussed in section 2.2 the threshold for the reorientation process is independent from the sample thickness d.

5 From numerical calculations the maximum amplitude of the oscillations corresponds to $\beta = 45°$ [10, 11, 14, 17].

Here K_i is the elastic coefficient, which depends on the boundary conditions for $z = 0$ and $z = d$, as in Eq. 2.4, and γ_1 is the corresponding viscosity coefficient.

Solving the Eq. 2.8, we find an expression for the characteristic time τ for the on, and off, switching of the deformation effects:

$$\tau_{rise} = \frac{\gamma_1}{(\Delta\epsilon E^2/4\pi) - K_i(\pi^2/d^2)} = \frac{4\pi\gamma_1 d^2}{\Delta\epsilon V^2 - 4\pi^3 K_i} \tag{2.9}$$

$$\tau_{decay} = \frac{\gamma_1 d}{\pi^2 K_i} \tag{2.10}$$

Thus the τ_{decay} time is determined only by the viscoelastic properties of the NLC and the geometry of the sample cell, while τ_{rise} declines in inverse proportion to the square of the voltage ($V^2 = E^2 d^2$) when $V^2 > 4\pi^3 K_i/\Delta\epsilon$.

3 TURBULENCE

CONTENTS

3.1 What is Turbulence? 13
3.2 History of Turbulence 14
3.3 The Nature of the Turbulence Problem 16
3.4 Statistical Approach and Phenomenology 16
3.4.1 Small-scales of Turbulence and Universality 17
3.4.2 Structure Functions and Intermittency 17
3.4.3 The Multifractal Model 18

Turbulence is a omnipresent phenomenon of Nature. In our everyday life, we either rarely notice it when swimming, driving a car, riding a bike, skating, or suddenly pay serious attention to it, when the ride gets bumpy on board a plane on stormy weather or when flying over tall mountains.

Let us imagine for a second how the early morning cup of coffee would be without it. If it weren't for the beneficial effects that come with turbulence, mixing milk and coffee would become a very tricky process. Instead of thoughtlessly stirring it with the spoon once and then wait shortly for turbulence do the rest of the work, we would have to repeat the process many times such that the fluid would be sufficiently folded over itself and the milk evenly split over the cup. Of course, there is the alternative of not touching the cup for some time and let the milk slowly diffuse, but then coffee is not enjoyable anymore when it gets cold.

However, designing the most effective method of stirring coffee is not why turbulence is important to science. Actually, the diversity of situations where we discover turbulence as an important scientific phenomenon is impressive: flow around ships and aircrafts, combustion in car engines and plane turbines, flow in the ocean, atmosphere, air flow in lungs, flow of blood in arteries and heart, flow in pipelines, even the dynamics of the financial markets can also be viewed as analogous to turbulent flows. The entire Universe appears to be in a state of turbulent motion, and turbulence seems to be a decisive factor helping in the formation of stars and solar systems, as indicated by astronomical observations and theoretical considerations in astrophysics.

From the large variety of situations mentioned above, many of them are cases in which turbulence is attractive from the point of view of the engineer, since studying it leads to technological improvement. It is more fruitful then to model regions where the turbulent flows interact with boundaries, and then learn how to control and apply them.

For the physicist, the interesting part is how the small-scale structure of turbulence is organized, preferably isolated from any boundary effects. This is where universal aspects can be sought, in the sense that they should be independent of the nature of the fluid or the geometry of the problem. It is universality that makes turbulence an exciting research subject for physicists and mathematicians.

3.1 WHAT IS TURBULENCE?

The word *turbulent* is used in the everyday experience to indicate something which is *not* *The origin of the word*

regular. It appears that Leonardo Da Vinci was probably the first to distinguish this special state of the fluid motion and use the term turbulence 5. In fact the word derives from the italian *turbolenza*, or better from the Latin *turba* which means something confusing or something which does not follow an ordered plan. For example, a *turbulent boy*, in all Italian schools, is a young fellow who rebels against ordered schemes. Following the same line, the behavior of a flow which rebels against the deterministic rules of classical dynamics is called turbulent. Anyhow, even without the aid of a laboratory experiment and a Latin dictionary, we experience turbulence every day. Despite of being such a familiar notion, the real investigation of turbulence is relatively new, as Hinze clarifies in his textbook. Osborne Reynolds himself, a pioneer in the study of turbulence, called it *sinuous motion*. Skipping over the dictionary definition, which does not suffice to characterize the modern physical sense of the word, we stop at the definition given in 1937 by Taylor and Von Kármán: "*Turbulence is an irregular motion which in general makes its appearance in fluids, gaseous or liquid, when they flow past solid surfaces or even when neighboring streams of the same fluid past or over one another*". To make this more clear, we need to use the terminology of fluid dynamics. Flows of gases and liquids can be divided into two very different types: *laminar* flows[1], which are smooth and regular, and turbulent, totally opposite, in which physical quantities as velocity, temperature, pressure, etc. fluctuate in a sharp and irregular manner in space and time, the latter being actually the more natural state of a flow. The variety of time-scales and amplitudes of the velocity seen in this picture illustrates the complexity of turbulence structure. It is this structure that makes turbulence very efficient in transferring momentum and therefore an interesting subject for practical applications, such as delaying the boundary layer separation, which decreases drag forces on objects submerged in a turbulent flow.

The sinuous motion

The modern definition

Laminar flow and turbulent flow

3.2 HISTORY OF TURBULENCE

Modern turbulence started with the experiments of Osborne Reynolds in 1883, who analyzed the conditions under which laminar flows of fluids in pipes become turbulent. The study led to a criterion of dynamical stability based on the *Reynolds number*

Reynolds number

$$\mathrm{Re} = \frac{vl}{\nu}, \tag{3.1}$$

where v and l are the characteristics velocity and length scales of the flow and ν is the kinematic viscosity. The Reynolds number may be interpreted as the ratio of inertial to viscous forces present in the fluid, and for an incompressible flow, it is the only control parameter of that system. Intuitively, as Frisch points out in his book on turbulence [78], its value can also be seen as an indicator for the degree of symmetry of the flow. This can easily be imagined in the experimental situation of a flow past a cylinder. For values of the Reynolds number departing from $\mathrm{Re} \sim 1$, visualizations of the flow show a gradual increase of the degree of asymmetry in the flow surrounding the obstacle, before and after it. Based on the technological interest raised by the remarkable momentum transfer properties of the large scales of turbulence, experiments in the beginning of the 20th century led to decisive advances in the theory of turbulence. Representative of this time are the so-called semi-empirical approaches made by great fluid-dynamicists, such as G. Taylor, L. Prandtl and T. Von Kármán in the 1920s and '30s, which were used to solve important practical problems. In a remarkable paper, Lewis Fry Richardson advanced in 1922 the assumption that turbulence is organized as an hierarchy of eddies of various scales, each generation borrowing energy from its immediately larger neighbor in a *cascade* process of *eddy-breakdown*. This picture,

The Richardson cascade

1 It is interesting to note that even the opposite of a turbulence motion, namely a *laminar* motion, derives from the Latin word *lámina*, which means stream or sheet, and gives the idea of a regular streaming motion.

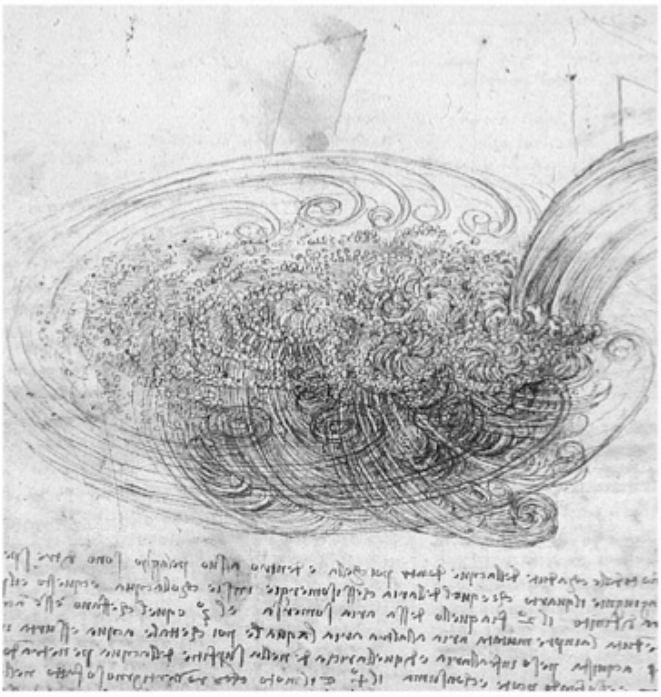

Figure 5: Drawing of a turbulent eddy by Leonardo da Vinci.

though more appropriate in wavenumber space, was poetically immortalized in his book inspired from observation of clouds and the verses of Jonathan Swift: *"Big whorls have little whorls, Which feed on their velocity; And little whorls have lesser whorls, And so on to viscosity (in the molecular sense)*".

The Kolmogorov description

This era culminated with the now fundamental ideas of Andrei Nikolaevich Kolmogorov in the *theory of locally isotropic turbulence* (K41 theory). Inspired by Richardson's energy cascade description, he assumed that with each step in the energy transfer towards smaller scales, the anisotropic influence of the large scales will gradually be lost, such that at sufficiently small scales the flow will be statistically homogeneous and isotropic. This steady situation, characterized by a mean flux of energy $\langle\epsilon\rangle$, was postulated by Kolmogorov to be universal and determined by only one parameter, $\langle\epsilon\rangle$. Moving further down the scales, there comes a length-scale where the flow gradients are so large that viscous effects can no longer be ignored. The scale is determined (in a dimensional argument) from the viscosity ν and $\langle\epsilon\rangle$

$$\eta = \left[\frac{\nu^3}{\langle\epsilon\rangle}\right]^{1/4}. \tag{3.2}$$

The self-similarity hypotheses

We introduce below the famous self-similarity hypotheses in their original form:

- At sufficiently large Reynolds numbers there is a range of high wave-numbers (inertial-range) where the turbulence is statistically in equilibrium and uniquely determined by the parameters $\langle\epsilon\rangle$ and ν. This state of equilibrium is universal.
- If the Reynolds number is infinitely large, the energy spectrum in the inertial range is independent of ν and solely determined by the parameter $\langle\epsilon\rangle$.

3.3 THE NATURE OF THE TURBULENCE PROBLEM

The equation of motion for the fluids flow: forcing and dissipation

The equations that govern turbulence are essentially a form of Newton's law for the motion of a fluid that is forced (at large scales) and affected by viscous dissipation (at small-scales)

$$\frac{\partial v(\mathbf{r},t)}{\partial t} + v(\mathbf{r},t)\cdot\nabla v(\mathbf{r},t) = -\frac{1}{\rho}\nabla p(\mathbf{r},t) + \nu\nabla^2 v(\mathbf{r},t) + F(\mathbf{r},t) \tag{3.3}$$

Here $v(\mathbf{r},t)$ denotes the velocity field at position $\mathbf{r}$ at time t, $p(\mathbf{r},t)$ the pressure, $F(\mathbf{r},t)$ the forcing, ρ is the density and ν is the kinematic viscosity.

The Eq. 3.3 is known as the Navier-Stokes equation, after the physicists who added the viscous term $\nu\nabla^2 v(\mathbf{r},t)$, C.L.M.H. Navier in 1827 and G.G. Stokes in 1845. Through this term, the kinetic energy is no longer conserved, but lost to heat.

The Navier-Stokes equation is a continuum equation. Later on we will learn that in 3-dimensional turbulence fluid motion occurs on smaller and smaller scales if the Reynolds number increases. Still, it can be proven that these scales will never be so small that the scale of molecular graininess of of the fluid is reached.

Deterministic chaos

Given an initial state of the flow field, together with the prescription of $v(\mathbf{r},t)$ at the boundaries, Eq. 3.3 suggests that the evolving field $v(\mathbf{r}, t > 0)$ is deterministic. However, we are uncertain about the uniqueness of the solution and therefore cannot characterize the phenomenon of turbulence as deterministic chaos. Moreover, the number of degrees of freedom of a turbulent flow is extremely large, which warrants a statistical rather than a deterministic description. The immense magnitude of the number of degrees of freedom N precludes the performance of direct numerical simulations of turbulent flows that can readily be made in the laboratory. With the number N increasing as $Re^{9/4}$, it will take many decades in the evolution of large-scale computing before the experiments of this thesis can be numerically simulated.

Understanding the problem

Understanding the nature of the turbulence problem is however a different story. What we need is "*a method of understanding the qualitative content of equations*" (Feynman 1963). Though it may seem rather pessimistic, Tsinober (2000) notes that there "*is no consensus on what is (are) the problem(s) of turbulence and what would constitute its (their) solution. Neither is there agreement on what constitutes understanding*". However, there seems to be agreement on what the culprits for this situation are:

- Nonlinearity - the term $v_i\partial_i v_j$
- Existence and smoothness of solutions at all time
- Non-locality - to determine the local fields one has to integrate over the entire space.

A more rewarding approach to deal with the extreme complexity of turbulence is a statistical description. The Kolmogorov statistical hypotheses form the starting point of the present thesis. In fact, a major effort will be to prove that the first hypothesis needs serious amendment.

3.4 STATISTICAL APPROACH AND PHENOMENOLOGY

In principle, the phenomenology of turbulence is characterized by simple statistical quantities, such as averages, probability distribution functions, spectra, correlations, etc., which are calculated from data experimentally measured or from direct computer simulations. In general, the term *averaging* is never equivalent to a proper ensemble average (over all possible states of the system), but ergodicity is invoked to replace it by time-averaging or mixed time and limited spatial averaging. These tools are sufficient to reveal some of the most important universal features of turbulence.

3.4.1 Small-scales of Turbulence and Universality

While turbulence at large Reynolds numbers consists of a wide range of dynamical scales that contain its energy, they are bounded naturally by a largest scale at which turbulence is stirred, and a smallest scale η, defined in Eq. 3.2, where most of the energy is dissipated. By small scales we will understand the dissipative range close to η and the inertial range postulated by the first Kolmogorov hypothesis (a). Phenomenological studies of turbulence are mostly aimed at the study of the small scales, since it is here that universal properties of turbulence are seen, and their characterization is considered important for the turbulence problem.

Isotropic and homogeneous turbulence

The second hypothesis of Kolmogorov (b) implies that small-scale turbulence is *isotropic and homogeneous* at sufficiently large Reynolds numbers, and its statistics will be determined only by the average dissipation rate

$$\langle \epsilon \rangle = \frac{\nu}{2} \sum_{i,j=1,}^{3} \left\langle \left(\frac{\partial v_i}{\partial x_j} + \frac{\partial v_j}{\partial v_i} \right)^2 \right\rangle \tag{3.4}$$

where ν is the fluid viscosity. If we consider the histogram of the fluctuations of normalized velocity increments over a small-scale separation $\Delta v(r)/(r\langle \epsilon \rangle)^{1/3}$, it follows then from (b) that this statistical quantity should be *universal*, i.e. independent of the flow, Reynolds number or r.

3.4.2 Structure Functions and Intermittency

One of the most common statistical quantities used in the phenomenology of turbulence is the structure function. We define the structure function of order p to be

$$S_p(r) = \langle \Delta v(r)^p \rangle = \int_{-\infty}^{\infty} P_r(\Delta v) \Delta v^p \, d(\Delta v), \tag{3.5}$$

where Δv are the velocity increments and $P_r(\Delta v)$ is their probability distribution function. The postulated universality of the normalized $P_r(\Delta v/(r\langle \epsilon \rangle)^1/3)$ implies that structure functions exhibit scaling behaviour for high Reynolds numbers

$$S_p(r) = C_p(r\langle \epsilon \rangle)^{1/3}), \tag{3.6}$$

when the separations r are within the inertial range, with C_p universal constants. The values of the scaling exponents $\xi_p = p/3$ follow from the postulate. The equivalent form of the above relation for order $p = 2$ gives the well-known scaling law for the energy spectrum

$$C\langle \epsilon \rangle^{2/3} k^{-5/3}. \tag{3.7}$$

The Kolmogorov 4/5 law

The only known exact relation for structure functions can be derived directly from the Navier-Stokes equations, namely the Kolmogorov $4/5$ law

$$S_3^L(r) = -\frac{4}{5}\langle \epsilon \rangle r. \tag{3.8}$$

Deviation from the K41 law: intermittency

For high orders $p \geqslant 4$, it is well-known the that scaling exponents ξ_p deviate from the Kolmogorov dimensional prediction, that is $\xi_p < p/3$. These deviations are known as anomalous scaling and imply that the form of the probability distributions $P_r(\Delta v)$ will vary inside the inertial range, such that with the decrease of the scale towards the dissipative range, their tails will be increasingly flared out. This phenomenon is called intermittency and the

anomalous scaling is a measure of it, since higher orders emphasize increasingly larger velocity excursions $\Delta v(r)$. To account for intermittency, the refined versions of the self-similarity hypotheses were proposed by Kolmogorov (1962), which incorporated the suggestion of Obukov that the mean energy dissipation rate exhibits strongly non-Gaussian fluctuations. In the case of anomalous scaling, one defines a local mean dissipation rate

$$\epsilon_r(\mathbf{r}, t) = \int_{V_r} \epsilon dV, \tag{3.9}$$

such that its own scaling exponents

$$\langle \epsilon \rangle^p \sim r^{\tau_p}, \tag{3.10}$$

will contribute to the new scaling

$$\langle \Delta v^p(r) \rangle = C'_p (\langle \epsilon \rangle r)^{p/3} \tag{3.11}$$

with exponents

$$\xi_p = p/3 + \tau_p \tag{3.12}$$

The failure of the Kolmogorov theory

Implicitly, the constants C'_p lose their universality (the famous *Landau objection*, originally formulated in 1944). The failure of the Kolmogorov theory to explain the anomalous scaling does not stop here however. Continuous improvement of experiments on intermittency brings increasing evidence that a description of turbulence beyond the Kolmogorov formulation, which dominated the turbulent research for more than half a century, is acutely needed. A number of intermittency models were proposed, which attempt to explain in particular the anomalous scaling exponents. The most popular model to explain the anomalous scaling exponents is the multifractal model of Frisch (the β-model 1985).

3.4.3 The Multifractal Model

The fractal description

In the Richardson cascade picture, when a mother-eddy breaks up into smaller daughter eddies, they uniformly occupy the entire space. In the fractal description, the resulting eddies will occupy only a fraction $0 < \beta < 1$ of the initial volume. Therefore, the fraction of the space that remains active at scale r (after some n breakdowns of the largest eddies r_0) is

$$p_r = \beta^n = \left(\frac{r}{r_0}\right)^{3-D} \tag{3.13}$$

Here the notation $3 - D$ justifies the interpretation of D as a fractal dimension. Then the energy flux (per unit mass) at scale r is

$$\Pi \sim \frac{E_r}{t_r} \sim p_r \cdot \frac{v_r^2}{t_r} = \frac{v_r^3}{3} \left(\frac{r}{r_0}\right)^{3-D} \tag{3.14}$$

which in the inertial range should not depend on the scale and therefore can be computed at the large energy injection scale

$$\langle \epsilon \rangle \sim \frac{v_0^3}{r_0} \tag{3.15}$$

The two relations 3.14 and 3.15 lead to a scaling exponent for the velocity field

$$v_r \sim v_0 \left(\frac{r}{r_0}\right)^h \tag{3.16}$$

The multifractal description

where $h = (1/3) - (3 - D)/3$. If rather than being single valued, the turbulent flow is assumed to possess a continuous range of scaling exponents h, then for each h there is a set $S_h \in R^3$ of fractal dimension $D(h)$ in which the velocity scales with this exponent. When we sum over all sets to compute the total scaling of the structure function

$$\frac{S_p(r)}{r_0^p} \sim \int d\mu(h) \left(\frac{r}{r_0}\right)^{ph+3-D(h)} \tag{3.17}$$

where $\mu(h)$ reflect the different weight of different fractal sets. In the limit $r \to 0$, the power-law with the smallest exponent will dominate, such that the scaling exponent of the structure function will be

$$\xi_p = \inf_h [ph + 3 - D(h)] \tag{3.18}$$

irrespective of the weights. It can be seen that the dimensions $D(h)$ and the scaling exponents are related by a Legendre transform, such that the inverse

$$D(h) = \inf_h [ph + 3 - \xi_p] \tag{3.19}$$

can be used to experimentally measure the deviations of the fractal dimension $D(h) \leqslant 3$ from the scaling exponents. So far, the multifractal model does not explain the anomalous scaling exponents, other than stating that anomalous scaling is equivalent to a non-trivial value of the multifractal dimension function $D(h)$. However, it is possible to construct more explicit models which do predict numerical values of the scaling exponents. One example is the log-Poisson model by She and Leveque, which reproduces the scaling exponents that are measured experimentally.

4 ELECTROHYDRODYNAMICS INSTABILITIES IN NLC

CONTENTS

4.1 Williams Domain and the Helfrich Interpretation 21
4.1.1 Analytical Determination of the Threshold Voltage for the Williams Domains 23
4.1.2 Frequency Dependence 24
4.1.3 Extension to Higher Frequencies 24
4.2 Theoretical Consideration for Onset of Convection and Threshold Behavior in EHD 26

> [...The effects of electric fields on nematic liquid crystals are spectacular...]
>
> E. Dubois-Violette, P. G. de Gennes and O. Parodi, *J. Phys.* **32**, 305 (1970)

The alignment in a NLC sample can be destroyed by a rather low voltage ($5 \div 7$ V) applied between two points in the sample. Because convection is involved the problem essentially belongs to nematodynamics, in the next sections are only summarized the main results together with their interpretation.

By increasing the electric field amplitude (keep fixed the frequency), convective rolls are longitudinally stretched and broken, with the formation of small scale structures. This dynamical regime is called weak turbulence (WT), and is characterized by patterns on all spatial scales. For higher values of the electric field, the sample reaches a strongly chaotic regime, the so called first dynamical scattering modes (DSM's) where spatial structures are apparently disrupted and the field can be described by multifractal geometry.

4.1 WILLIAMS DOMAIN AND THE HELFRICH INTERPRETATION

The deformation effects in NLC discussed section 2.2.1 arose from the competition of two forces: the dielectric torque $\Delta\epsilon E^2$ (owing to the negative dielectric anisotropy) and a force exerted on the bulk fluid due to the charge separation produced by the positive conductivity anisotropy ($\Delta\sigma > 0$). In particular, the anisotropic electric conductivity is precisely the reason for anomalous orientation of NLC by an external field that does not correspond to the sign of the dielectric anisotropy. As a rule, the reorientation occur when $\Delta\epsilon < 0$ and $\Delta\sigma > 0$, although cases are known of anomalous orientation when $\Delta\epsilon > 0$ and $\Delta\sigma < 0$ [2]. The reason for the anomalous orientation lies in the interaction of the space charge with the external electric field [19].

The deformation actually appear only in a NLC having $\Delta\epsilon < 0$ [6, 20] that has a sufficient electric conductivity. [21] An exception to this is reported in [2] where they observed, at low-voltages, a deformation in *butoxy-benzoic* acid, which has a small positive anisotropy in the nematic phase. This might involve the fact that the criterion $\Delta\epsilon < 0$ is approximate in nature [22], while the exact criterion must be found from the exact expression for the threshold voltage in line with the theory [23, 24]. The study reported in [24] was concerned with theoretical study of EHD instabilities of NLC having $\Delta\epsilon > 0$ with direct current.

The Helfrich model

Following the Helfrich interpretation [25], when a slightly deformed S-oriented ($\mathbf{n}(\mathbf{r}) \perp z$) NLC sample, owing a negative dielectric anisotropy ($\Delta\epsilon < 0$), is under the action of an external electric field $\mathbf{E}(0, 0, E_z)$ (where $E_z = V_0/d$ and V_0 is the applied voltage), the electric field gives rise to a current $\mathbf{I}(I_x, 0, 0)$ due to the elevated conductivity of the NLC in the x direction. The current I_x leads to partial separation of positive and negative ions along the x direction and to formation of a space-charge field $\hat{E}_x$. In this condition a torque M_σ arises from its interaction with the field E_z, and it tends to increase the initial deformation 6.

Williams domains

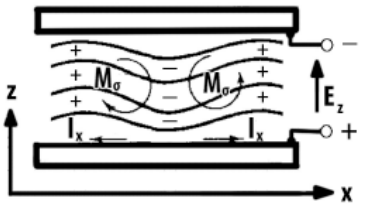

Figure 6: The model of Helfrich. The solid wavy lines indicate the direction of $\mathbf{n}(\mathbf{r})$ in the slightly deformed NLC.

As a result of the torque M_σ, by analyzing the sample under a optical microscope (in polarized light), a spatially-periodic patterns of steady-state flow is observed. This pattern is known as Williams domains (WD) [26]. The WD are manifested as a alternate pattern of dark and bright fringes when a light beam polarized along the x direction[a] pass through the sample cell, and the fringes are perpendicular to the x direction[b].

a The direction of the incident polarization is $\parallel$ to $\mathbf{n}(\mathbf{r})$.
b The Williams domains direction is $\perp$ to $\mathbf{n}(\mathbf{r})$.

The threshold voltage for appearance of the WD ($V_0 = 5 \div 7$V) does not depend on the thickness d of the sample, while the grating period is approximately equal to d. It has been experimentally possible to establish the convective nature of the movement of the liquid, as shown in Fig. 8b, by observing solid particles mixed into the NLC, and even to measure the velocity of this movement (tens of μ/sec) as a function of the voltage [27] (recently has been discovered that the velocity field of the flux inside the sample is the superposition of two phenomena see Chap. 9). The convective movement partially orients the NLC, especially strongly in the region of maximum velocity gradient, i.e., at the centers of the convective rolls.

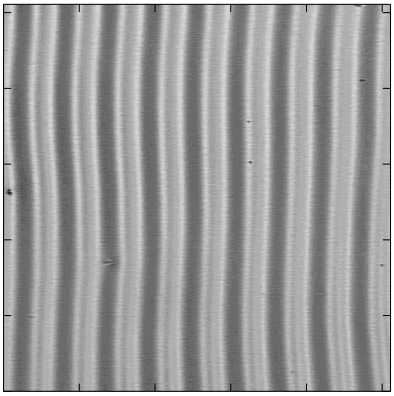

Figure 7: A snapshot of Williams Domains for a sample cell of thickness d = 50μm.

This leads to the periodic variation of the orientation of the director shown in Fig. 8b by the solid line, which in turn causes a periodic variation of the refractive index for light polarized along the x axis. The grating of cylindrical lenses thus formed [28] focuses the transmitted beam into bright lines, which are the Williams domains.

4.1.1 Analytical Determination of the Threshold Voltage for the Williams Domains

In order to determine the onset voltage for Williams Domains in a NLC B-oriented, we must solve a system of four linearized equations [23], which describe an incompressible nematic fluid. The first of them, the equation of motion for the director $\mathbf{n}(\mathbf{r})$, is analogous to Eq. 2.8, but it contain an additional term $\alpha_2 \partial v_z/\partial x$. This term describes the viscous friction torque ($\alpha_2 < 0$ is the friction coefficient, and v_z is the z component of the velocity of the liquid). In the simplest model in which one treats a steady-state regime ($d\theta/dt = 0$) while the threshold for the S-effect is high enough (or, equivalently $\Delta\epsilon_{\parallel} \sim \Delta\epsilon_{\perp}$, $\Delta\epsilon \sim 0$), Eq. 2.8 became:

$$K_{33}\frac{\partial^2\theta}{\partial z^2} - \alpha_2\frac{\partial v_z}{\partial x} = 0. \tag{4.1}$$

The second equation describes the movement of the viscous liquid (η is the viscosity) taking account of the force of the electric field E acting on the space charge δq (Navier-Stokes equation). In the simplest case in which the period of the deformations is of the order of the thickness of the layer of NLC λ_0 ($\lambda_0 \sim d$). The equation will be:

$$2\eta\frac{2\pi}{d}\frac{\partial v_z}{\partial x} - E\delta q = 0. \tag{4.2}$$

The third equation is obtained from the condition of continuity of the current $\nabla \cdot I_x = 0$, where $I_x = \sigma_{\parallel}E_x + \Delta\sigma \cdot E\theta$ [29]:

$$\sigma_{\parallel}\frac{\partial E_x}{\partial x} + \Delta\sigma\frac{\partial\theta}{\partial x} = 0. \tag{4.3}$$

Finally by using the Poisson equation we obtain:

$$\frac{\partial E_x}{x} - \frac{4\pi}{\epsilon}\delta q = 0. \tag{4.4}$$

From Eq. 4.2 we can note that the velocity gradient $\partial v_z/\partial x$ will attain a value at some field value E_0 a such that the torque of the frictional forces in Eq. 4.1 will exceed the elastic torque. Thus, simultaneous solution of the system 4.1 - 4.4 will determine the threshold voltage for the WD formation. Actually:

$$2\eta \cdot \frac{2\pi}{d}\frac{K_{33}}{\alpha_2}\frac{\partial^2\theta}{\partial x^2} = E\frac{\epsilon}{4\pi}\frac{\partial E_x}{x} = -E^2\frac{\epsilon}{4\pi}\frac{\Delta\sigma}{\sigma_{\parallel}}\frac{\partial\theta}{\partial x}. \tag{4.5}$$

Assuming $\partial^2\theta/\partial x^2 \sim (2\pi/d)\partial\theta/\partial x$ (periodic deformation [30] $\lambda_0 \sim d$), we obtain the expression for the threshold voltage for the WD:

$$V_c^2 = \frac{32\pi^3 K_{33}\eta\sigma_{\parallel}}{(-\alpha_2)\epsilon\Delta\sigma}. \tag{4.6}$$

The qualitatively-derived Eq. 4.6 does not differ in principle from the more exact expression given in [23]. Numerical calculation give a value of the order of 10 V, which agrees satisfactorily with experimental results. The solution of the problem obtained by Helfrich [25] that takes account of the dielectric anisotropy of the NLC, $\Delta\epsilon < 0$ gives a somewhat more complex relation for the threshold voltage (case $\mathbf{n}(\mathbf{r}) \parallel x$; see Fig. 6):

$$V_c^2 = \frac{4\pi^3 K_{33}}{\Delta\epsilon(\sigma_{\perp}/\sigma_{\parallel}) + (k_1/\eta 1)\epsilon_{\parallel}[(\epsilon_{\perp}/\epsilon_{\parallel}) - (\sigma_{\perp}/\sigma_{\parallel})}} \tag{4.7}$$

where K_{33}, k_1, and η_1 are the coefficients of: elasticity, friction and viscosity, respectively*. Formally, Eq. 4.7is reduced to Eq. 4.6 when $\Delta\epsilon = 0$[1].

1 Apart from the numerical coefficient.

⋆ An analogous expression is given in [25] for an initial S-oriented case, but with different coefficients of elasticity, friction, and viscosity (K_{11}, k_2, and η_2 respectively).

The theory presented in [25] has a substantial defect. It does not take account of the boundary conditions, while, as we have stated, the wave vector of the spatial deformations in the x direction (q_x) was assumed to be equal to π/d. The steady-state problem with account taken of the boundary conditions has been solved independently in [23, 24]. Here the solution the linearized problem require numerical calculation. The rigorous expressions for V_o that were derived in [24], and which depend parametrically on the ratio of wave vectors $s = q_z/q_x$ are formally reduced for s = o to Eq. 4.7. In fact, the meaning of the viscosity coefficients in Eq. 4.7 proves to differ with different authors [19, 24] and it is apparently given most correctly in [24]: $k_1 = \alpha_2$, $k_2 = \alpha_3$, $\eta_2 = (-alpha_2 + \alpha_4 + \alpha_5)/2$, $\eta_1 = (\alpha_3 + \alpha_4 + \alpha_6)/2$, where the α_i are the Leslie coefficients [31].

4.1.2 Frequency Dependence

The dielectric regime

The behavior of a NLC in an alternating field has been treated theoretically in[29] (without taking account of the boundary conditions). The relation of the instability threshold to the frequency of the external field for and to the geometry of Fig. 6 is given by the following expression

$$\langle V_0^2(\omega)\rangle = \frac{V_0^2(1+\omega^2\tau_0^2}{\zeta^2-(1+\omega^2\tau_0^2)} \tag{4.8}$$

The equation 4.8 is the mean-square value of the threshold voltage at frequency ω.

We can define critical frequency $\omega_c = (\zeta^2-1)^{1/2}/\tau_0$, where τ_0 is the dielectric relaxation time and the quantity (ζ^2-1) contains the material properties.

Equation 4.8 implies that the onset voltage for the WD sharply increases as $\omega \to \omega_c$. Although the ionic current along the z axis follows the external field without lag, the process of space-charge separation along the x coordinate lags in phase behind the field with increasing frequency. This diminishes the force exerted on the space charge q by the external field E, and the torque M_σ is decreased, and one must increase the external voltage to attain instability. The frequency range for $\omega < \omega_c$ is called *conduction regime*. The variation of the threshold voltage V_c is shown in Fig. 8.

4.1.3 Extension to Higher Frequencies

The conductive regime

By observing Fig. 8 is clear the distinction of two very different regimes, respectively below and above a certain threshold frequency ω_c. The frequency range for $\omega > \omega_c$ is known as *dielectric regime*. In this regime threshold field intensity does not depend on the thickness d. In this regime, $V_c(\omega) \sim d^2\omega$, and the wave vector of the deformation pattern depends on the frequency, $q_x \sim \sqrt{\omega}$. According to [29], the calculation of the instability threshold in the dielectric regime is complicated, and it requires numerical technique. A simple expression has been proposed in [32] for the threshold field in the frequency region $\omega > \omega_c$:

$$\langle E_c^2\rangle = \frac{8\alpha_2\omega}{\Delta\epsilon}. \tag{4.9}$$

For $\omega < \omega_c$ the threshold V_c is rather low, and independent of the sample thickness d, and when $V \sim V_c$ we have the formation of WD, with a spatial periodicity comparable to the thickness d. On the contrary, in the case $\omega > \omega_c$ the threshold is higher and V_c is

proportion to d [36], and the threshold parameter is the field $E_c = V_c/d$, where E_c varies as $\omega^{\frac{1}{2}}$. The onset instability at V_c is manifested by some parallel striation, which a distance much smaller than d, and a dependence from the frequency as $1/E_c \sim \omega^{-\frac{1}{2}}$.

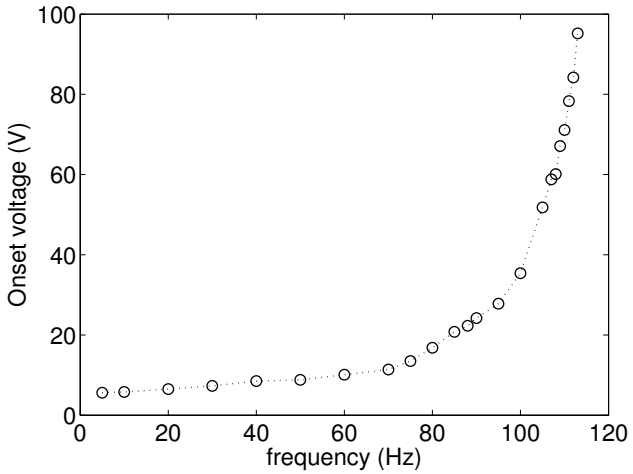

Figure 8: The typical V_c Vs. ω behavior for an MBBA sample, relative for $\omega < \omega_c$, until $\omega \sim \omega_c$.

This second type of instability has been observed first in [33] and studied in detail by the Orsay Group [34], who coined the name "*chevrons*" 9. The cut-off frequency $\omega_c/2\pi$ is typically of the order of 100 Hz and is found to increase linearly with se sample conductivity⋆ [34].

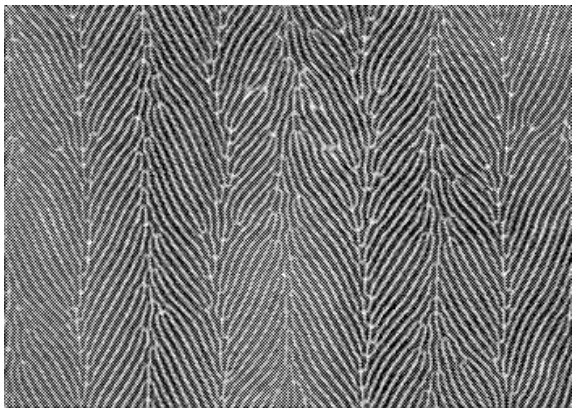

Figure 9: A snapshot of "chevrons" for $\omega > \omega_c$

⋆ In a very pure sample with a very low conductance the a.c. field effects should always correspond to the chevron regime.

4.2 THEORETICAL CONSIDERATION FOR ONSET OF CONVECTION AND THRESHOLD BEHAVIOR IN EHD

The basic mechanism for the onset of convection has been understood and described for an applied dc-voltage by Helfrich [35].

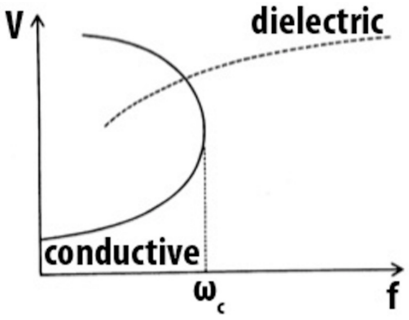

Figure 10: Stability diagram for EHD convection. The solid and dot lines show the thresholds above convection take place.

By the Orsay Group [29] this was extended to an ac-voltage and it was recognized within the one dimensional approximation that there are two different frequency regimes, , the low frequency conduction and the high frequency dielectric regime at the onset of convection (Fig. 10). In the conduction regime convection rolls have a wavelength of the order of the thickness of the fluid layer and their director is mainly stationary in time with small modulation, whereas in the dielectric regime the director is mainly oscillating with the external frequency and the stationary part is smaller. The wavelength of the periodic pattern in the dielectric regime is much smaller than the layer thickness and is for large ranges

The one dimensional model

independent of the thickness and the conductivity. This could be alredy roughly understood in the framework of the *one-dimension model* (ODM) calculation [26, 36].

Originally, it was assumed that the periodic pattern occurs at threshold always with the roll axis normal to the undistorted director orientation (normal rolls), which was often experimentally confirmed. However Hilsum and Saunders [37] observed a secondary transition to an oblique roll convection structure. This second transition can be understood by taking in account the *flexoelectric effects* in the ODM. In the conduction regime the onset via traveling waves has been also observed [38, 39]. But unfortunately theoretically the occurrence of a Hopf bifurcation could not be predicted, even by a rigorous solution of the full linearized hydrodynamic equations without further assumptions.

The equations of EHD

The basic equations for EHD convection are provided by the standard hydrodynamic description of NLCs [40], and for the same equations including the flexoelectric effects. They consist of the momentum balance (Navier-Stokes equation) together with incompressibility $\nabla \cdot \mathbf{v} = 0$, which determine the velocity field $\mathbf{v}$, and the balance of torque which gives the director $\mathbf{n}$. Moreover, there are electric field equations in the quasi-static approximation. The complete electric field is the superposition of induced and applied part: $\mathbf{E} = -\nabla\phi + (V(t)/d)\hat{\mathbf{z}}$ and $\mathbf{n}$ is defined in polar coordinates: $\mathbf{n} = (\cos\Theta\cos\Psi, \cos\Theta\sin\Psi, \sin\Theta)$. All these equations are coupled and provide an highly nonlinear set of equations for three velocity components, two angles for $\mathbf{n}$ and the induced electric potential ϕ.

The threshold for EHD is calculated by assuming that all quantities deviate only very slightly from their values in the basic unstructured state, which is characterized by $\mathbf{v} = 0$, $\mathbf{n} = (1, 0, 0)$ and $\phi = 0$ (which is equivalent to vanishing charge density). We then write $\mathbf{n} = (1, \Psi, \Theta)$ and linearize the equations in the small deviations [41, 42].

Translational invariance

The resulting set of linear partial differential equations (PDE) for $\mathbf{u} = \{\phi, \Theta, \Psi, \mathbf{v}\}$ is translational invariant with respect to x and y and therefore the solutions are harmonic and may be chosen proportional to $\sin(qx + py)$ and $\cos(qx + py)$ ($(p, q) = 2\pi/\lambda_{x,y}$, where $\lambda_{x,y}$ are the wavelength of the convective structure in the x and y directions). The applied voltage is

assumed periodic in time (with periodicity T), $V(t) = \langle V \rangle f(t)$, with $f(t) = f(t+T)$. The set of linear equations has then the formal structure:

$$\tilde{M}(t, \partial_z)\partial_t \mathbf{u}(z,t) = \tilde{L}(t, \partial_z)\mathbf{u}(z,t) \tag{4.10}$$

where the 6×6 matrices $\tilde{M}$ and $\tilde{L}$ contain derivatives with respect to z and depend on q, p and $V(t)$ and they have the periodicity T in time. Rigid planar anchoring of the director and ideal conducting electrodes are assumed. Therefore we have the boundary conditions*

$$\mathbf{u} = 0, \quad and \quad z = \pm d/2 \tag{4.11}$$

* from $\nabla \cdot \mathbf{v} = 0$ we also obtain $\partial_z v_z = 0$ at $z = \pm d/2$.

From periodic driving voltage $V(t)$ the linear modes are expected to be of the form

$$\mathbf{u}(z,t) = \mathbf{u}'(z,t) exp(\sigma t), \ \sigma = \sigma_r + i\sigma_i, \tag{4.12}$$

where, according to the Floquet theorem [43] $\mathbf{u}'$ is periodic in t with period T. For the numerical solution of Eq. 4.10, for each component $\mathbf{u}'_k$ an expansion into a complete set of z-dependent function has been chosen [41, 42]:

$$\mathbf{u}'_k(z,t) = \sum_{j=1}^{N} \mathbf{w}_{k,j}(t)\Lambda_{k,j}(z). \tag{4.13}$$

Eq. 4.10 is then transformed into a set of ordinary differential equations (ODE) for $\mathbf{W} = (\mathbf{w}_1, \cdots, \mathbf{w}_n)(\mathbf{w}_k = (w_{k1}, \cdots, w_{kN}))$. By integrating the set of ODE in time from t to $t+T$ and by using the boundary condition $\mathbf{W}(t) = \mathbf{W}(t+T)$ the Floquet exponents σ can be determined. The neutral surface $V_0(p, q, \omega)$ with respect to q and p provides the absolute threshold $V_c(\omega)$ and the critical wavevector (q_c, p_c). For a Hopf-bifurcation the critical frequency is defined by the Hopf frequency $\nu_c = \Im[\sigma_{max}(V_c(\omega), q_c, p_c)]$. The condition $\partial^2 V_0(\omega)/\partial p^2 > 0$ at $(q_c, p_c = 0)$ is necessary for normal rolls to occur at threshold. Otherwise there exists a lower threshold at $p_c > 0$ (oblique rolls). If there is continuous transition from normal to oblique rolls $p_c \to 0$ at threshold by changing the frequency. The transition frequency $\omega \cdot \tau_0$ is then marked by $\partial^2 V_0(\omega)/\partial p^2 = 0$ at $(q_c, p_c = 0)$. This frequency is known as *Lifshitz point*.

Symmetry consideration

Now we consider the symmetry behaviour of the solution of Eq. 4.10 in more detail for a vanishing flexoelectric effect and a driving voltage with property $V(t + T/2) = -V(T)$. In this case the symmetry of $\mathbf{u}'$ with respect to z is

$$(\Phi, \Theta, \Psi, v_x, v_y, v_z)(-z) = \pm(\Phi, \Theta, -\Psi, -v_x, -v_y, -v_z)(z) \tag{4.14}$$

(+ sign = "type I", − sign = "type II") and the symmetry with respect to the translation $t \to t + T/2$ is:

$$(\Phi, \Theta, \Psi, \mathbf{v})(t + T/2) = \pm(-\Phi, \Theta, \Psi, \mathbf{v})(t) \tag{4.15}$$

(+ sign = "type A", − sign = "type B").

The EHD modes

The type A is the well known conduction mode and the type B is the dielectric mode. The symmetry Eq. 4.15 express also the fact that without the flexoelectric effect the polarity of the electric field E does not affect the director orientation $\mathbf{n}$ and the velocity $\mathbf{v}$. In each symmetry class we obtain a lowest threshold $V_c(\omega)$.

The thresholds $V_c(\omega)$ for these four solutions are shown in Fig. 11 (left panel). These results has been calculated for the MBBA whit $\sigma_\perp d^2 = 80 \cdot 10^{-8} \Omega^{-1} m^{-1}$ and an harmonic

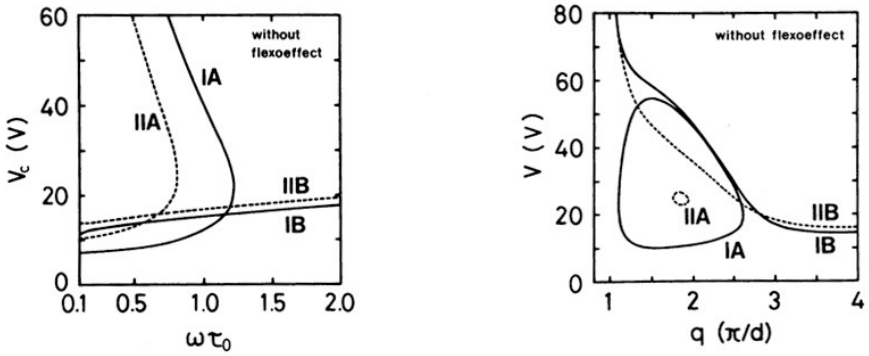

Figure 11: Thresholds of four branches for solution described in the text: left panel minima of neutral curve as a function of frequency, right panel neutral curves at frequency slightly below ω_c, taken from *Pattern Dynamics in the Electrohydrodynamics of Nematic Liquid Crystals*.

driving voltage. The type IA solutions describes the lowest threshold in the conduction regime whereas the type IB provide the lowest threshold in the dielectric regime. At this lowest thresholds we have always normal rolls ($p_c = 0$). Type IIA and IIB solutions describe modes with higher thresholds. For the IA mode the threshold curve turns over the upper re-stabilizations branch at the so called cut-off frequency ω_c. The IIA mode shows the analogous behavior. The two dielectric modes IB and IIB have different z-symmetry but the threshold difference between both is relatively small, which is quite remarkable.

Threshold differences

The threshold difference between the first two z-dependent modes(one symmetric and the other anti-symmetric with respect to the thickness d of a layer), and also the threshold difference between the modes IA and IIA, is of the order of the first threshold value. Therefore an interaction of these two simple modes could only be expected far away from the threshold but then already also higher harmonics in the z-direction are excited and the non-linear solution become complicated. However the small difference in the threshold between the IB and IIB modes can be considered as an unfolding *codimensional two bifurcation* (CDT) where a simple interaction of both modes is possible. The associated critical wavenumber of the conduction modes are nearly insensitive to the change of $\sigma_\perp \cdot d$.

In Fig. 11 (rigth panel) is plotted the neutral curves for the frequency $\omega \cdot \tau_0 = 0.8$ (τ_0 is the charge relaxation time) [41, 42]. The neutral curves of the branches IA and IIA are closed loops in the frequency range with restabilization. The neutral curves for the branches IA and IB, and also for IIA and IIB, are in general not allowed to intersect each other. This explains the deformation of the neutral curve in IB. By intersecting σd the threshold of the dielectric mode increases strongly and then this deformation can be removed.

The intersection point of the lowest threshold curves $V_c(\omega)$ in Fig. 11 (left panel) corresponds to the situation where in Fig. 11 the minima of two lowest curves (IA and IB) lie at the sam voltage. This is the situation of a CDT bifurcation of two bifurcations with different wave-numbers. At this CDT point the wavenumber ratio $q_c^d/q_c/d$ of the dielectric and the conduction mode can vary over a large range ($\sim 1-20$) depending on the parameters, especially the dielectric anisotropy, the conductivity and the thickness. By an appropriate choice of σd and an additional of an external magnetic field in the x-direction the ratio $q_c^d/q_c/d$ can be also brought to the resonance value 2 to 3. Near such CDT point various interesting secondary bifurcations are expected [44]. The detailed character of the CDT point, however, also depends on whether the threshold $V_c(\omega)$ of the dielectric mode mode intersect the conduction threshold at the lower branch or the stabilization branch or at the turn over point.

The differences between these last three possibilities become stronger for a nematic material whit large negative dielectric anisotropy [45].

Solution whit the flexoelectric effect

Taking the flexoelectric effect into account the separate symmetries 4.14 and 4.15 are destroyed, but the combined simmetryes $z \to -z$ and $V \to -V$ remain. That means for driving voltages with the symmetry $V(t + T/2) = -V(t)$ one still has tho separate modes: the superposition of type IA and IIB solutions provides the threshold for the conduction regime and the superposition of the type IB and IIA solutions gives the threshold for the dielectric regime. Using a driving voltage without the above symmetry a superposition of all four types is necessary to solve the linear problem and therefore no further a priori distinction between the conduction and the dielectric mode is possible.

The calculations of the threshold behavior obtained from the full set of hydrodynamic equations can be also extended to stochastic excitations. Due to the stochastic excitation the described independent linear threshold modes are coupled. It is an open question whether this leads for example to an Hopf bifurcation or to a multiple bifurcation point, where the real parts of several eigenvalues pass simultaneously through zero. In an experiment it has been found that by a stochastic excitation it is possible to induce a direct transition from a non-convective regime to turbulence.

5 EXPERIMENTAL OBSERVATION OF EHD TURBULENCE

CONTENTS

5.1 The Fragmentation Model 31
5.2 Evolution of EHD Instabilities 32
5.2.1 Undulation, Zig-Zag, and Oblique Rolls 32
5.2.2 The bimodal Structure (Rectangular cells) 33
5.2.3 Remarks on the Nature of The Transition to the Bimodal 35
5.3 Transition to a Weak Turbulence Regime 35
5.4 The Dynamic Scattering Mode 2 36
5.5 Chaoticity? The Lyapunov exponents 39
5.5.1 Lyapunov Exponent for the DSM2 40

As sentenced in Chap. 2 and 4 a nematic liquid crystal is a fluid with an orienentational ordering (denoted by a director $\mathbf{n}(\mathbf{r})$) and is characterized by by a coupling between that ordering and the velocity gradients which are present [36]. The molecular orientation is controlled by elastic and viscous torques, and is sensitive to external fields. The first convection occurs as rolls having an orientation perpendicular to the molecular axis direction $\mathbf{n}(\mathbf{r})$, say Williams Domains. When the external field is slowly increased new instabilities appear The main step in the evolution to turbulence occurs under the form of a pinching instability of the convective rolls. Turbulence in our fluid corresponds to a disordering of the orientation, and we shall show in Chap. 6 that it is associated with topological singularities in the orientation field, expressed as a surrogate measure called distortion energy density.

Up to the present time, many attempts have been reported that such an anisotropic fluid has been used under an electric field in order to look for and study the possible structures before chaos [39]. However the observed sequences were either incomplete or included irrelevant structures. No clear classification could be made, and the study of the evolution of the streamlines was omitted. The only reliable observation was that, as in Rayleigh-Bénard convection, two structures (rolls and rectangles) were often created between the rest state and the chaos. In fact, experimental data or accurate observation concerning the convection amplitude (velocity or molecular orientation) were difficult to obtain because of the presence of a large density of defects.

5.1 THE FRAGMENTATION MODEL

Multi convective structures: fragmentation model

In the turbulent state the flow field, of NLC, may be, at some time, considered as a superposition of elementary rotations randomly distributed in space and fluctuating in time. As the external field is increased, the time and space scales decrease. Let us consider only the time independent states, *i.e.* we restrict our picture of turbulent motion to a spatially disordered superposition of elementary rotations[1]. In a typical convection experiment the first structure is a set of parallel rolls with a preferred alignment *i.e.* y direction (Fig. 12A). The next step

1 We consider the transition to turbulence related to the fragmentation of the original WD rolls

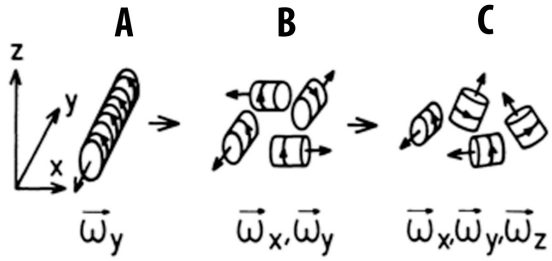

Figure 12: A simple fragmentation model for the evolution from one convective mode to turbulence: A) convection rolls around y, B) second mode added around x, C) turbulent state. ω_α is the angular frequency of the mode around the α direction.

will add, to the first *mode*, a second *mode* of rotation *i.e.* around the x direction (Fig. 12B). Next, a third *mode* around z will be added (Fig. 12C. These modes can be sketched as slice of the former rolls, which afterwards have uniformly been reoriented. The resulting structures will be ordered in space. Disordering may be caused by localized perturbations that produce defects in the structures. The turbulent state is obtained when these perturbations are, in addition, fluctuating in time. Such a structure would then appear as a randomly moving ensemble of still-ordered domains. As the external field increases, the local velocity increases, and the size of the ordered domain decreases.

5.2 EVOLUTION OF EHD INSTABILITIES

5.2.1 Undulation, Zig-Zag, and Oblique Rolls

Undulation of WD

As sentenced in sec. 5.1 when the electric is increased, the WD structures begin to fragment themselves in small parts, and other modes of convection appears. As first step before the fragmentation the WD structures becomes undulatory[2] along the roll axis y for a well defined voltage $V_u \sim 15$V. The deformation is static and has a sinusoidal shape with a spatial period $\Lambda = 2\pi/q_y$ of order 5 to 7 times the roll diameter d 13. In order to describe the undulatory roll we shall measure the local tilt angle along y, $\theta = \theta_m \sin(q_y, y)$. The maximum tilt angle θ_m over y, measured at the inflection point increase with the voltage[3] V_0, while Λ remains constant. In 1986 R. Ribotta and A. Joets found that the angle θ_m scales as $\theta_m \sim \epsilon^{0.43}$ $\epsilon = (V_0^2 - V_u^2)/V_u^2$ is defined as the control parameter (or reduced voltages), in our case we found that $\theta_m \sim \epsilon^{0.46}$. This behavior is characteristics of a direct bifurcation.

Zig-zag deformation

At higher voltage, θ_m remains constant while Λ increases sharply. The deformation is no longer sinusoidal but becomes angular while the rolls straighten. The increase of Λ is limited by the defects which nucleate more easily and pile up along y in order to form a grain boundaries. The final stage of evolution of the system is an ensemble of domains of parallel rolls, tilted symmetrically with respect to y. Then, after long time ($\sim 20 \div$min) a final shape is reached which consists in a pattern of rectilinear rolls tilted symmetrically by θ over y. The process of change in the shape is a continuous one and does not mean that a structure instability has occurred. In fact, the defects present in the sample tend to pile-up and form grain boundaries ath the limit of domains tilted by $+\theta$ $-\theta$. These domains can increase their

2 Before the undulatory distortion appears, the WD tends to crate some defect called *edge dislocation*, and around the core, the rolls are depressed on one side and compressed on the other side of a line normal to the roll axis and passing through the core. This type of instability is non described here.

3 The external electric field is defined as: $\mathbf{E} = (0, 0, V_0/d^\star)$ where V_0 is the applied voltage and $d^\star$ is the sample thickness.

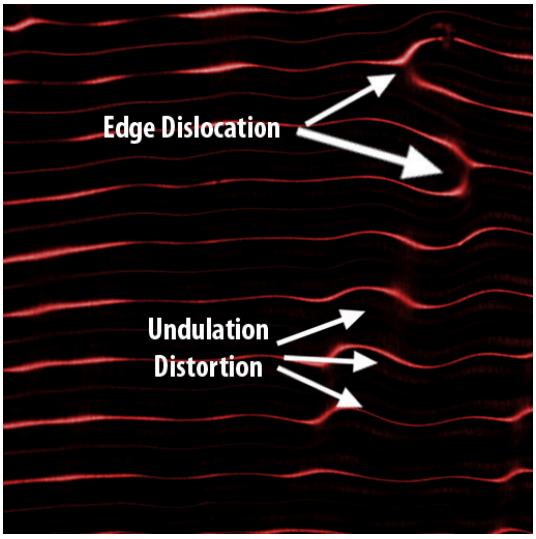

Figure 13: A snapshot of the undulatory rolls and the edge dislocation obtained for $V_0 \sim 17V$.

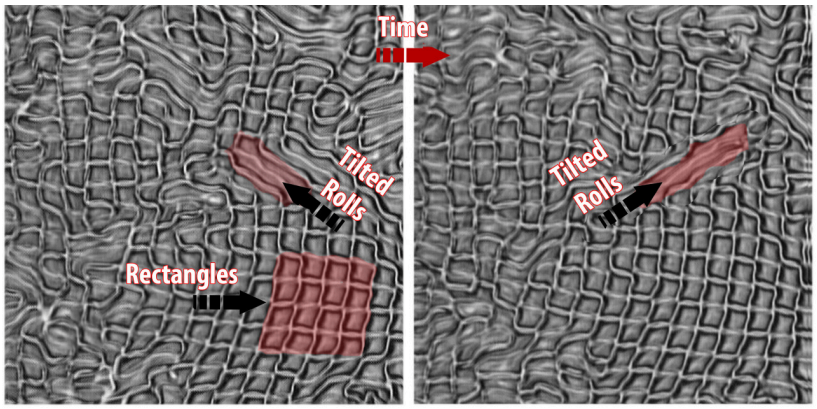

Figure 14: Tilted rolls, and rectangular cell.

area at a costant voltage as the time evolve. The final structure is a set of large domains made of rectilinear rolls tilted by $+\theta$ or $-\theta$ over the y axis (zig-zag structure).

5.2.2 The bimodal Structure (Rectangular cells)

A structure made of rectangular cells has often been observed, this type of structure is not so difficult to obtain. A very easy method to observe the formation of the rectangular cells is by rapid growing a large number of defects. In fact, this structure is obtained by a slightly increment of the external field, usually around $\sim 11V$.

Apparently the rolls are again along y, by looking at the streamlines, we can see that in the middle of the side of the cell along y there are now, nodal points where the flow is focused (the rotation mode is ω_y). In addition, the small individual rotations ω_x obtained in the point which connect[4] two angular zone are coupled, and a new mode is obtained along x.

4 The word "connect" does not mean a physical connection between two different cell but just the zone in which the distance between two angle of two cells minimum

Each of these cells has a rotation ω_y opposite to its near neighbor (also along x the rotation is alternate).

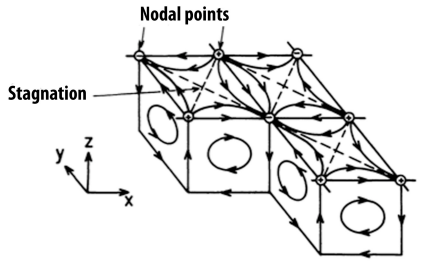

Figure 15: A sketch of the bimodal structure. The convection occurs between singular nodal points. Stagnation points indicate a zero vertical velocity.

The the elementary cell (Fig. 15) is a rectangular cell centered on a nodal point, and at each corner is a stagnation point which separate each individual cell. The rectangles corresponds to the sudden connection of the ω_x modes which are formed by the distortion of the previous state (the distortion of the zig-zag pattern), then a new rotation element ω_x is created and is decoupled from the former one ω_y. This structure is known as *bimodal*, the transition between the distortion of the zig-zag pattern and the formation of the rectangles belong to first order group as sentenced in [63].

Zig-zag oscillations: the bimodal structure

Before reaching the stable rectangular structure, the sample shows some oscillation between a zig-zag (or some times tilted rolls fig. 14) domains around the y direction between $-\theta$ and $+\theta$. These oscillation are periodic in time and, and the period decrease as V_0 increase. For $\theta = \theta_{max}$, the rolls are zig-zag, when θ decrease, the rolls tends to reform the rectangular structure. For $\theta = 0$ the rectangles set in, then the oscillations goes on the opposite direction and the rectangles becomes unstable[5] 16. As sentenced before, when V_0 increase the period of oscillation decrease, as the same way the size of the oscillating domain decrease. Finally,

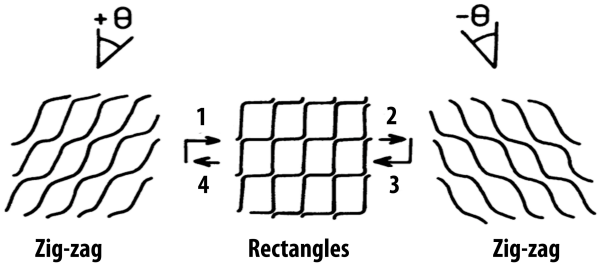

Figure 16: Oscillation around the bimodal structure. The periodic oscillations occurs between two directions of the zig-zag.

after a time of $\sim$ 10min, the whole structure stabilizes on the bimodal rectangles. Usually the last oscillating domain is clamped around a defect* and that duration is necessary for eliminating the defect. This transient state is actually not undestood, but in presence of large number of defects it produces a randomly fluctuating structure which can appear well below the rectangular structure.

$\star$ The defect in the rectangular structure consist of an extra half row connected with an extra half column 17. The topology of this defect shows a number of singularities (nodal and stagnation points) whit a zero sum. Defect consisting of an extra period, either two row or two columns, has not been encountered. This behaviour is probably, in this case, due to the necessity of a larger core area.

5 Try to imagine this deformation as a pendulum

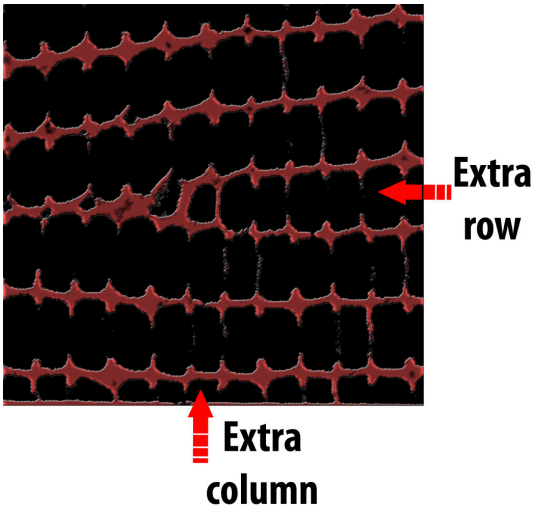

Figure 17: Defect in the rectangula structure.

5.2.3 Remarks on the Nature of The Transition to the Bimodal

When two distinct structures co-exist a sharp boundary separate them. The optical pattern changes abruptly at the transition. At last, the oscillations are quite indicative of some relaxation oscillations which can occur around an inverse bifurcation. These qualitative facts are in favor of a transition zig-zag $\rightarrow$ rectangular $\rightarrow$ zig-zag structure of a quasi-first order (or inverse bifurcation).

5.3 TRANSITION TO A WEAK TURBULENCE REGIME

At about $V_0 = 20V$, the rectangular structure once again starts oscillating between $-\theta$ and $+\theta$ around y in way similar as previous description. However the rectangle becomes more and more distorted as V_0 increase. The area of the oscillating domains is no more the same for each one, but a single rectangle tends to form smaller ones in a process similar to the Richardson cascade. Around $V_0 = 25V$ a new regime composed by structures at different scales is reached: this regime is actually a real turbulent regime characterized by a cascade of structures on all scales.

The weak turbulent regime

The new domains formed, as sentenced before, are distorted and formed by elongated pieces of cells which shows some appearance of portions of rolls. If we rotate the polarizer by $\pi/2$ we can observe inside these cells, some loops of singular lines similar to the disclination walls but whit a rather distorted shape (Fig. 18). Thus the flow no longer has simple symmetry elements. For a slightly increasing voltage these loops rotate in the cell around their mean direction. this rotation rapidly increase and the average size decrease simultaneously. At this point the appearance of coherent oscillations disappears, each cell having now a motion totally independent from its neighbor. The correlation length of the structure is now reduced to the order of one cell. The singular lines indicate that the orientational order shows a large gradient due to a high shear flow. The structure is no longer ordered in the usual sense (over distances large compared to the characteristic length d), and there is now a rotation component around z (ω_z). In fact this regime is a first step in which the ordering is lost simultaneously in space and in time. However the individual motions are still occurring on a scale comparable to d, the sample thickness.

Distortion of disclination loops

Rotation around z

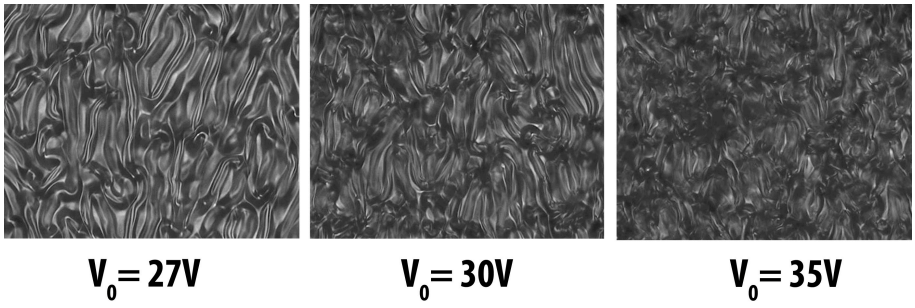

Figure 18: Evolution of the weak turbulent regime as a function of the applied voltage V_0.

5.4 THE DYNAMIC SCATTERING MODE 2

The nucleation process

When the external voltage V_0 is further increased The pattern became more and more chaotic. At this point the *dynamic scattering mode 2* "DSM2" sets up[6]. The DSM2 appears as a nucleation[7] process in which the DSM2 nuclei expands from a point and invades the whole space (Fig. 19), absorbing the DSM1 regime. Usually the DSM2 grow point is focused on a defect in the pattern: impurities or anchoring defect.

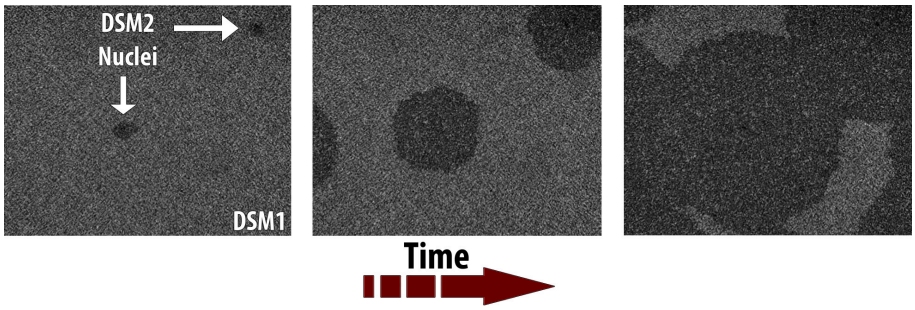

Figure 19: A set of snapshots for the DSM2 nucleation, obtained for $V_0 = 50V$ and $f = 70Hz$, as a function of time $t^\star$. The sequence has been taken by jumping directly from $V_0 = 0 \rightarrow V_0 = V^\star$.

Scattering of visible light: reduction of transmittance

When this new regime sets up a strong reduction in the light transmittance (Fig. 20), and a strong intermittency in the observed pattern are present (7). When the light trasmittance begin to decrease we can fix the threshold value $V^\star$ for the transition DSM1→DSM2. The transmittance reduction, typically shows an exponential decay of the form: $I = I_0 e^{-V/\alpha}$ (α is the decay rate), in our case $\alpha = 5.1 \pm 0.1V$ for the DSM1 case and $\alpha = 14.2 \pm 0.4V$ in the DSM2 case (Fig. 21). This reduction of transmittance is always related to the fragmentation of the rolls. In this regime (DSM2) the average size of the structures seems to be of the order of the visible light, and a strong scattering effect is evident. For this reason it takes that name dynamic[8] scattering mode.

Scattering mean free path ℓ

A parameter used to describe the strong and recurrent scattering events is mean free path ℓ,

6 Actually also a DSM1 regime exist, but is difficult to fix a threshold value in the external voltage V_0 for this regime. The transition from the weak turbulence to the DSM1 regime is a continuous transition whit out any break. We fix the threshold value for the DSM1 just above the value at which the DSM2 appears, see the text for further information.

7 The creation of different DSM2 nuclei follow the classical law of the a nucleation process: $J = J_\infty(-A/(1+\epsilon)) + B$, ϵ is the reduce voltage see 5.2.1

8 The term dynamic is used to describe the continuous motion of the structures under the action of the external field.

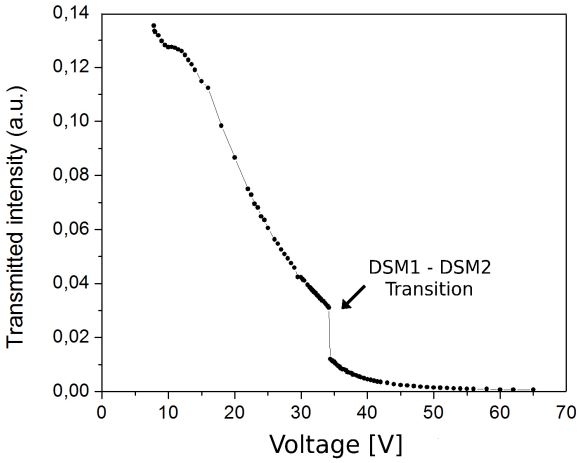

Figure 20: Light transmittance through the sample, as a function of the applied voltage V_0.

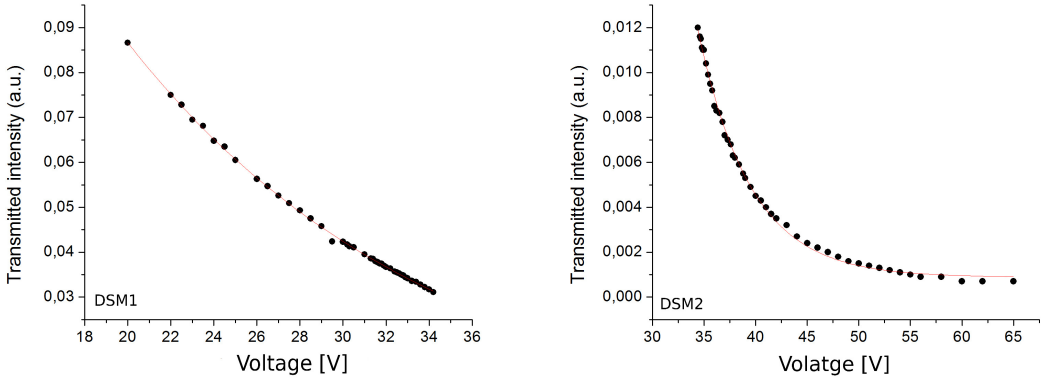

Figure 21: Left panel: transmittance in the DSM1 case, right panel: transmittance in the DSM2 case.

which give a measure of the path traveled by a photon between two scattering events. From the Beer's law we have $I = I_0 e^{d/\ell}$ where d is the sample thickness and ℓ is the scattering mean free path, from a linear transformation we can have information of this parameter as function of the applied voltage V_0 (Fig. 22). From the experimental results we understand that for low voltages photons are scattered just few times, probably from the defect in the structures described in the previous sections, and the mean free path ℓ is of the order of $\sim 40\mu m$. For higher value of V_0 (DSM2 case), the mean free path ℓ is drastically reduced ($\ell \sim 5\mu m$). This reduction is relate to a transition from a single scattering event regime to a multiple scattering event regime, say the photons are scattered many and many times before they pass through the sample. In other word if we imagine[9], in a simple case, the sample composed by a set of N thin layers of NLC, each time that the light penetrate a single layer probes a different refraction index n, and for each layer a certain amount (percentage) of the incident light pass to the $N+1$ layer, while a certain percentage is reflected backward to the

9 This description is also valid in two or three dimensional case, but is more complicated because the transmission and the reflection can be not on the same plane. This cases are not described here.

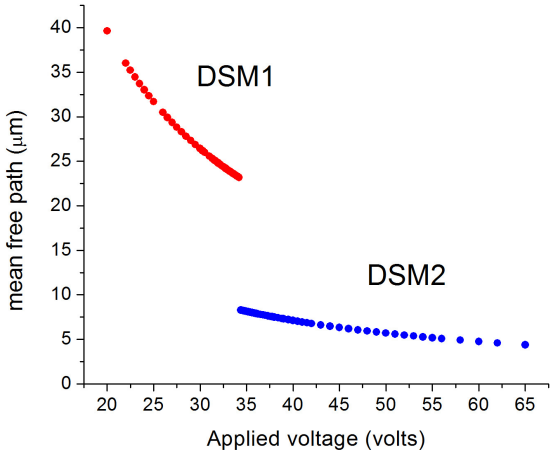

Figure 22: The mean free path ℓ as a function the applied voltage V_0, the sample thickness is $\sim 50\mu m$.

$N-1$ layer. When the external field is increased the thickness of these layers decrease and the number N increase, for this reason a strong reduction . As the time goes on a certain amount (percentage) of the incident light is trapped inside the sample for a certain time. This behavior is a fingerprint of a light weak localization phenomena. More information about the multiple scattering and the weak localization are discussed in Chap. 10.

DSM2: a directed percoletion unversality class

Recently has been shown that the DSM1→DSM2 transition belong to the *directed percolation* (DP) universality class (an example is reported in Fig. 23, a kind of second order phase transition (see B). Takeuchi et al. attempt to experimentally realize a steady-state transition in the DP class. The sample is a NLC (thickness $12\mu m$) of conventional MBBA, close to

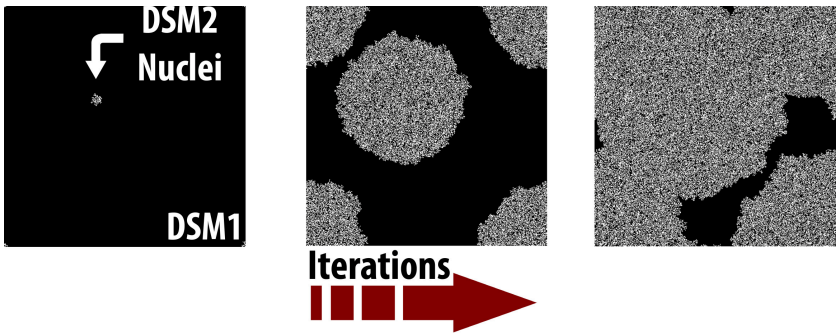

Figure 23: A Monte Carlo cellular automata simulation on a 2D lattice of dimension $L \times L$, for a DP class process. The simulation is based on the rule: $P^{i,j}_{0\to 1} = p_1/4(s_{i-1,j} + s_{i+1,j} + s_{i,j-1} + s_{i,j+1}) + h$ and $P^{i,j}_{1\to 0} = p_2$, where i,j represents the lattice point, h is an extra small probability to create an active site spontaneously anywhere is added, and p_1, p_2 depends by a parameter λ which represent the interaction whit the external field. The simulation was performed by us.

the voltage threshold $V^\star$ for the appearance of DSM2, has been discovered that (due to the spatio-temporal intermittency sentenced before) the DSM2 plays the role of an active state and DSM1 corresponds to the absorbing state. It is also argued that the system under study should be less sensitive to other experiments:

1. since it is macroscopic, sensitivity to quenched disorder is much less than in small systems on a molecular scale and

2. since it is chaotic in both states, it is less sensitive to long-range interactions.

As the order parameter[10] is simply the density of DSM2 points, its observation gives an estimate of the non-universal threshold p_c and the exponent β for which Takeuchi et al. report the estimate $\beta = 0.59(4)$. Furthermore, the distributions of the size Δl and the duration Δt of the inactive regions are measured. Form the expected power laws $e_\perp(\Delta l) \sim (Deltal))^{\epsilon_\perp/\nu_\perp}$ and $e_\parallel(\Delta t) \sim (\Delta t)^{\epsilon_\parallel/\nu_\parallel}$ whit the scaling relations $\epsilon_{\parallel,\perp} = 2 - \beta/\nu_{\parallel,\perp}$, they find $\nu_{\perp,x} = 0.66$, $\nu_{\perp,y} = 0.77$ and $\nu_\parallel = 1.51$, where the index x, y refers to the spatial direction in which the distribution is measured. Their results for β and $\nu_\perp$ compare quite well whit the theoretical expectation for the DP class B: $\beta \approx 0.583$, $\nu_\perp \approx 0733$ and $\nu_\parallel \approx 1.295$.

They hence carried out a different experiment by bringing the system first deep into the regime with a large DSM2 before *quenching* the system to close to the voltage threshold. Measuring the relaxation of the DSM2 they extract a second estimate for $\beta/\nu_parallel$. This leads to $\nu_parallel = 1.181$, in better agreement with the theoretical prediction. Finally, they present their data in the form of a data collapse and find that their scaling function matches quite well with the corresponding scaling function of the contact process B. In this experiment, it has been possible for the first time to obtain estimates for all three independent exponents which are in fair agreement with the theoretical values for the DP class in $2+1$ dimensions, as well as the entire scaling function. If these findings can be substantiated by further tests and improved estimates the chaotic liquid crystal studied by Takeuchi et al. would be the first experimental realization of directed percolation.

5.5 CHAOTICITY? THE LYAPUNOV EXPONENTS

[....The hardest thing to get right about Lyapunov exponents is the spelling of Lyapunov, which we will variously find as Liapunov, Lyapunof and even Liapunoff. Of course Lyapunov is really spelled in the Cyrillic alphabet: (λ)(backwards r)(π)(Y)(H)(o)(B). Now that there is an ANSI standard of transliteration for Cyrillic, we expect all references to converge on the version Lyapunov.....]

A measure of convergence or divergence of particle orbits

After this short introduction we discuss about the meaning of these exponents. Lyapunov exponents measure the rate at which nearby orbits converge or diverge. There are as many Lyapunov exponents as there are dimensions in the state space of the system, but the largest is usually the most important. Roughly speaking the (maximal) Lyapunov exponent is the time constant, lambda, in the expression for the distance between two nearby orbits, $e^{\lambda t}$. If λ is negative, then the orbits converge in time, and the dynamical system is insensitive to initial conditions. However, if λ is positive, then the distance between nearby orbits grows exponentially in time, and the system exhibits sensitive dependence on initial conditions.

There are basically two ways to compute Lyapunov exponents. In one way one chooses two nearby points, evolves them in time, measuring the growth rate of the distance between them. This is useful when one has a time series, but has the disadvantage that the growth rate is really not a local effect as the points separate. A better way is to measure the growth rate of tangent vectors to a given orbit.

More precisely, consider a map f in an m dimensional phase space, and its derivative matrix $Df(x)$. Let $\mathbf{v}$ be a tangent vector at the point x. Then we define a function

$$L(x, \mathbf{v}) = \lim_{n\to\infty} \frac{1}{n} \ln |Df^n(x)\mathbf{v}|.$$

10 ρ is the order parameter in B

Now the Multiplicative Ergodic Theorem of Oseledec states that this limit exists for almost all points x and all tangent vectors $\mathbf{v}$. There are at most m distinct values of L as we let $\mathbf{v}$ range over the tangent space. These are the Lyapunov exponents at x.

In our case we can study the chaoticity of the system by building up a simple model for the ligth which pass through the sample.

5.5.1 Lyapunov Exponent for the DSM2

For our model we consider the sample NLC cell as random optical media made by a sequence of $N > 1$ layers of thickness b and index of refraction n_i, $i = 1, ...N$. For each layer n_i is a random variable extracted according to a given probability distribution[11]. We are interested in the properties of the transmission through the N layers of a monocromatic light beam. The sample can be seen as a random Fabry-Perot interferometer.

For a simple $1-D$ case we assume the random sample as a line between $x = 0$ and $x = N$. For simplicity we take $b = 1$ (in some units), then the incident and transmitted light waves are given by:

$$\begin{aligned} \phi(x) &= e^{ik_0 x} + r_1 e^{-ik_0 x}, \quad x \leqslant 0 \\ \phi(x) &= t_N e^{ik_0 x} \end{aligned} \tag{5.1}$$

where t_N is the complex transmission coefficient of the N layers, r_1 is the complex refraction coefficient of the first layer, and k_0 is the wavenumber outside the sample. We assume no absorption from the layers, so that $|t_i| + |r_i| = 1$.

By solving the wave equation for each layer, and imposing the continuity of $\phi(x)$ and its derivative at $x = 1, ..., N$ it is known that t_N and r_1 are related by

$$\begin{pmatrix} t_n e^{ik_0 N} \\ ik_0 t_n e^{ik_0 N} \end{pmatrix} = \left[\prod_{i=1}^{N+1} \mathbf{Q_i} \right] \begin{pmatrix} 1 + r_1 \\ ik_0(1 - r_1) \end{pmatrix} \tag{5.2}$$

where

$$\mathbf{Q_i} = \begin{pmatrix} \cos(k_i) & k_i^{-1} \sin(k_i) \\ -k_i \sin(k_i) & \cos(k_i) \end{pmatrix} \tag{5.3}$$

is the tranfer matrix from one layer to the next one, and

$$k_i^2 + \omega^2 (n_i^2 - n_o^2 \sin^2 \theta_0) \tag{5.4}$$

is the wavenumber in the i-th layer. The angle θ_0 is the incident angle[12] which is assumed to be in the interval $[0, \pi/2)$, and ω is the light beam frequency.

An indication of the light transmission intensity is given by the penetration length ξ_p defined as:

$$\xi_p^{-1} = -\lim_{N \to \infty} \frac{1}{N} \ln |t_N|. \tag{5.5}$$

For $N >> 1$, $|t_N| \sim exp(-N\lambda_1)$, where λ_1 is the maximal Lyapunov exponent of the product[13] $\left[\prod_{i=1}^{N+1} \mathbf{Q_i}\right]$, so that $\xi_p = 1/\lambda_i$.

11 We chose as a probability distribution for n_i a standard gaussian distribution whit $\sigma \sim \Delta n$ of the MBBA

12 The angle between the incident light beam and the normal to the surface of the incidence

13 The maximal value for the Lyapunov exponent is $\sqrt{\pi}$, for a complete random system

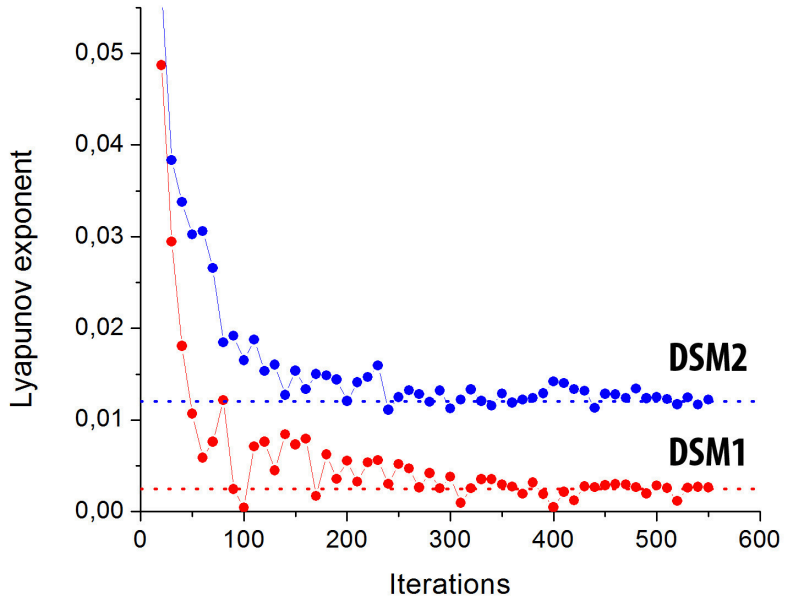

Figure 24: Lyapunov exponents computed by the model for the DSM1 case (red dots) and DSM2 case (blue dots). The numerical values converges to the experimental evaluated after 500 iterations.

From the bear law we know that $I \sim exp(-d/\ell)$ if we say that $d = Nb$ and we relate this result whit the Eq. for $|t_n|$ we found $\lambda_1 \sim b/\ell$. If we estimate λ_1 from the experimental data we obtain $\lambda \sim 0.0025$ for the DSM1 case and $\lambda \sim 0.012$. In Fig. (24) is reported a numerical evaluation of the model which is in perfect agreement whit the experimental results. The small value of the Lyapunov exponent, also in the DSM2 case, means that the system, apparently very chaotic, is much correlated as we can imagine!

6 CONFOCAL FLUORESCENCE MICROSCOPY OBSERVATION OF EHD

CONTENTS

6.1 History 43
6.2 Modern Confocal Microscopy 44
6.2.1 Fluorescence 44
6.3 Fluorescence Microscopy 45
6.4 How Does a Confocal Microscope Work? 46
6.5 3d Visualization 47
6.6 Other Consideration 48
6.6.1 Resolution 48
6.6.2 Pinhole Size 48
6.6.3 Intensity of Incident Light 49
6.6.4 Fluorophores 49
6.6.5 Photobleaching 49
6.7 Confocal Fluorescence Microscopy in EHD Instabilities 50
6.7.1 Clustering of Elastic Distortion Energy 51

A confocal microscope creates sharp images of a sample that would otherwise appear blurred when viewed with a conventional microscope. This is achieved by excluding most of the light from the sample that is not from the microscope's focal plane. The image has less haze and better contrast than that of a conventional microscope and represents a thin cross-section of the sample. Thus, apart from allowing better observation of fine details it is possible to build three-dimensional (3D) reconstructions of a volume of the sample by assembling a series of thin slices taken along the vertical axis.

6.1 HISTORY

Confocal microscopy was pioneered by Marvin Minsky in 1955 while he was a Junior Fellow at Harvard University. Minsky's invention would perform a point-by-point image construction by focusing a point of light sequentially across a sample and then collecting some of the returning rays. By illuminating a single point at a time Minsky avoided most of the unwanted scattered light that obscures an image when the entire sample is illuminated at the same time. Additionally, the light returning from the sample would pass through a second pinhole aperture that would reject rays that were not directly from the focal point. The remaining "desirable" light rays would then be collected by a photomultiplier and the image gradually reconstructed using a long-persistence screen. To build the image, Minsky scanned the sample by moving the stage rather than the light rays. This was to avoid the challenge of trying to maintain sensitive alignment of moving optics. Using a 60 Hz solenoid to move the platform vertically and a lower-frequency solenoid to move it horizontally, Minsky managed to obtain a frame rate of approximately one image every 10 sec.

6.2 MODERN CONFOCAL MICROSCOPY

Modern confocal microscopes have kept the key elements of Minsky's design: the pinhole apertures and point-by-point illumination of the sample. Advances in optics and electronics have been incorporated into current designs and provide improvements in speed, image quality, and storage of the generated images. Although there are a number of different confocal microscope designs, this entry will discuss one general type the other designs are not markedly different [46]. The majority of confocal microscopes image either by reflecting light off the sample or by stimulating fluorescence from *dyes* (*fluorophores*) applied to the sample. The focus of this entry will be on fluorescence confocal microscopy as it is the mode that is most commonly used in biological applications. The difference between the two techniques is small. There are methods that involve transmission of light through the sample, but these are much less common.

6.2.1 Fluorescence

If light is incident on a molecule, it may absorb the light and then emit light of a different color, a process known as fluorescence.

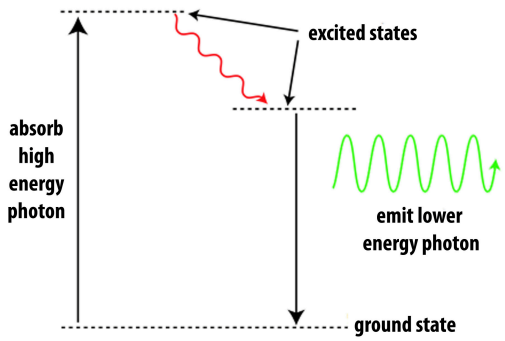

Figure 25: Mechanism of fluorescence. The horizontal lines indicate quantum energy levels of the molecule. A fluorescent dye molecule is raised to an excited energy state by a high energy photon. It loses a little energy to other molecules and drops to a lower excited state. It loses the rest of the energy by emitting light of a lower energy.

At ordinary temperatures most molecules are in their lowest energy state, the ground state. However, they may absorb a photon of light (for example, blue light) that increases their energy causing an electron to jump to a discrete singlet excited state [47]. In Fig. 25, this is represented by the top black line. Typically, the molecule quickly (within 10^{-8} sec) dissipates some of the absorbed energy through collisions with surrounding molecules causing the electron to drop to a lower energy level (the second black line).
If the surrounding molecules are not able to accept the larger energy difference needed to further lower the molecule to its ground state, it may undergo spontaneous emission, thereby losing the remaining energy, by emitting light of a longer wavelength (for example, green light)[48]. *Fluorescein* is a common fluorophore that acts this way, emitting green light when stimulated with blue excitation light. The wavelengths of the excitation light and the color of the emitted light are material dependent.

Microscopy in the fluorescence mode has several advantages over the reflected or transmitted modes. It can be more sensitive. Often, it is possible to attach fluorescent molecules to specific parts of the sample, making them the only visible ones in the microscope and it is also possible to use more than one type of fluorophore [49]. Thus, by switching the excitation light different parts of the sample can be distinguished.

6.3 FLUORESCENCE MICROSCOPY

In conventional fluorescence microscopy a dyed sample is illuminated with light of an appropriate wavelength and an image is formed from the resulting fluorescent light.

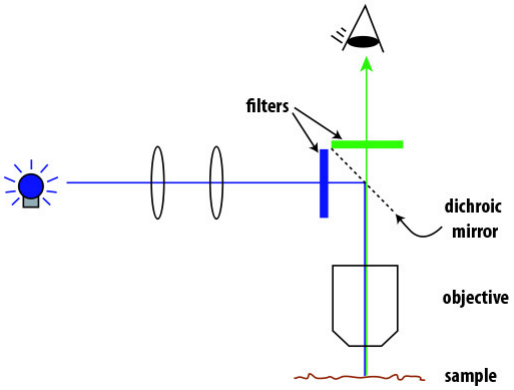

Figure 26: Basic setup of a fluorescence microscope. Light from the source is reflected off the dichroic mirror toward the sample. Returning fluorescence of a longer wavelength is allowed to pass through the dichroic mirror to the eyepiece.

In Fig. 26 the excitation light is blue and the emitted light is green. The microscope uses a dichroic mirror (also called a "dichromatic mirror") that reflects light shorter than a certain wavelength but transmits light of longer wavelength. Thus, the light from the main source is reflected and passes through the objective to the sample, while the longer-wavelength light from the fluorescing sample passes through both the objective and the dichroic mirror. This particular type of fluorescence microscopy, in which the objective used by the illuminating light is also used by the fluorescing light in conjunction with a dichroic mirror, is called epifluorescence. In the case of reflected light microscopy, a beam splitter is used in place of the dichroic mirror.

To understand confocal microscopy it is instructive to imagine a pair of lenses that focuses light from the focal point of one lens to the focal point of the other. This is illustrated by the dark blue rays in Fig. 27. The light blue rays represent light from another point in he sample, which is not at the focal point of the left-hand-side lens. Clearly, the image of the light blue point is not at the same location as the image of the dark blue point.

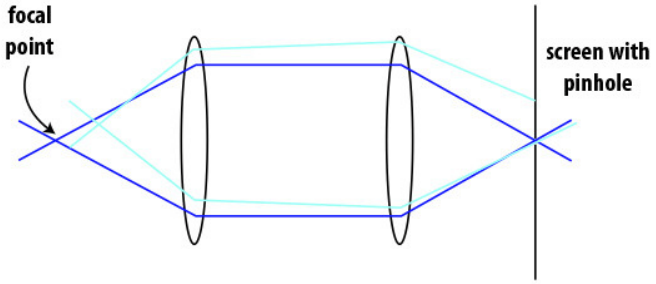

Figure 27: Rejection of light not incident from the focal plane. All light from the focal point that reaches the screen is allowed through. Light away from the focal point is mostly rejected.

In confocal microscopy, the aim is to see only the image of the dark blue point [50]. Accordingly, if a screen with a pinhole is placed at the other side of the lens system, then all of the light from the dark point will pass through the pinhole. Note that at the location of the screen the light blue point is out of focus. Moreover, most of the light will get blocked by the screen, resulting in an image of the light blue point that is significantly attenuated compared to the image of the dark blue point. To further reduce the amount of light emanating

from "light blue" points, the confocal microscope setup minimizes how much of the sample is illuminated. Normally, in fluorescence microscopy the entire field of view of the sample is completely illuminated, making the whole region fluoresce at the same time. Of course, the highest intensity of the excitation light is at the focal point of the lens, but the other parts of the sample do get some of this light and they do fluoresce. Thus, light at a "dark blue" point may include light that has been scattered from other "light blue" points, thereby obscuring its fluorescence. To reduce this effect the confocal microscope focuses a point of light at the in-focus dark blue point by imaging a pinhole aperture placed in front of the light source [50]. Thus, the only regions that are illuminated are a cone of light above and below the focal (dark blue) point.

Together the confocal microscope's two pinholes significantly reduce the background haze that is typical of a conventional fluorescence image. Because the focal point of the objective lens forms an image where the pinhole=screen is, those two points are known as "conjugate points" (or alternatively, the sample plane and the pinhole=screen are conjugate planes). The pinhole is conjugate to the focal point of the lens, hence the name "confocal" pinhole.

6.4 HOW DOES A CONFOCAL MICROSCOPE WORK?

The confocal microscope incorporates the ideas of point-by-point illumination of the sample and rejection of out-of-focus light. One drawback with imaging a point onto the sample is that there are fewer emitted photons to collect at any given instant. Thus, to avoid building a noisy image each point must be illuminated for a long time to collect enough light to make an accurate measurement [50]. In turn, this increases the length of time needed to create a point-by-point image. The solution is to use a light source of very high intensity, which Minsky did with a zirconium arc lamp. The modern choice is a laser light source, which has the additional benefit of being available in a wide range of wavelengths. In Fig. 28 the laser provides the intense blue excitation light. The light reflects off a dichroic mirror, which directs it to an assembly of vertically and horizontally scanning mirrors. These motor-driven mirrors scan the laser across the sample. Recall that Minsky's invention kept the optics stationary and instead scanned the sample by moving the stage back and forth in the vertical and horizontal directions. As awkward (and slow) as that method seems it does have among others the following two major advantages [51]:

- The sample is everywhere illuminated axially, rather than at different angles as in the case of the scanning mirror configuration, thereby avoiding optical aberrations. Thus, the entire field of view is illuminated uniformly.
- The field of view can be made larger than that of the static objective by controlling the amplitude of the stage movements.

In Fig. 28 the dye in the sample is excited by the laser light and fluoresces. The fluorescent (yellow) light is descanned by the same mirrors that are used to scan the excitation light (red) from the laser and then passes through the dichroic mirror. Thereafter, it is focused onto the pinhole. The light that makes it through the pinhole is measured by a detector such as a photomultiplier tube. In confocal microscopy, there is never a complete image of the sample because at any instant only one point is observed. Thus, for visualization the detector is attached to a computer, which builds up the image one pixel at a time. For a 512×512 pixel image this is typically done at a frame rate of $0.1 - 30$Hz. The image created by the confocal microscope is of a thin planar region of the sample, an effect referred to as optical sectioning. Out-of-plane unfocused light has been rejected, resulting in a sharper, better resolved image.

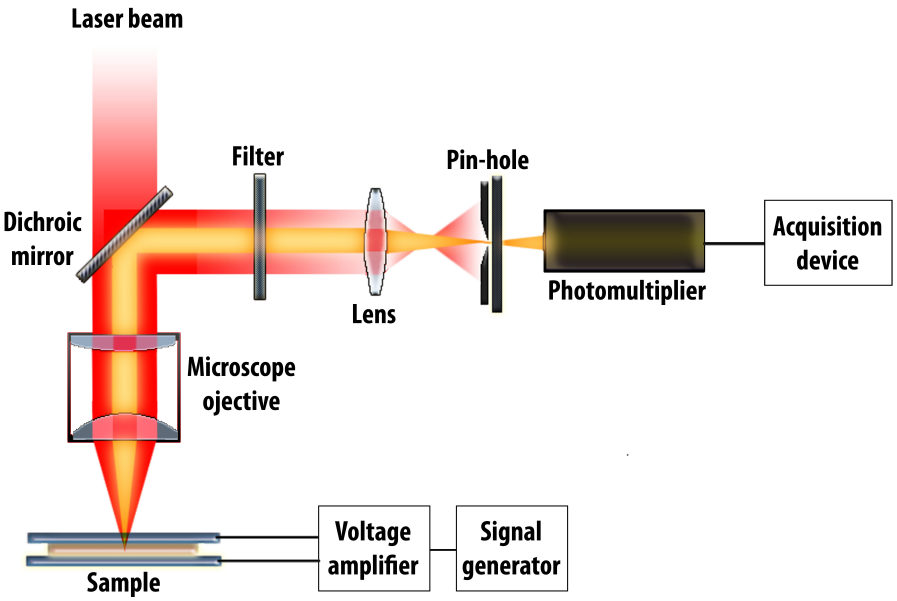

Figure 28: Basic setup of a confocal microscope. Light from the laser is scanned across the sample by the scanning mirrors. Optical sectioning occurs as the light passes through a pinhole on its way to the detector.

6.5 3D VISUALIZATION

The ability of a confocal microscope to create sharp optical sections makes it possible to build 3D renditions of the sample. Data gathered from a series of optical sections imaged at short and regular intervals along the optical axis are used to create the 3D reconstruction. Software can combine the 2D images to create a 3D rendition. Representing 3D information in a meaningful way out of 2D data is nontrivial, and a number of different schemes have been developed. Fig. 29 shows a 3D reconstruction, from slices of a suspension of 2µm diameter colloidal particles using "alpha blending" a technique that combines images by first making each of their individual pixels less or more transparent according to a computed weight called the "alpha" value [52]. The result is a 3D like structure.

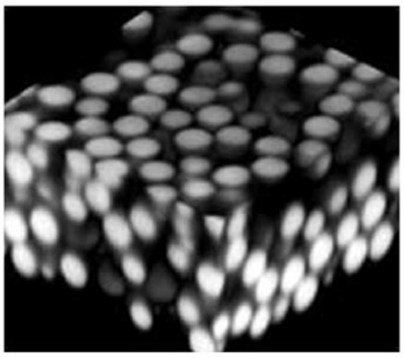

Figure 29: 3D reconstruction of a series of 2D images of *PMMA* spheres suspended in a cyclohexyl-bromide and decalin solution. The image was created using "alpha blending".

6.6 OTHER CONSIDERATION

A confocal microscope, as with every instrument, has some limitations and often compromises must be made to optimize performance. The following is an outline of some of the most important of them.

6.6.1 Resolution

As with conventional microscopy, confocal microscopy has inherent resolution limitations due to diffraction. In the discussion above it is assumed that the point source used produces a point of light on the sample. In fact it appears in the focal plane as an Airy disk, whose size depends on the wavelength of the light source and the numerical aperture of the objective lens [53]. (The numerical aperture of a lens is a measure of how well it gathers light.) The graph of Fig. 30B shows a plot of the intensity of light as a function of radius of an Airy disk the image is circularly symmetric, as shown in Fig. 30A.

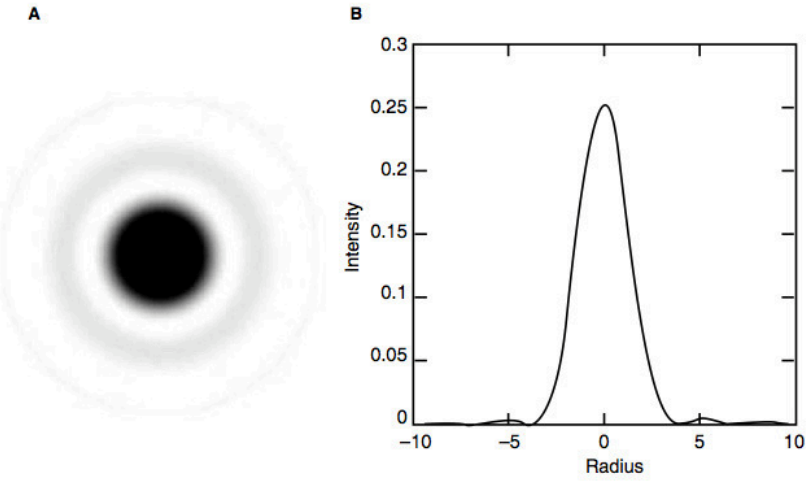

Figure 30: Airy disk similar to that of an image of a very small particle. (A) The image is "overexposed" and in reverse color to allow distinction of the faint secondary peak. (B) A graph of the intensity change with radius.

6.6.2 Pinhole Size

The optical sectioning capability of a confocal microscope derives from having a pinhole to reject out- of-focus light rays. In turn, the strength of the optical sectioning (the rate at which the detected intensity drops off in the axial direction) depends strongly on the size of the pinhole [49]. It is tempting to assume that making the pinhole as small as possible is the best choice. However, as the pinhole size is reduced, so too are the number of photons that arrive at the detector from the sample. This may lead to a reduced signal-to-noise ratio. To offset the weaker signal more fluorescence is needed from the sample. This usually can be done, to a limit, by raising the intensity of the excitation light. But high intensities can damage the sample, and in the case of fluorescence, also degrade the fluorophore. Moreover, it has been shown that optical sectioning does not improve considerably with the pinhole size below a

limit that approximates the radius of the first zero of the Airy disk [46, 49]. Thus, a good approximation is to make the pinhole about the size of the Airy disk.

6.6.3 Intensity of Incident Light

An important component of a confocal microscope is the photo-detector that captures light from the sample. In confocal fluorescence imaging the pinhole along with the optics preceding it significantly reduce the intensity of the emission that reaches the detector. Thus, the detector sensibility and noise behavior are vitally important [51]. The sensitivity is characterized by the quantum efficiency, which, as in any measurement involving quantum interactions, is limited by Poisson statistics [49]. That is, the accuracy of the measurement is improved by increasing the number of photons arriving at the detector. In practical terms this can be done by averaging data from many frames which has the drawback of slowing down the effective frame rate of the microscope. Or, it can be done by increasing the intensity of the fluorescence signal. Fluorescence can be increased by dyeing the sample with a larger concentration of fluorophore molecules or by raising the intensity of the excitation light. However, each of these methods increases excitation up to some limit. For high fluorophore concentrations, the individual molecules can quench each other [48]. They may also reduce the amount of fluorescence deep inside the sample - fluorophores nearest the light source can absorb enough light to significantly reduce the portion available to the rest of the sample[51]. Increasing fluorescence by increasing the excitation light intensity leads eventually to saturation of the fluorophore. Higher intensities drive a larger fraction of fluorophore molecules into excited states, which in turn leads to a smaller fraction of ground state molecules. Ultimately, the rate at which fluorophores are excited matches their decay rate, causing ground state depopulation. Fluorescence then ceases to increase with excitation intensity [54].

6.6.4 Fluorophores

Among the most important aspects of fluorescence confocal microscopy is the choice of fluorophore. It is typically influenced by several factors. The fluorophore should tag the correct part of the sample. It must be sensitive enough for the given excitation wavelength. For biological samples it should not significantly alter the dynamics of the organism; and an extra consideration is the effect of the sample on the fluorophore, its chemical environment can affect the position of the peaks of the excitation and emission spectra [51].

6.6.5 Photobleaching

A major problem with fluorophores is that they fade (irreversibly) when exposed to excitation light. Although this process is not completely understood, it is believed in some instances to occur when fluorophore molecules react with oxygen or oxygen radicals and become non-fluorescent [49, 54]. The reaction can take place after a fluorophore molecule transitions from the singlet excited state to the triplet excited state. Although the fraction of fluorophores that transitions to the triplet state is small, its lifetime is typically much longer than that of the singlet state. This can lead to a significant triplet state fluorophore population and thus to significant photobleaching [48]. Several strategies have been developed to reduce the rate of photobleaching [48, 54]. One method is to simply reduce the amount of oxygen that would react with the triplet excited states. This can be done by displacing it using a different gas [48]. Another method is by the use of free-radical scavengers to reduce the oxygen radicals. Shortening the long lifetime of the triplet excited state has also been shown to be effective [55]. Other ways include using a high numerical aperture lens to collect more fluorescence light

and thus use less excitation light [54]. Also, keeping the magnification as ow as is permissible spreads the excitation light over a larger area, thereby reducing the local intensity. While photobleaching makes fluorescence microscopy more difficult, it is not always undesirable. One technique that takes advantage of it is fluorescence photobleaching recovery (FPR) or fluorescence recovery after photobleaching (FRAP). It involves exposing a small region of the sample to a short and intense laser beam, which destroys the local fluorescence, and then observing as the fluorescence is recovered by transport of other fluorophore molecules from the surrounding region. Quantities such as the diffusion coefficient of the dyed structures can then be determined [56].

6.7 CONFOCAL FLUORESCENCE MICROSCOPY IN EHD INSTABILITIES

In this section the confocal fluorescence microscopy technique is applied to the study of EHD instabilities, in order to have information on dynamic at different z in the sample bulk. The sample analyzed in this work is a conventional cell containing a film of [N-(4-Methoxybenzyliden)-4-butylanilin] (MBBA) of thickness $d = 35\mu m$, planarly aligned a on plane (x, y), placed between two semitransparent electrodes. In order to induce EHD instabilities, a sinusoidal electric field $E = (0, 0, E_z)$, where $E_z = V_0/d$, is applied on the sample at a fixed frequency $f = 70$ Hz (V_0 is an external tunable voltage). The onset voltage for the Williams domain regime at frequency f is V_{th} = 11.1 V for the present sample. The profile of the NLC along the z direction was observed by encoding the sample with a gain medium (Pyrromethene 597 dye 0.3% wt), and scanned by confocal fluorescence polarization microscopy (Zeiss: LSM-510).

A small region of the original dataset along the z axis is reported in fig. 31 (top panel) for $V_0 = 11.1$ V where the transverse structure of WDs is evident. The z-profiles of further EHD convective structures observed for higher values of V_0 are shown in fig. 31. The increasing stochastic nature of the flow, as V_0 increases, involves the whole bulk, as can be seen from fig. 31. As V_0 increases small-scale structures are evidenced.

The dye molecules dissolved in the NLC at this concentration, proved to be completely miscible as evidenced by the absence of micro cluster, of dye embedded in the liquid crystalline phase [57, 58]. Confocal microscopes can acquire in-focus images from selected depths (a process known as optical sectioning), which allows a 3D reconstruction of topologically complex objects. Each pixel in the resulting image represents the detected light emitted by a volume element within the sample, when the dye molecules are stimulated by a light source. To this goal, a linearly polarized He-Ne laser (532 nm), was focused tightly inside the sample by a high numerical aperture (NA) objective lens, used as an optical pump. The thickness of the focal plane (namely the vertical spatial resolution) is then given by $\Delta Z \sim 1/(NA)^2$. The in-plane spatial resolution is defined as $\Delta X = \Delta Y \sim 1/NA$ The focal point of the laser scanned the three-dimensional volume, and the fluorescence from each point was selectively detected by a photomultiplier tube placed behind a pinhole, placed at a confocal configuration. The anisotropic molecular shape of dye molecules easily aligns itself parallel to the molecular director $\mathbf{n}(\mathbf{r})$ and follows the internal flow of EHD instabilities [57, 58, 75]. As the laser scans over the plane of interest, a section image $I(x, y)$ of the internal structure of the sample is acquired (Fig. 32). The intensity $I(x, y)$ is proportional to the average local distortion of the molecular director field $\mathbf{n}(\mathbf{r})$ [59, 60]. The result data set consist in a cube of size $L_X \times L_Y \times L_Z$ acquiredin 3D space($L_X \simeq L_Y \simeq 920\mu m$, $L_Z \simeq 35\mu m$).

The brightness of a resulting image pixel corresponds to the relative intensity of detected light. The image reconstruction is based on the larger absorption of the dye molecules along their symmetry axis [57, 59, 60]. Therefore, regions with high light intensity represent

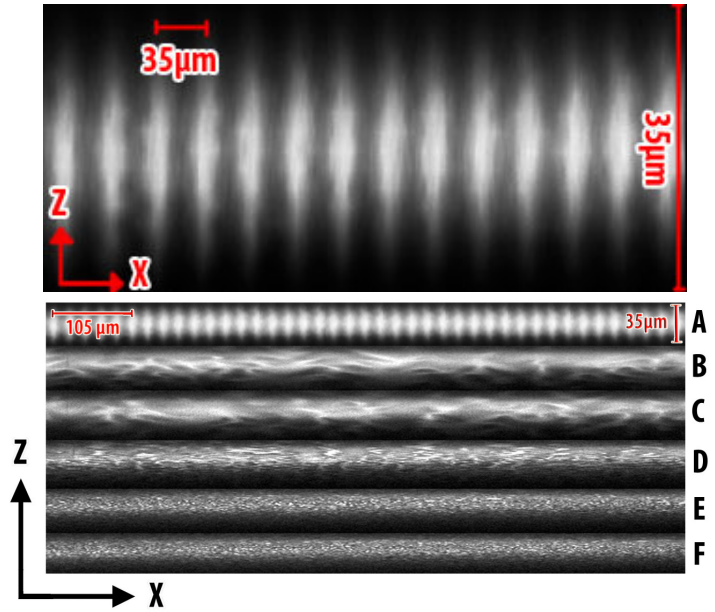

Figure 31: Top panel: Sample profile of NLC cell along the x, z plane obtained for $V_0 = 11.1$ V, by scanning the center of the sample cell in the y-direction, showing the transverse section of the WD rolls. Bottom panel: x, z profile of a 35μm cell encoded with fluorescent material Pyrromethene 597 dye 0.3%wt, for different values of applied electric field: A) $V_0 = 11.1$V, B) $V_0 = 25$V, C) $V_0 = 35$V, D) $V_0 = 40$V, E) $V_0 = 50$V, F) $V_0 = 70$V.

portions of volume in which the dye (and thus NLC) longer molecular axis is parallel to the polarization of the incident laser beam.

6.7.1 Clustering of Elastic Distortion Energy

Usual fluid flows are characterized by a cascade of kinetic energy from large to small scales where it is dissipated [76]. In the same framework a quantity of interest in the context of turbulent mixing is the dissipation of passive scalar fluctuations or the concentration of passive fields within fluid flows. It has been shown that these quantities do not fill homogeneously the whole space but are intermittently distributed as clusters. The complex dynamics leading to clusters is generally attributed to the presence of singularities of a measure which can be derived from experiments. In usual fluid flows, the rate of energy dissipation per unit volume is given by $\epsilon = \nu[(\partial u_i/\partial x_j) + (\partial u_j/\partial x_i)]^2$ (ν being the kinematic viscosity of the flow) where u_i and x_i are respectively the velocity and the spatial coordinate vectors. In general only time series of the longitudinal velocity field $v(t)$ are available from experiments, so that, through the Taylor's frozen flow hypothesis, the time derivative $\epsilon \sim \nu(dv/dt)^2$ is used as a surrogate for the turbulent dissipation rate [74]. Other measurements of passive scalar fluctuations as for example the temperature $T(x, y)$ or the concentration of passive contaminants in fluid flows measured in the physical space [70–72], are used to study the statistical properties of the dissipation field of the passive scalar fluctuations [71–73]. Once more the square of spatial derivatives $\epsilon \sim \kappa(\partial T/\partial x_i)^2$ (κ is the corresponding molecular diffusivity), are viewed as an experimental surrogate of the dissipation field. These measurements have been used to investigate the spatial concentration of the dissipation fields in fluid flows [70, 74] or the clustering of concentration of contaminants [71–73].

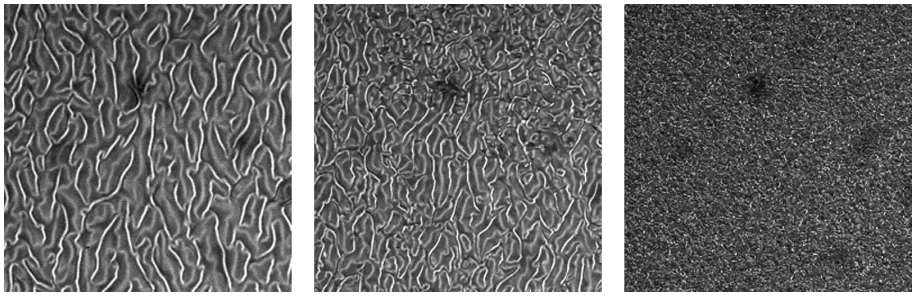

Figure 32: We report three snapshots of the flow structures I(x,y) for three different applied voltages $V_0 = 25$ V (left panel), $V_0 = 35$ V (middle panel) and $V_0 = 70$ V (right panel). The depth is $z = 0.07\mu$m.

The distortion free energy of a NLC is defined through the spatial derivative of the components of the molecular director $F = K(\partial n_i/\partial x_j)^2$ [36, 97] (K is the elastic constant in the one-constant approximation). Since the transmitted light intensity $I(x, y)$ is proportional to the average local distortion of the molecular director field, we conjecture that spatial derivative of $I(x, y)$ can be used to probe the local distortion of the molecular director. Then, once the data set $I(x, y)$ is acquired for each depth z, we define a 2D stochastic field

$$\Psi(x, y) = K \left\{ \left[\frac{\partial I(x, y)}{\partial x} \right]^2 + \left[\frac{\partial I(x, y)}{\partial y} \right]^2 \right\} \tag{6.1}$$

which, in the same spirit of the usual measurements in fluid flows, should represents a surrogate of the local distortion energy [75]. As a reference, in fig. 33 we show some snapshots of $\Psi(x, y)$ for three different values of the applied electric field V_0.

It is evident that the distortion energy is intermittent and does not fill uniformly the whole space, rather it is non-homogeneously distributed with large magnitudes concentrated in rather small spatial regions. In the following we will use the field $\Psi(x, y)$ as an empirical measure to investigate the statistical features and scaling behavior of the elastic distortion energy in EHD turbulence, at different values of the amplitude of the electric field and for different depths inside the sample. Since the measure of the local distortion energy is merely the small-scale manifestation of the chaotic dynamics associated to the behavior of EHD turbulence, the tendency of Ψ to concentrate in small regions of space allows us to investigate how the elastic energy density dynamically evolves into clusters in the various regimes.

Intermittent processes cannot be described efficiently by conventional statistics. For noisy processes that are close to be gaussian, it can be expected that a few low-order moments contain most of the information, while for processes of the type shown in fig. 33, it is clear that the first few moments give very little clue to their nature. It has been recognized that intermittent measures arising in nonlinear systems lend themselves to be characterized by multifractal geometry [68, 69]. Intermittency of energy dissipation [74] or clustering of passive fields in turbulent fluid flows [71, 72, 75], have been characterized in terms of their multifractal set in the position space [69, 71]. Following the same framework, here we consider the statistical behavior of a probability measure obtained from $\Psi(x, y)$ to investigate how the multifractal structure of clustering of elastic energy density changes during EHD instabilities at different depths z and different applied voltages V_0. One way to build up multifractals is to proceed from one scale to the next smaller ones (offsprings) in such a way that the measure contained by the large scale is unequally divided among the smallest offsprings. If the rule determining the nature of the division among small scales is independent

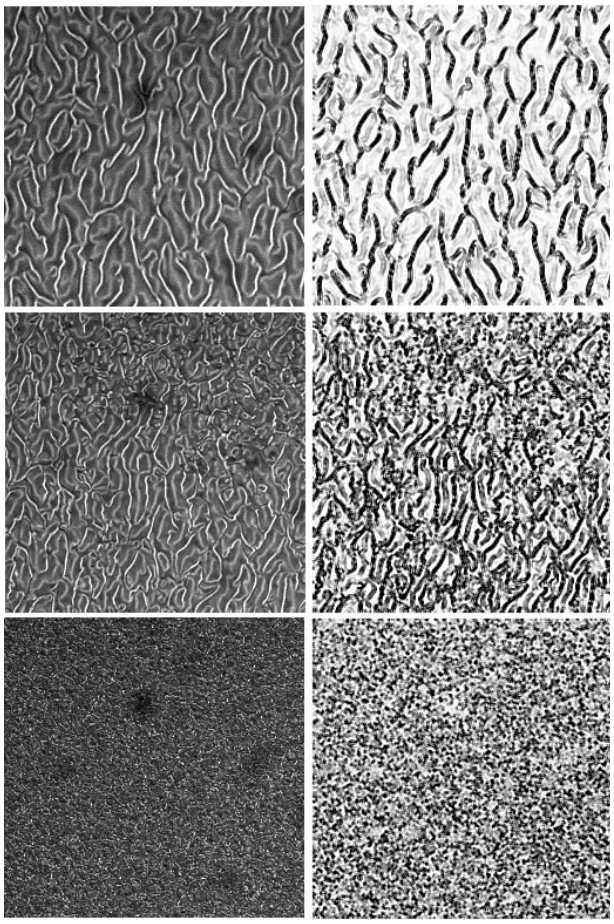

Figure 33: We report the contour plot of the flow structures $I(x, y)$ (left hand column) and the distortion energy density $\Psi(x, y)$ (right hand column), for three different applied voltages $V_0 = 25$ V (upper panels), $V_0 = 35$ V (middle panels) and $V_0 = 70$ V (lower panels). The depth is $z = 0.07$ μm.

of the generation level, one expect to see similar properties on all scales. Since the measure on an arbitrarily chosen offspring at any generation level is determined by the product of a series of multipliers, a multifractal is associated with a multiplicative process. In this sense it is clear that the scaling will only be local, that is multifractals are described by many scaling indices. A practical way of doing it, is to define a coarse-graining probability measure ρ_r by dividing the domain in which $\Psi(x, y)$ resides, into boxes $\Omega_i \in \Omega_L$ (Ω_L represents the whole space) of a certain size r and to write the total amount of distortion energy on each of these boxes

$$\rho_r = \int_{\Omega_i} |\Psi(x, y)|^2 dx dy \tag{6.2}$$

The typical behavior of the probability measure scales as a power law $\rho_r \sim r^{\alpha(x_i, y_i)}$, where (x_i, y_i) is the center of the box in the space in which the multifractal is embedded. This expression comes from the fact that we expect α to be the dimension of the embedding space of dimension $d = 2$. For pure fractals α can have non integer values, and in the case of a global scaling law, one expect that α is constant and independent on position of the box. On

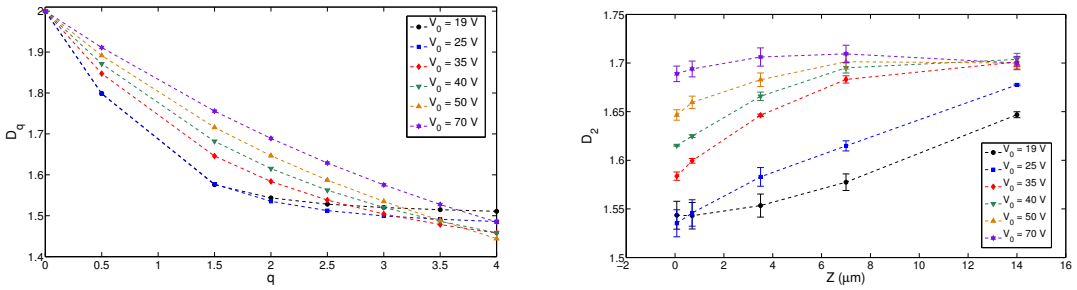

Figure 34: Left panel: the singularity spectrum D_q as a function of q is reported for different values of the applied voltage V_0. Measurements are performed at $z = 0.07$ μm. Rigth Panel: The correlation dimension D_2 is reported as a function of the depth z for different applied voltages V_0,selecting several chaotic dynamics.

the contrary multifractals are characterized by interwoven sets of varying dimensionality so that α depends on the position [68, 69]. The scaling exponent α is related to singularities of the density of elastic energy, defined as the total amount of elastic energy in a box of size r divided by the surface of the box $\xi_r \sim r^{\alpha-2}$. In fact, whenever $\alpha < 2$ the density increases indefinitely as the box size shrinks, and locally represents singular regions namely spikes in the distribution of ξ_r, the "strength" of singularities being measured by the value of α.

From a computational point of view [68] it can be shown that singularities of strength α can be described by the scaling of the q-th moments of the normalized coarse-grained measure

$$\frac{\langle \rho_r^q \rangle}{\rho_L^q} \sim r^{(q-1)D_q} \tag{6.3}$$

ρ_L is the integral of the measure over Ω_L and brakets mean space averages. In eq. (6.3) the scaling exponents D_q are called generalized dimensions, related to the singularity strength by $\alpha = d/dq[(q-1)D_q]$ [69]. The method of moments is the simplest way to probe the multifractality of the measure. The meaning of rising the measure ρ_r to a power q to study multifractals, is that if q is positive and large, only the large intensity regions will be picked by the average in (6.3). As a consequence, for a simple fractal $D_q = const.$ independent on q. On the contrary, different values of D_q as q increases, probes the singularities of the different interwoven set of which a multifractal is made. According to eq. (6.3), if log-log plots of $[< \rho_r^q > /\rho_L^q]^{1/(q-1)}$ vs. r presents linear regions, for r within a certain scaling range, then the slopes corresponds to D_q.

We performed the analysis of moments for various values of q, and in fig. 34 (left panel) we report the values of D_q as a function of q obtained for different values of the applied voltage V_0, for a given depth $z = 0$ (the behavior is the same for different z). Clusters described by multifractals are observed for all values of V_0, say different values of D_q are recovered as q increases [68]. However a careful analysis show that D_q saturates as q increases, for lower values of V_0, while the dimension of the set where clusters lie decreases as q increases, for higher values of V_0. This means that, when turbulence appears in the NLC, the elastic energy density becomes singular, at variance to static structures where clusters are probably defined by a given scale. Of particular interest is the second–order statistic, the correlation dimension D_2,which is related to the probability of finding two structures close to each other. In fig. 34 (right panel), we report the values of D_2 as a function of the depth z for different V_0. In this case D_2 increases as V_0 increases, but it saturates going inside the NLC for higher values of V_0. On the contrary D_2 increases going inside the NLC for non turbulent regimes.

Indicating that the bulk sample is much less influenced by the anchoring energy with respect the boundary glass plates.

As a further measure of clustering let us consider the probability density function (pdf) $P(\mu_r)$ of the normalized coarse–grained density $\mu_r = \rho_r / \sqrt{\langle \rho_r^2 \rangle}$, and in fig. 35 we report this quantity for different scales r and two different applied voltages.

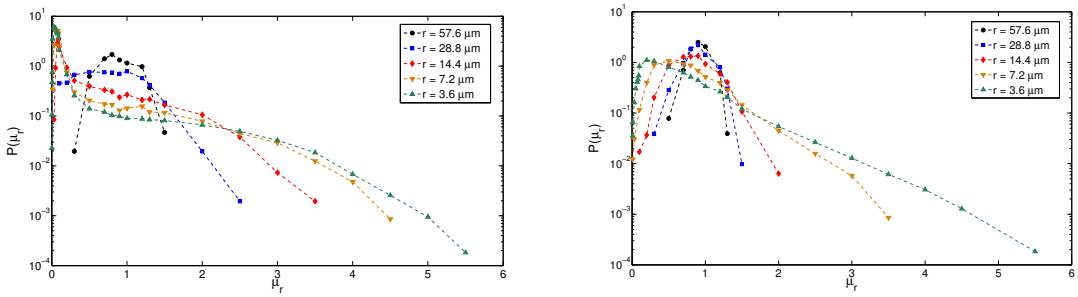

Figure 35: The pdfs of the normalized density measure μ_r are reported for different coarse-graining scales r. Left panel refers to an applied voltage $V_0 = 19$ V, right panel refers to $V_0 = 70$ V. Measurements are perfomed at $z = 0.07$ μm.

The evolution towards the clustering structure is evident as the scale r becomes smaller. In fact one observes that the deviation from a uniform distribution is maximum at small scales and that the distortion energy distribution approaches uniformity when r increases. It is clear from fig. 35 that the pdf associated with two different scales r do not differ only through a scaling factor. The pdf of the coarse-grained density has noticeable characteristics that gives insights on the mechanisms leading to energy density clustering. Both tails (at low and high values) are much wider than that we would expect from a uniform distribution (see fig. 36).

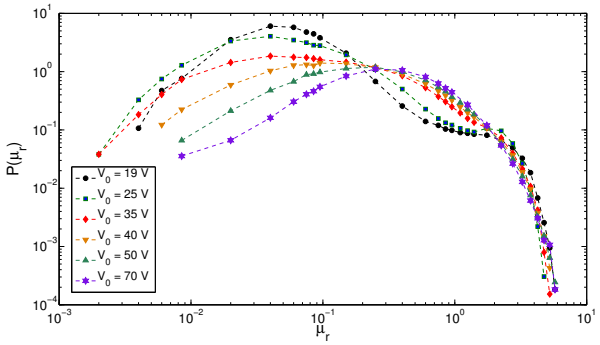

Figure 36: The pdfs of the normalized density measure μ_r are reported for different applied voltages V_0 for $z = 0.07$ μm and $r = 3.6$ μm.

This implies that, on the one hand, it is more probable to observe a region where elastic energy is highly concentrated, but on the other hand it is also probable to observe a region where the distortion energy is smooth. For small applied voltages, when the turbulence is far from being fully developed, a characteristic structure is clearly observed for small r, while in the turbulent regime the large–density tail decreases exponentially at small scales.

What happens to pdfs as the depth z is increased, is shown in fig. 37, where we report $P(\mu_r)$ for different depths and two different applied voltages. Going inside the sectioning, we

observe the tendency towards an exponential decay for the large density tail. This evolution is well visible when the turbulence is not developed, and is due to the fact that the sharp structures forming clustering in the bulk are not influenced by the glass surfaces. On the contrary, when the turbulence is fully developed, the first layers under the glass surfaces are involved in the turbulent clusterization of elastic energy density. This gives the same pdfs for each layer observed.

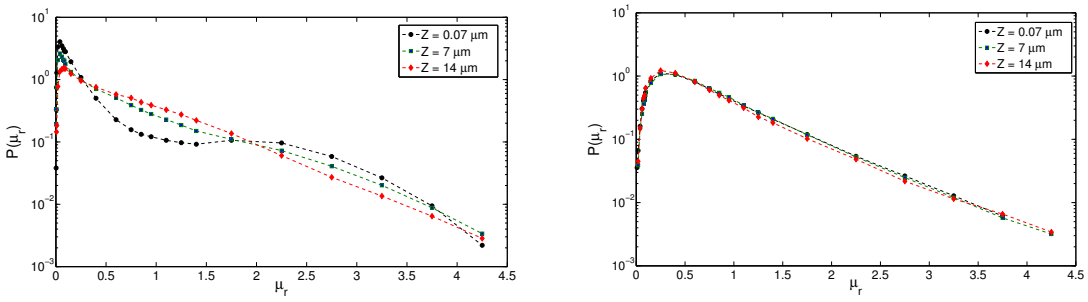

Figure 37: The pdfs of the normalized density measure μ_r are reported for different depths z and two voltages: $V_0 = 25$ V (left panel), $V_0 = 70$ V (right panel). In both cases $r = 3.6$ µm.

7 ANOMALOUS SCALING OF INTENSITY FLUCTUATIONS DISTRIBUTION IN EHD

CONTENTS

7.1 Intermittency 57
7.1.1 The PDF Within the K41 Framework 59
7.1.2 The PDF for a Simple Intermittency Model 59
7.2 Probability Density Function of Intensity Fluctuations 61
7.2.1 A Model for the Scaling Behavior of PDFs 62
7.3 Scaling of EHD Turbulence 62

The main characteristic of turbulence in usual fluid flows is the generation of high amplitude fluctuations on all dynamically interesting spatial and temporal scales, giving rise to scale-free relationship for statistical quantities of some interest [76–78]. On the basis of experimental results [79–82] and numerical simulations [83, 84], it is nowadays accepted that scaling behaviours are anomalous with respect to the Kolmogorov phenomenology [78]. This seems to be a universal characteristic of turbulent flows, being observed also in complex fluids, like for example turbulent astrophysical flows [85–87] and charged particle flows [91, 92]. Most experimental results [93–96] have shown that the deviation from a Kolmogorov-like phenomenology is stronger in anisotropic flows. The process leading to anomalous scaling is usually called intermittency [78], which manifest itself through a lack of global self-similarity, evidenced by the scaling behavior of probability density function (PDF) of fluctuations. In fact, PDFs of field fluctuations across the scale r change shape with the scale, evolving from quasi-Gaussian at large scales, to stretched exponential tailed distribution at small scales. In usual fluid flows, this has been associated with the inhomogeneous distribution of turbulent energy dissipation rate [78]. In complex fluid flows, dissipation properties are different from usual fluids, so that the presence of intermittency can be due to structures associated with large local gradients [85–87, 91, 92].

Liquid crystals represent an experimental example of anisotropic fluids displaying complex spatio-temporal behavior [36, 97], a typical case where the system is driven far from equilibrium. Spatio-temporal turbulence (in terms of irregular patterns and chaotic dynamics) can be observed in nematic liquid crystal (NLC) films experiencing electrohydrodynamic (EHD) instabilities.

7.1 INTERMITTENCY

Intermittency has several meanings in turbulence, but the most interesting one for the purpose of this meeting is the tendency of the probability distributions of some quantities (*i.e.* velocity gradients, scalar quantities ecc.) to develop long tails of very strong events. This leads to strong deviations from Gaussian statistics that become larger and larger when considering fluctuations at smaller and smaller scales.

In three-dimensional hydrodynamic turbulence, the origin of these deviations has been ascribed to the formation of coherent structures (strong vortices) since the 1950s. However, the physical mechanism of intermittency is still an open question. Intermittency has also

been observed in granular systems [4], in magnetohydrodynamic turbulence in geophysics or in the solar wind, and in systems involving transport by a turbulent flow. The question is rather that the extreme tails become stronger as the Reynolds number increases, and that the trend does not show any sign of stopping at the highest experimental Reynolds numbers.

This is not altogether surprising, because turbulence is believed to be singular in the limit of infinite Reynolds numbers. In an equilibrium system, global energy conservation implies that the energy input should be equal to the average viscous dissipation per unit mass

$$\langle \epsilon_\nu \rangle = \nu \langle |\nabla \mathbf{v}|^2 \rangle \tag{7.1}$$

where ν is the kinematic viscosity of the fluid, and $\langle |\nabla \mathbf{v}|^2 \rangle$ is the L_2 norm of the velocity gradient tensor. The average is taken either over the whole flow or over a suitably designed ensemble of experiments. The basic experimental observation in turbulence is that the energy input required to maintain a turbulent flow becomes independent of the viscosity if the Reynolds number is high enough. In the limit of $\nu \to 0$, this implies that the velocity field has to develop infinite gradients. The observation of intermittency goes beyond that singular behavior and implies that strong gradients become more common as the Reynolds number increases, even when measured in terms of their r.m.s. values. In particular, all the higher statistical flatness factors of the velocity gradients are thought to diverge in the inviscid limit. Intermittency is not limited to gradients. Turbulence is a multi-scale phenomenon, in which the ratio between the largest and the smallest length scales can reach $10^5 - 10^6$. The fundamental problem is to understand how large-scale quantities, such as the energy, are transported across that range of scales to the smallest eddies, where they can, for example, be dissipated. The generally accepted model is the cascade, introduced by Richardson [1920], which states that eddies of a given size only interact with those of somewhat larger or somewhat smaller sizes. Any interaction between eddies of very different sizes takes places through a sequence of such small cascade steps. It is clear that, even if the underlying equations are deterministic, a phenomenon as complex as turbulence has some components that can best be described as random. In fact, when the physical consequences of the cascade were first explored by Kolmogorov [1941], he assumed that the process was complex enough for the eddies to lose all the memory of their previous histories, and that their properties after each cascade step could be described by purely random distributions. It then follows that there is an 'inertial' range of scales in which the eddies are too large for viscosity to be important, and too small to retain any effect of large-scale inhomogeneities. The Navier-Stokes equations are invariant to scaling transformations in that range, and the probability distributions of, for example, the velocity differences within an eddy, can only depend on the eddy size.

Consider for example the velocity difference Δv between two points separated by a distance r. The original Kolmogorov formulation assumes that the probability density function (PDF) $P(\Delta v)$, is a universal function in the inertial range of scales, whose only parameter is a velocity scale depending on r. It then follows from energy conservation arguments that

$$P(\Delta v) = F\left[\Delta v / (\langle \epsilon \rangle r)^{1/3}\right], \tag{7.2}$$

where $\langle \epsilon \rangle$ is the average energy transfer rate across scales per unit mass. In an equilibrium system, it has to be equal to ϵ_ν.

Equation 7.2 is valid as long as the separation r is much larger than the Kolmogorov viscous cutoff $\eta = (\nu^3/\langle \epsilon \rangle)^{1/4}$, and much smaller than the integral scale of the largest eddies $L_\epsilon = v'^3/\epsilon$, where v' is the root-mean-square value of the fluctuations of one velocity component. The extent of this inertial range is a function,

$$L_\epsilon/\eta = Re_L^{3/4}, \tag{7.3}$$

of the Reynolds number $Re_L = v' L_\epsilon / \nu$.

7.1.1 The PDF Within the K41 Framework

The key argument is quite simple: the viscous cutoff and the velocity gradient have a *nonlinear* dependence on the velocity amplitude of large-scale eddy motion; if the latter has fluctuations, for example with Gaussian statistics, so will the former, but of course with a different pdf. Specifically, let us assume that the turbulence is homogeneous and isotropic. the velocity v_0 characteristic of large *eddies* is assumed to have fluctuations with a pdf $P_v(v_0)$. The integral scale l_0 is taken to be unity. In the K41 theory the velocity increment $v_l(r) = v(r+l) - v(r)$ behaves, for l in the inertial range, as

$$v_l(r) \sim v_0 l^h, \tag{7.4}$$

with $h = 1/3$ for any r. The viscous cutoff[1] is obtained by equating the turnover time $t_l = l/v_l$ and the diffusion time l^2/ν, where ν is the kinematic viscosity. Hence

$$\eta \sim (\nu/v_0)^{3/4}. \tag{7.5}$$

The velocity gradient, which will be denoted by s (for *strain*) is given by

$$s \sim v_\eta/\eta \sim v_0^{3/2}\nu^{-1/2}. \tag{7.6}$$

Eq. 7.6 defines a nonlinear change of variable from v_0 to s. It is follows that the PDF P_s of the velocity gradients is given by

$$P_s(s) \sim \nu^{1/3} s^{-1/3} P_v(\nu^{1/3} s^{-1/3}). \tag{7.7}$$

If, for example, we choose P_v to be a Gaussian, as suggested by experimental data for homogeneous turbulence. we obtain for the pdf of velocity gradients a modified exponential law involving a 4/3 power of the argument and a $s^{-1/3}$ prefactor. Kraichnan (1990) obtained an ordinary exponential form for the tail of P_s (with an $s^{-1/2}$ prefactor). He also made use of a nonlinear transformation (the "mapping closure"). The quality of present experimental and numerical data may not allow to unambiguously discriminate between the ordinary and the modified exponential laws. Still, Kraichnan's expression for the PDF leads to difficulties at high Reynolds numbers: the mean dissipation $\nu\langle s^2\rangle$ does not become independent of ν for $\nu \to 0$, a property which is however satisfied by Eq. 7.7.

Numerical evidence of a strong correlation between high-amplitude fluctuations of velocity and the vorticity has been recently reported by Brachet (1990). who has conducted a high-Reynolds number direct simulation of the Taylor-Green vortex flow. Note that if coherent structures are present, the velocity distribution PI' may differ markedely from Gaussian.

7.1.2 The PDF for a Simple Intermittency Model

To take in account the effects of intermittency we shall modify the above analysis (β-model). For simplicity we assume that there is a single scaling exponent and a single dimension. It is now assumed that Eq. 7.4 holds with a scaling exponent $h \neq 1/3$, but only when $r \in S$, where S is a set of fractal dimension $D < 3$. The relation

$$3 - D = 1 - 3h \tag{7.8}$$

1 the Kolmogorov dissipation scale η

is assumed to ensure a finite energy dissipation in the limit $\nu \to 0$. It is convenient to parameterize both D and h in terms of the intermittency parameter $\mu = 3 - D$, the co-dimension of dissipative structures. The same argument which led to the viscous cutoff 7.5 gives now an h-dependent cutoff

$$\eta \sim (\nu/\nu_0)^{1/(1+h)} \tag{7.9}$$

The velocity gradient is now given by

$$s \sim \nu_\eta/\eta \sim \nu^{(h-1)/(h+1)}\nu_0^{2/(h+1)}. \tag{7.10}$$

In order to find the pdf of the velocity gradient s, it is not enough to perform the nonlinear change of variable implied by Eq. 7.10. We must also take into account the fact that the fractal set S, smoothed over a distance η, fills a fraction of space given by

$$p \sim \eta^{3-D}. \tag{7.11}$$

Outside of the η-smoothed fractal set, there is no appreciable small-scale activity and we can set the velocity gradient to zero (in comparison to the values it achieves in active regions). Thus, for a fixed value of ν_0 we obtain the following PDF for the velocity gradient:[2]

$$P_s^{ua}(s') \sim (1-p)\delta(s') + p\delta(s'-s), \tag{7.12}$$

with p given by Eq. 7.11 and SsS given by Eq. 7.10. Averaging now over the PDF P_ν of $u\nu_0$, we obtain

$$P_S(s) \sim (\nu/s)^{(1+2\mu)/3} P_\nu(\nu^{(2+\mu)/6} s^{(4-\mu)/6} + \gamma\delta(s), \tag{7.13}$$

where γ is determined by the condition that the integral of $P_s(s)$ be normalized to unity.

If again we specialize to a Gaussian $P_\nu p$, we obtain for the PDF of velocity gradients a modified exponential law with a power $(4-\mu)/3$ of the argument. For $\mu = 1$, when the dissipative structures are sheet-like ($D = 2$), we obtain an ordinary exponential law (except for the δ-function term).

It is easily checked that, for any μ, the mean dissipation $\nu\langle s^2\rangle$ is independent of the viscosity.

Moments of the velocity gradient of arbitrary order are easily evaluated. Their scaling dependence on the viscosity is not affected by the functional form of P_ν Hence, results for skewness and flatness are the same as given by Frisch, Sulem and Nelkin (1978) for the β-model which ignores fluctuations of ν_0 As long as $\mu > 0$ the skewness and flatness increase indefinitely with the Reynolds number.

Numerical data from fully resolved turbulence simulations, such as the 240^3 pseudo-spectral simulation, suggest that the PDF of velocity gradients is a modified exponential with a power of the argument slightly lower than one. This is consistent with the model proposed above if we take μ to be somewhat greater than one, and correspondingly $D < 2$. Geometrically, it corresponds to more filament-like than sheet-like turbulent structures. Such structures have indeed been visualized in direct numerical simulations of turbulence fields. The present argument has however a difficulty: $D < 2$ implies a negative exponent h. This difficulty can be overcome if the interaction between the coherent vortex structures and a background stochastic field is taken into account.

2 the superscript "ua" stand for" unaveraged"

7.2 PROBABILITY DENSITY FUNCTION OF INTENSITY FLUCTUATIONS

In turbulence studies, it is customary to analyze the flow properties through the representation given by the field differences estimated at different lags, which represent a probe for turbulent structures at a given scale. Here, we study a sample of NLC in various EHD regimes using the tools developed for ordinary fluid turbulence. Therefore, once the data sets is acquired as described in previous section, for each depth z we represent the intensity fluctuations at a given scale r through the differences at various lags r (see Fig. 2). This is done by defining both the transverse $\delta_x I(\mathbf{x}, r, z) = I(x + r, y, z) - I(x, y, z)$ and longitudinal $\delta_y I(\mathbf{x}, r, z) = I(x, y + z, z) - I(x, y, z)$ fluctuations with respect to the directions of the original Williams convective rolls axis (the y axis in our reference system), which introduces anisotropy. In order to study the statistical properties of the field, we evaluate the PDFs $P_r(\Delta_s I)$ ($s = x, y$) of normalized fluctuations at a given scale r

$$\Delta_s I(\mathbf{x}, r, z) = \frac{\delta_s I(\mathbf{x}, r, z)}{\sqrt{\langle |\delta_s I|^2 \rangle}} \tag{7.14}$$

(brackets being averages over space for a fixed depth z and lag r). It is easy to show that global self-similarity requires that PDFs superposes at different scaling r (see Fig. 38).

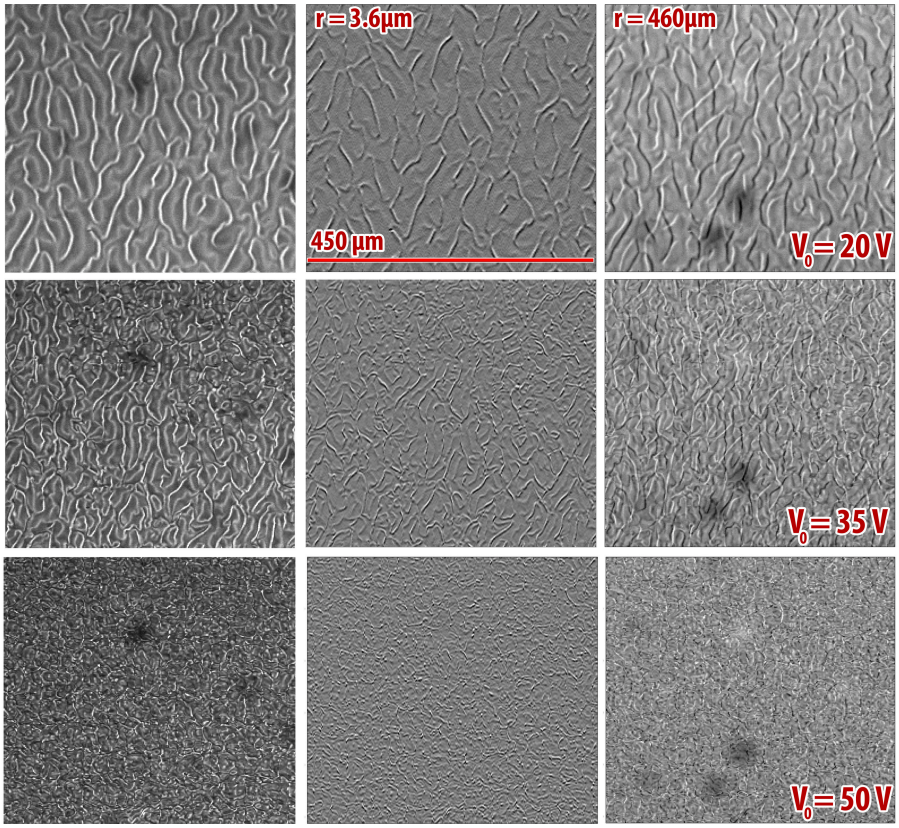

Figure 38: Snapshots of $\delta I_x(\mathbf{x}, r, z)$ at $z = 0.14\mu m$ for different values of V_0 and different lags r. The original snapshots have been cut at $L_X \simeq L_Y \simeq 450\mu m$.

The scaling behavior of PDFs, for different depths z and different voltages V_0, is shown in figs 39 and 40. PDFs are nearly Gaussian at large scales, while they show rising tails at smaller and smaller scales. This indicates that, at small scales, strong fluctuations have higher probability of occurrence than if they were Gaussian distributed random events. Thus, some degree of correlation is present in the field due to structures, which accumulate at smaller scales. This is similar to the typical behavior of intermittency in fully developed turbulence [78, 101, 102]. It should be noticed that, at variance with usual fluid flows, in some cases we found that PDFs of field fluctuations show a quasi-Gaussian core with superposed enhanced tails. This is the case at low voltage, namely for $V_0 = 20 \div 25$V, at all depths and scales for the y direction increments, and at $z = 0.14\mu$m for large and intermediate scales, for the increments in the x direction. This is probably due to the presence of a distinct population of structures boundaries in the sample, evident at low voltage, whose occurrence will be taken into account when analyzing the PDF shape.

7.2.1 A Model for the Scaling Behavior of PDFs

In order to quantify the scaling properties of PDFs shown in Figures 39 and 40, we fit the measured distributions with a model PDF, originally developed for fluid turbulence [101], and successfully used in other contexts [103–107]. In the multifractal framework of the turbulent energy cascade [78], PDFs of the field increments at a given scale are considered as the result of a continuous superposition of parent distributions, characterized by the same functional shape but different parameters, describing the statistics of the field inside disjoint subsets of the field. The model PDFs are then built as the convolution of the parent distribution, usually the large-scale one, with the theoretical or experimental weights distribution [104]. In the present case, from the observation of curves in Figures 39 and 40, the parent distribution is a Gaussian $G_\sigma(\Delta_s I)$, σ being the variable standard deviation ($s = x, y$).

The scale-dependent weights PDF is introduced in the model as the distribution of the standard deviations $L_{\lambda(r)}(\sigma)$, characterized by its width parameter $\lambda(r)$, so that the resulting PDF is

$$P_r(\Delta_s I) = \int G_\sigma(\Delta_s I) * L_{\lambda(r)}(\sigma) d\sigma \,. \tag{7.15}$$

For those systems in which the relationship between the variances and some observables is known, the function $L_{\lambda(r)}(\sigma)$ can be obtained from the data. When this is not possible, a theoretical ansatz is necessary. In the present case we propose to use the typical Log-normal function [101, 107], usually suggesting the presence of a multifractal, nonlinear multiplicative cascade in the process. With this choice,

$$L_{\lambda(r)}(\sigma) = \frac{1}{\sqrt{4\pi}\lambda(r)} \exp\left(-\frac{\ln^2 \sigma}{2\lambda^2(r)}\right). \tag{7.16}$$

The scale dependent log-variance $\lambda(r)$ determine the shape of the global PDF. For example, for $\lambda = 0$ the Log-normal PDF is a δ-function, so that the convolution (7.15) gives a Gaussian. As $\lambda(r)$ increases, the convolution includes more and more different values of σ, so that the tails of the PDF raise.

7.3 SCALING OF EHD TURBULENCE

In fully developed turbulence, the inertial range is characterized by power-law scaling of the parameter $\lambda(r)$. This is related with the multifractal properties of the flow [101, 107]. In

the present case, where a model for scaling fluctuations of turbulence does not exist, the same parameter can be used to quantify the degree of non-Gaussianity of the statistics, and therefore to represent the scaling properties of the field fluctuations. Figures 41 and 42 show the parameter $\lambda(r)$ obtained from the fit of PDFs for different values of V_0 and z.

Top panels show the variation of λ with the scale r. At low voltage $V_0 = 20V$, the large values of λ at small scales indicate high tails of the PDF, corresponding to the presence of strongly localized structures. The observed small scale values are comparable for all depths. We remind the reader that, for $z < 10$ μm for the perpendicular fluctuations, and at all depths for parallel fluctuations, a double distribution, including the model distribution and a superimposed Gaussian, has been used to capture separately the Gaussian core and the enhanced tails in the statistics. In the perpendicular case, for scales approximately $r > 15$ μm a rapid decrease of λ is observed, indicating quasi-Gaussian background field. The sharp transition in the parameter suggests the presence of a characteristic scale in the process. From this observation, we conclude that the small scale statistics is dominated by the presence of structures representing the boundaries of the non-interacting Williams convective rolls, characterized by size $r \simeq 15\mu m$, and embedded in a Gaussian background, so that at larger scales the correlation is lost. This is in agreement with previous results on the same sample [75, 98]. The same holds for the parallel direction, where, however, the values of λ are affected by the presence of the superposed Gaussian, whose presence dominates the statistics, especially at large scales and depths.

For both increment directions, at $V_0 = 35V$ the parameter has a smooth decrease from the high small scales values to a saturation level, reached for $r > 15\mu m$. The small scale variation indicate presence of intermittency, suggesting that in this regime the dynamics of the liquid crystal is characterized by nonlinear interactions generating small scale structures through a multiplicative process, which resemble the typical cascade in usual fully developed turbulence. The saturation values of λ are non-Gaussian, so that even at large scales the random background interacts with the structures (reminder of the Williams rolls) generating large fluctuations of the field. This regime is therefore closer to a case of fully developed turbulence. Values of λ depend on the layer depth, so that non-Gaussianity is larger closer to the top boundary. Such difference could be due to the anisotropic anchoring effect (glass-NLC interface) of a treated solid surface on a nematic liquid crystal [36]. In fact, the surface anchoring is usually anisotropic; more specifically, the anchoring tends to be stronger in the polar rather than in the azimuthal direction and the dynamic is anisotropically influenced down to the extrapolation length scale (about 3μm in this case). Finally, at $V_0 = 70V$ PDFs are almost identical at all scales, with a slow decrease toward large scales. However, at variance to usual fluid flows, values of λ indicate non-Gaussian statistics, so that coherent structures are still present in the field on all scales. These can be interpreted as weak residuals of the original Williams rolls and could represent structures generated by the fluid motions at high voltages [98]. On the other hand, the lack of scaling variation of the parameter suggests the absence of inhomogeneities (namely strongly localized structures) in the flow, so that the structures present in the field are quite similar at all scales.

Central panels of Figures 41 and 42 show the variation of the fit parameter λ with the depth z, for the three values of V_0 already represented, and at two different scales r. In all cases, non-Gaussian properties are stronger near the glass plate, where wall effects keep the molecules more structured. The statistical properties of the intensity fluctuations depend therefore on the depth in the cell, which is in agreement with fluid convective models [36, 97]. Notice that the gap between the two curves at different lags r provides a quick visual estimate of the range of variation of the PDF shape, indicating the degree of intermittency. As already pointed out, the high voltage regime (DSM2, at $V_0 = 70V$) shows non-Gaussian statistic, but weak intermittency, the two curves being only slightly different. The largest degree of intermittency is seen in the WT regime ($V_0 = 35V$) for the perpendicular fluctuations, and at low voltage for the parallel fluctuations (where however the extra Gaussian contribution in

present at all scales). This confirms that the WT regime is a turbulent regime similar to fully developed turbulence in fluid flows, DSM regimes being more similar to what we expect from a field, stochastically evolving both in space and time, filled by the same degree of structures on all scales (e.g., a energy dissipation rate in turbulence [78]).

In bottom panels of Figures 41 and 42, the variation of λ with the voltage V_0 is shown. As before, plots refer to three different depth z, at two different scales r. Near the wall ($z = 0.14$ μm) the two curves are separated by a small gap, indicating some degree of intermittency, which however decreases with increasing voltage. The curves behaviour is similar at small and large scale. Conversely, far from the boundary the parameter λ tends to converge to a similar value (the non-Gaussian, weak intermittent high voltage statistics), the gap between the two scales decreasing considerably when V_0 increases. While it is trivial that the small scale values (blue curve) decrease with voltage, due to the disappearing of the coherent structures (Williams convective rolls), the large scale increase of non-Gaussianity with V_0 (red curve) indicates some degree of organization and the appearance of some coherence (self-similar structures) in the liquid crystal [98].

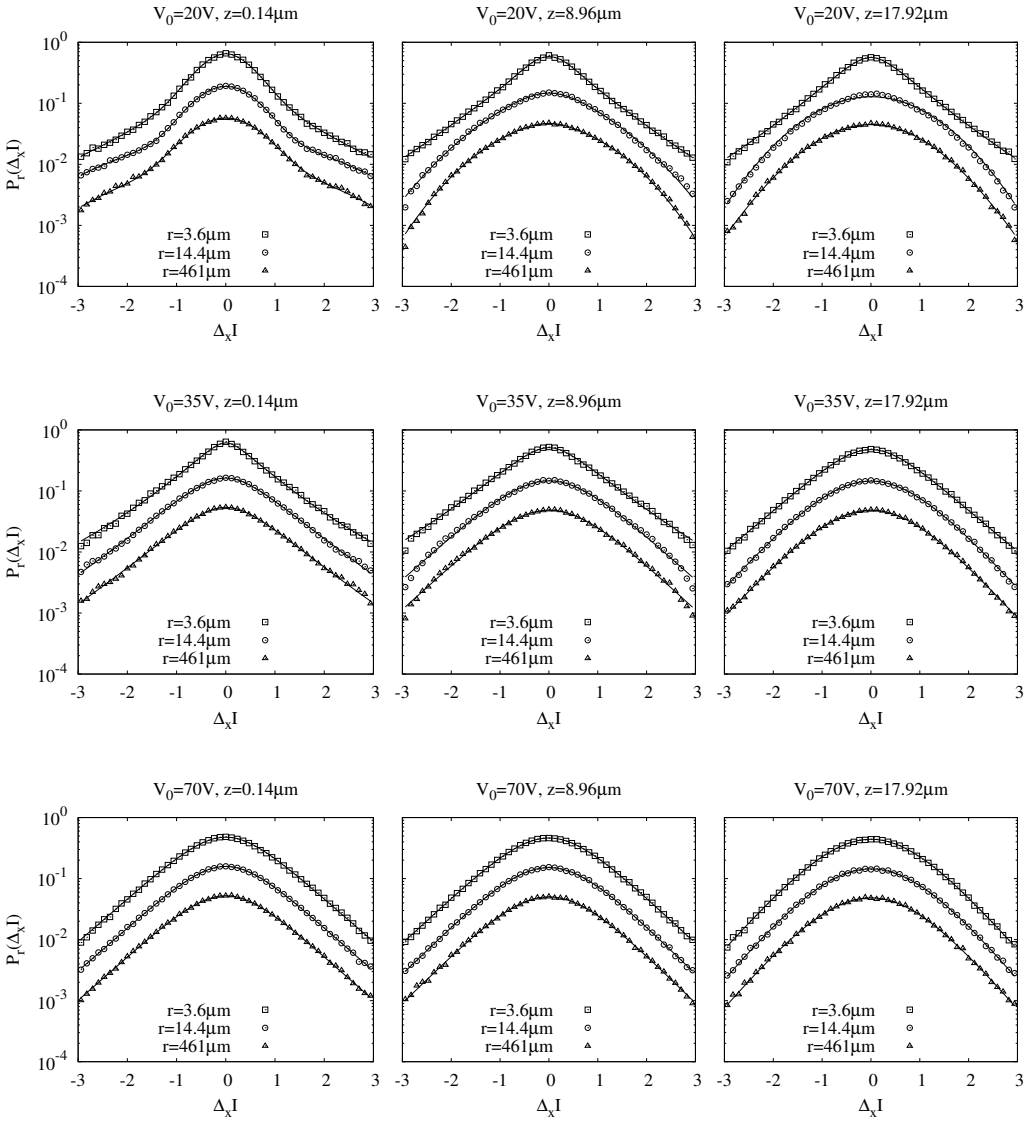

Figure 39: The probability distribution functions of the transverse intensity fluctuations $P_r(\Delta_x I)$, computed at different lags r along the direction x, for three values of the voltage V_0 and at three depths z (symbols, see figure titles and legend). PDFs have been vertically shifted for clarity. The fit with the model PDF is superposed to each distribution, as full line.

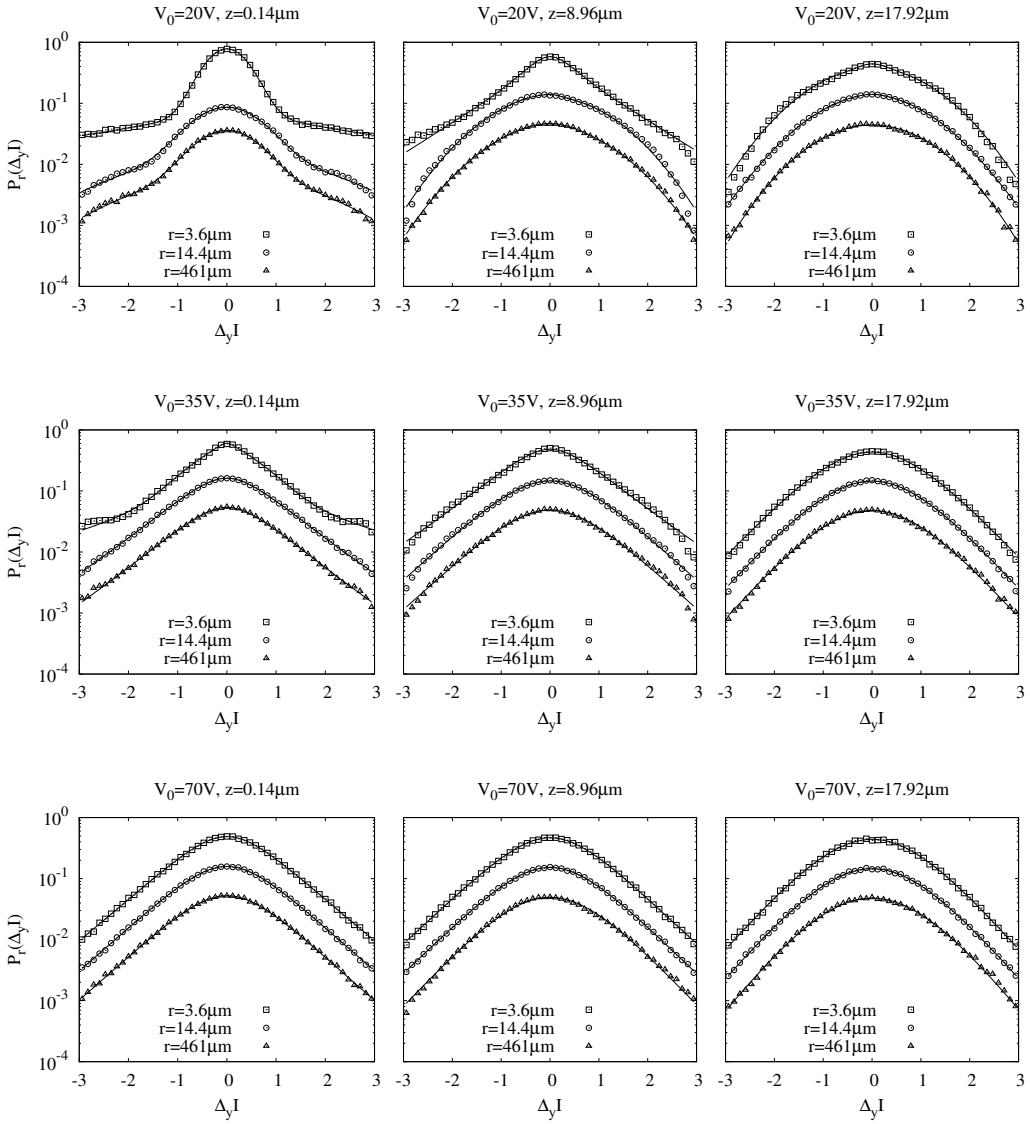

Figure 40: The probability distribution functions of the parallel intensity fluctuations $P_r(\Delta_y I)$ computed at different lags r along the direction y, for three values of the voltage V_0 and at three depths z (symbols, see figure titles and legend). PDFs have been vertically shifted for clarity. The fit with the model PDF is superposed to each distribution, as full line.

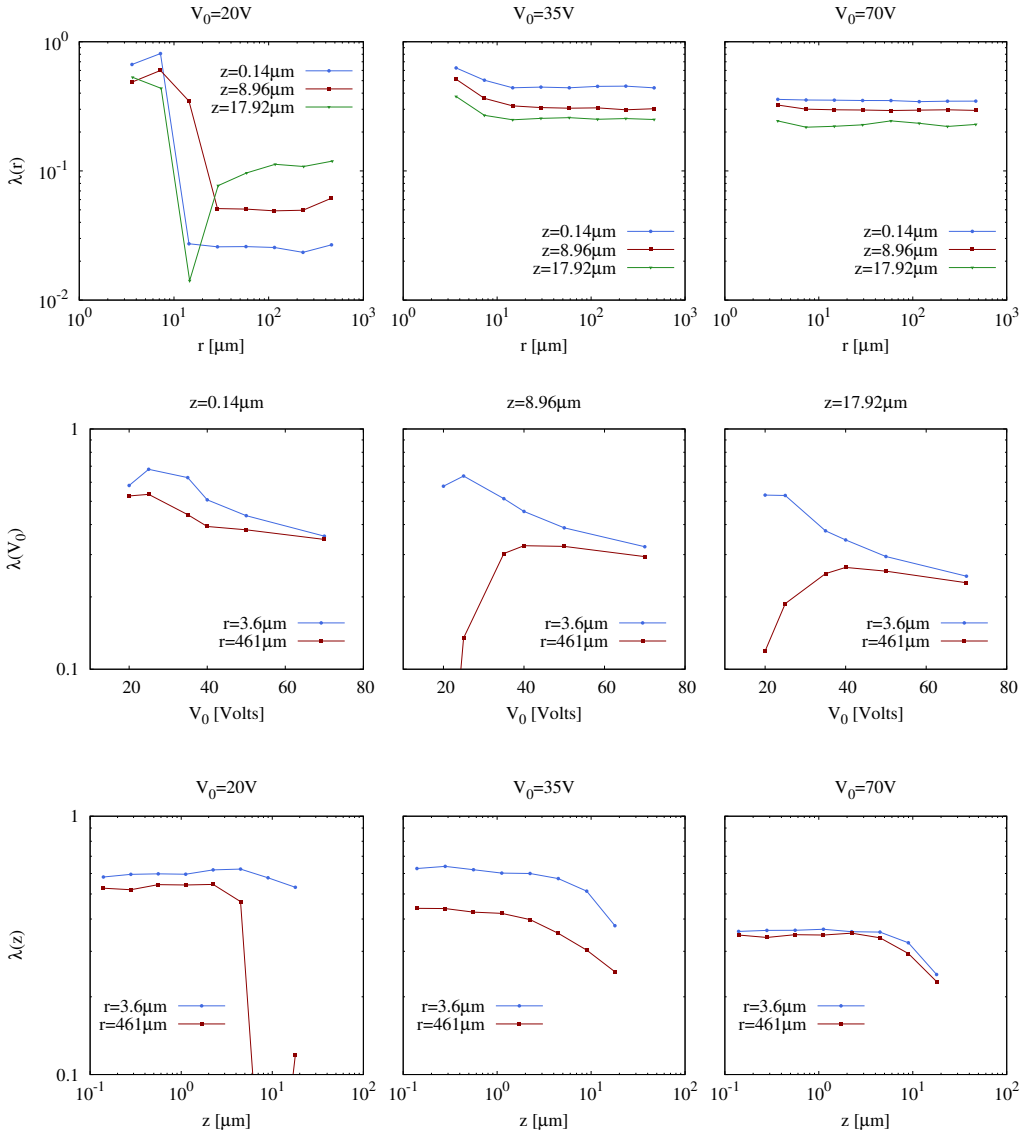

Figure 41: The fit parameter λ as a function of the scale r for the values of voltage V_0 and depth z represented in Figure 39 (see titles and legends), obtained for fluctuations perpendicular to the Williams rolls.

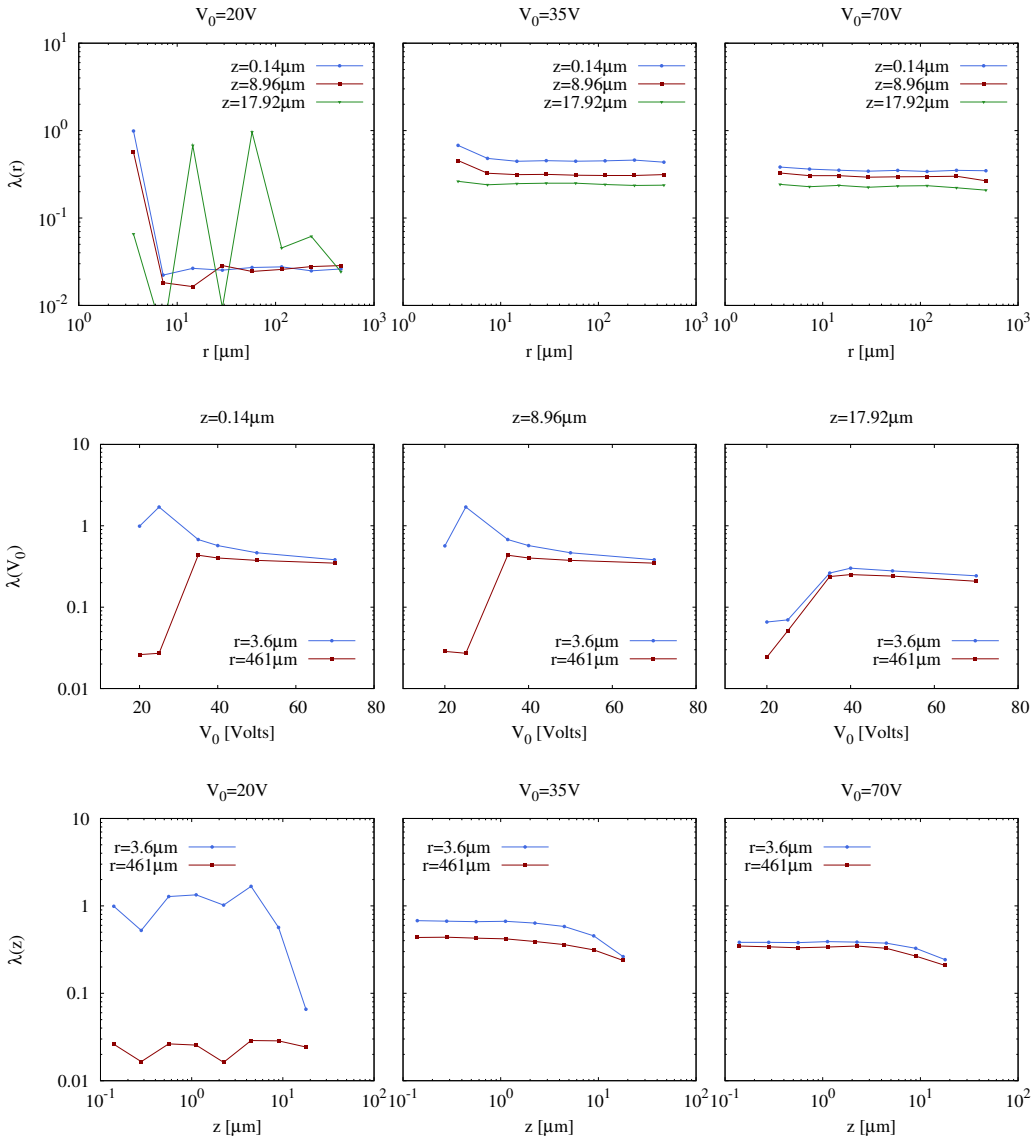

Figure 42: The fit parameter λ as a function of the scale r for the values of voltage V_0 and depth z represented in Figure 40 (see titles and legends), obtained for fluctuations perpendicular to the Williams rolls.

8 THE PROPER ORTHOGONAL DECOMPOSITION

CONTENTS

8.1 Basic Concepts 69
8.2 On Domains and Averaging 72
8.3 Proper Orthogonal Decoposition of EHD Turbulence 72

The proper orthogonal decomposition (POD) provides a basis for the modal decomposition of an ensamble of functions, such as data obtained in the course of experiment. Its properties suggest that it is the preferred basis to use in various applications. The most important of these is *optimality*: it provides the most efficient way of capturing the dominant components of an infinite-dimensional process with only few "modes". The POD was introduces in the context of turbulence by J. L. Lumley [116], and the procedure has been used in various disciplines other than fluid mechanics: random variables [117], image processing [118], signal analysis [119], data compression [120], process identification and control in chemical engineering [121, 122], and oceanography [123]. In all of these application, the POD is used to analyse experimental data with a view to extracting dominant features and trends: *coherent structures*. In the context of turbulence and other complex spatio-temporal fields, these will typically pasterns in space *and* time.

8.1 BASIC CONCEPTS

Supposing the existence of an ensamble $\{u^k\} \in \mathbb{C}$ of scalar fields, each being a function $u = u(x)$ defined on the domain $0 \leqslant x \leqslant 1$. In order to find a good representation for the members of $\{u^k\}$, we need to project each u onto candidate basis functions, and so we assume that u's belong to an inner product space: the linear, infinite-dimensional Hilbert space $L^2([0,1])$, of square integrable (complex-valued) functions with inner product

$$(f,g) = \int_0^1 f(x)g^\star(x)\,dx\,. \tag{8.1}$$

In this context we want to find a basis $\{\phi_j(x)\}_{j=1}^\infty$ for L^2 that is optimal for the data set in the sense that finite-dimensional representation of the form

$$u_N(x) = \sum_{j=1}^{N} a_j\phi_j(x) \tag{8.2}$$

describe typical members of the ensamble better than representation of the same dimension in *any* other basis. The notion of "typical" implies the use of an averaging operation, denote by $\langle\,.\,\rangle$, and which will be assumed to *commute* with the spatial integral (8.1) of the L^2 inner product. The averaging process is discussed in more detail in the next section, but is

sufficient for now imagine an ensamble average over a number of separate experiments forming $\{u^k\}$, or a time average over an ensamble with $u^k = u(x, t_k)$, obtained from successive measurements during a single run.

The mathematical statement of optimality is that we should choose ϕ to maximize the averaged projection of u onto ϕ, suitably normalized:

$$\max_{\phi \in L^2([0,1])} \frac{\langle |(u,\phi)|^2 \rangle}{\|\phi\|} , \tag{8.3}$$

where $|\,.\,|$ denotes the modulus and $\|\,.\,\|$ is the L^2-norm:

$$\|f\| = (f,f)^{\frac{1}{2}} .$$

Solution of (8.3) as states would yield only the best approximation to the ensamble members by a *single* function, but the other critical points of this functional are also physically significant, for they correspond to a set of functions which, taken together, provide the desired basis. The corresponding functional related to the maximization $\langle |(u,\phi)|^2 \rangle$ subject to the constraint $\|\phi\| = 1$ can be expressed as:

$$J[\phi] = \langle |(u,\phi)|^2 \rangle - \lambda(\|\phi\|^2 - 1) \tag{8.4}$$

and a necessary condition for extrema is that the functional derivative vanish for all variations $\phi + \delta\psi \in L^2([0,1])$, $\delta \in \mathbb{R}$:

$$\frac{d}{d\delta} J[\phi + \delta\psi] \,|_{\delta=0} . \tag{8.5}$$

From (8.4) we have

$$\frac{d}{d\delta} J[\phi + \delta\psi] \,|_{\delta=0}$$

$$= \frac{d}{d\delta} [\langle (u, \phi + \delta\psi)(\phi + \delta\psi) \rangle - \lambda(\phi + \delta\psi, \phi + \delta\psi)] \,|_{\delta=0}$$

$$= 2Re[\langle (u,\psi)(\phi,u) \rangle - \lambda(\phi,\psi)] = 0 ,$$

where we use the property $(f,g) = \int f g^\star dx = \left[\int f^\star g \, dx\right]^\star = (g,f)^\star$ of the (complex) L^2 inner product. The quantity in brackets may be written as

$$\left\langle \int_0^1 u(x)\psi^\star(x)\, dx \int_0^1 \phi(x')u^\star(x')\, dx' \right\rangle - \lambda \int_0^1 \phi(x)\psi^\star(x)\, dx$$

$$= \int_0^1 \left[\int_0^1 \langle u(x)u^\star(x') \rangle \phi(x')\, dx' - \lambda\phi(x) \right] \psi^\star(x)\, dx = 0 ,$$

where we have rearranged the integrals and brought the average "inside" using the commutativity of $\langle\,.\,\rangle$ and $\int\,.\,dx$. Finally since $\psi(x)$ is an arbitrary variation, our condition reduces to:

$$\int_0^1 \langle u(x)u^\star(x') \rangle \phi(x')\, dx' = \lambda\phi(x) . \tag{8.6}$$

Thus the optimal basis is given by the eigenfunctions $\{\phi_j\}$ of the integral equation (8.6) whose kernel is the averaged autocorrelation function $\langle u(x)u^\star(x')\rangle = R(x,x')$.

There is also a geometrical interpretation of this representation, particularly in the finite-dimensional case where the observation $\{\mathbf{u}^k\}$ are (m-)vectors rather than functions. In this case The autocorrelation function is replaced by the $m \times m$ tensor product matrix:

$$\mathbf{R} = \langle \mathbf{u} \otimes \mathbf{u}^\star \rangle \ .$$

The eigenvectors of the resulting matrix eigenvalue problem are then simply the principal axes of the cloud of data point $\{\mathbf{u}^k\}$ in the m-dimensional vector space [124]. Hilbert-Schmidt theory assures that there is a countable infinity of eigenvalues and eigenfunctions that provides a diagonal decomposition of the averaged autocorrelation function:

$$R(x,x') = \sum_{j=1}^{\infty} \lambda_j \phi_j(x) \phi_j^\star(x') \ , \tag{8.7}$$

and that the eigenfunctions ϕ_j are mutually orthogonal in L^2. This derivation is stronger than the variational argument given above, since we are assumed a maximum for (8.3) rather than merely a critical point: solution of (8.6) is both necessary *and* sufficient.

We may order the eigenvalues by $\lambda_j \geqslant \lambda_{j+1}$, and observe that the autocorrelation $R(x,x') = \langle u(x)u^\star(x')\rangle$ is non–negative, in order to ensure that $\lambda_j \geqslant 0$ for all j. As we will see in the appendix A, almost every member of the ensamble used in the averaging $\langle \ . \ \rangle$ leading to $R(x,x')$ can be reproduced by a modal decomposition based on the eigenfunctions $\{\phi_j\}_{j=1}^{\infty}$:

$$u(x) = \sum_{j=1}^{\infty} a_j \phi_j(x) \ . \tag{8.8}$$

The POD is literally this equation. The diagonal representation (8.7) of the two point correlation tensor implies that:

$$\langle a_j a_k^\star \rangle = \delta_{jk} \lambda_j \ , \tag{8.9}$$

so that the (random) modal coefficients of the representation are uncorrelated on average. If $u(x)$ is a turbulent velocity field, then the eigenvalues λ_j represent twice the average kinetic energy in each mode ϕ_j, and thus, picking the subspace spanned by the modes $\{\phi_j\}_{j=1}^{N}$ corresponding to the first (largest) N eigenvalues, the representation (8.2) reproduces the most energetic disturbances in the field, as claimed at the outset. The λ_j are called empirical eigenvalues.

Thus far we have considered only function defined on a bounded interval. The unbounded case, which is more natural in the context of open fluid flow, can be dealt with in the same way provided that the inner product (now an infinite integral) is well defined, and that the space of function still has a countable basis. In dealing with unbounded domains in practice we shall either select a finite sub-domain and use periodic boundary conditions (see Appendix A) or we shall be concerned with functions which decay to zero rapidly outside a finite region.

The derivation of the integral equation (8.6) also generalize functions of more than one variable and to vector–valued functions such as the three–dimensional velocity fields $\mathbf{u}(\mathbf{x},t)$ of turbulence, simply by using the appropriate Hilbert space and inner products [124]. For vector–valued functions, $R(x,x')$ is replaced by an averaged autocorrelation tensor $\mathbf{R}(\mathbf{x},\mathbf{x}') = \langle \mathbf{u}(\mathbf{x}) \otimes \mathbf{u}(\mathbf{x}')\rangle$ and the eigenfunctions are also vector–valued. Each mode therefore imposes a fixed relation among the components of the field. The non negative definiteness of $R(x,x')$

implies that the empirical eigenvalues λ_j are non negative themselves, but in general they are not *all* strictly positive. To produce a *complete* basis for L^2 we must include all those "additional" eigenfunction ϕ_j whit zero eigenvalues, although, in view of (8.8), they carry no information on the original data ensamble. It is therefore often advantageous to consider representations in terms of only those empirical eigenfunction with non–zero eigenfunctions with non–zero eigenvalues.

8.2 ON DOMAINS AND AVERAGING

In section 8.1 we focused on fields depending on a single variable x. In dealing with turbulence, the fields depend on four variables, three spatial and one temporal. There is no reason *a priori* to distinguish between space and time and the multi–dimensional theory does not enforce such a distinction: for experiments performed in the one–dimensional spatial domains $0 \leqslant x \leqslant 1$ over times of duration T, one simply measures correlations with time lags as well as spatial separations and works in the space $L^2([0,1] \times [0,T])$, in which case the inner product becomes a double integral over x and t. However, in view of our intent use of POD in the derivation of an empirical eigenfunction basis, we shall generally seek only spatial basis functions. The time-dependent modal coefficients $a_k(t)$ in representations of the form

$$u(x,t) = \sum_k a_k(t)\phi_k(x) \tag{8.10}$$

and their multi–dimensional analogues, will be determined subsequently via projection of the governing equations.

8.3 PROPER ORTHOGONAL DECOPOSITION OF EHD TURBULENCE

When the fields $I(x,y,t)$ are decomposed through (8.10), the number of significant modes strongly depend on V_0. Figure 43 shows the number n of POD modes that contain 99% of the energy, as a function of the applied voltage V_0. In usual fluid turbulence applications, where coherent structures are present at large scales, that amount of energy is spread over only few modes of the order of $n \simeq 3$ [124]. In our experiments the curve $n(V_0)$ increases significantly from a small number of modes, recovered just beyond the stationary WD convective regime, to higher values in the DSM regimes. Large values of n indicate high complexity, the absence of dominating large-scale structures, and the presence of some turbulent dynamics related to non-linear interactions among different structures at all scales. From figure 43, it is perhaps possible to identify three bifurcation points in the instability dynamics, characterizing three different regions of increasing stochasticity.

The time evolution captured by the different coefficients $a_j(t)$, appears very irregular and in general each coefficient is characterized by a power-law spectrum, thus indicating absence of typical structures in time. Chaoticity increases with V_0, as shown in fig.s 44 where we report an example of the time dynamics of the system projected on the two dimensional phase-space made by $a_m(t)$ vs. $a_k(t)$.

The spatial pattern associated to each POD mode, can be characterized by computing the integrated Fourier coefficients $\phi_j(k_x,k_y)$ of the POD eigenfunctions $\psi_j(x,y)$ along the x and y directions, say respectively $\psi_j(k_x) = \int dk_y \phi_j(k_x,k_y)$ and $\psi_j(k_y) = \int dk_x \phi_j(k_x,k_y)$.

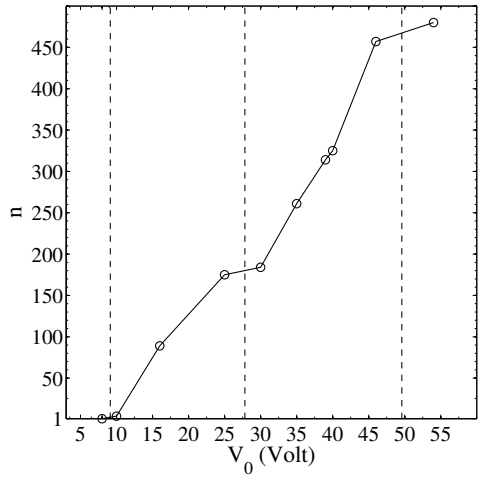

Figure 43: The number of modes n containing 99% of energy as a function of the applied voltage V_0. Three different regimes are roughly identified separated by a weak increase of n.

Further information can be obtained through the integral scale lengths, which represents the energy containing scale of classical turbulence [133]

$$L_{x_i}^{(j)} = \frac{\int_0^\infty |\psi_j(k_{x_i})|^2 k_{x_i}^{-1} dk_{x_i}}{\int_0^\infty |\psi_j(k_{x_i})|^2 dk_{x_i}},$$

where $x_i = x, y$ and k_{x_i} is the wave vector associated to the Fourier coefficients $\psi_j(k_{x_i})$ of each POD mode. This allows to estimate a typical spatial scale for the selected modes, indicative of the size and shape of the characteristic structures isolated by POD. The ratio of the x and y spatial scales can be moreover used for a quantitative evaluation of the structures anisotropy [134]

$$\theta_j(k) = \tan^{-1}\left[\frac{\sum_{\mathbf{k}} k_y^2 |\psi_j(\mathbf{k})|^2}{\sum_{\mathbf{k}} k_x^2 |\psi_j(\mathbf{k})|^2}\right]^{1/2}, \tag{8.11}$$

where $k^2 = k_x^2 + k_y^2$. For an isotropic field $\theta_j(k) = 45°$ for all k. Values of the anisotropy angle $\theta_j(k)$ different from 45° indicate anisotropy at the scale k^{-1}. In particular, $\theta_j(k) > 45°$ indicates presence of structures mainly oriented in the y direction (thus implying periodicity along x), while $\theta_j(k) < 45°$ will be found for structures oriented along the x direction (implying periodicity along y).

The information on the structures generated at higher voltages are summarized in fig.s 45 where we report results relative to three different values of V_0 characterizing different dynamical regimes, namely $V_0 = 25$ V (WT), $V_0 = 40$ V (DSM1), and $V_0 = 54$ V (DSM2). Top panels of figure 45 show the three corresponding snapshots of $I(x, y, t^*)$ at a fixed time $t^* = 10$ s. In the cases under study, modes $j = 0$, representative of the average dynamics, are always characterized by the majority of energy content (90% for WT, 93% for DSM1, 96% for DSM2). The corresponding eigenfunctions $\Psi_0(x, y)$ present an irregular pattern of structures at all scales (not shown). Moreover, they capture experimental bias, common to all the images, such as the inhomogeneity of the microscope light source on the sample, and the acquisition noise. Since POD modes are proper orthogonal basis of the system, the experimental effects are removed from the successive eigenfunctions characterized by

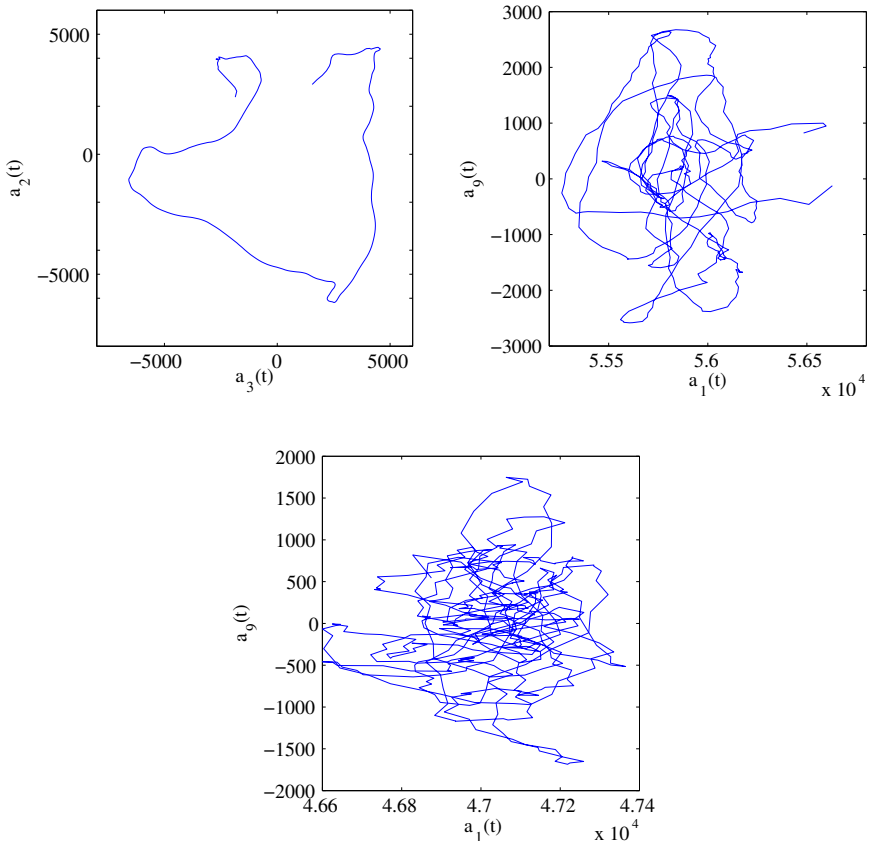

Figure 44: Typcal examples of the time evolution characterizing the three dinamical regimes are shown. Top left panel refers to the WT, top right panel to DSM1 and lower panel to DSM2 regimes respectively. Each panel reports the projection of the time evolution of representative coefficients $a_i(t)$ vs. $a_j(t)$ on a plane.

$j > 0$. The bottom panels of figure 45 show the decreasing energy fraction of each mode, after removing λ_0. After a break (occurring at $j = 6$ for WT, $j = 13$ for both DSM1 and DSM2) the energy fraction decrease exponentially, indicating some change in the properties of structures captured by POD modes.

In the WT regime, the raw snapshots from the dataset (figure 45) are characterized by the presence of complexity, with structures on many spatial scales. As an example, POD modes $j = 2$ and $j = 3$ are shown in figure 45, where a clear presence of structures is observed. According to the usual point of view [63, 64], the convective structures are broken in small domains with different rotation axis. Due to the particular suitability of POD to depict correlation patterns of the dynamics, these small-scale structures are recovered in the modes $j = 2$ and $j = 3$. Although the convective structures observed at smaller V_0 are distorted and broken, the small-scale structures present an alternating pattern of dark-white fringes. The integrated spectra of the POD eigenfunctions are shown in the top-left panel of figure 46. The two spectra for $j = 2$ and $j = 3$ are very similar, so that only the mode $j = 2$ is shown here. The energy roughly decreases as a power law of the wave vector, which is typical of turbulent fields [133]. Along the x direction, a clear peak is visible at $2\pi/k \simeq 28$ µm, which is related to the Williams periodicity. Along the y direction, the low k larger energy content indicates presence of y-elongated structures, whose size is not resolved, as confirmed by looking at

the eigenfunctions in figure 45. The characteristic sizes of the structures, observed clearly in modes $j > 1$, are estimated for the mode $j = 2$ as $L_x \simeq 32$ μm and $L_y \simeq 48$ μm, while for the mode $j = 3$ as $L_x \simeq 33$ μm and $L_y \simeq 42$ μm. The small values found in the x direction (with respect to the sample length) indicates that the residual Williams structures are in fact composed by smaller elements, whose size is comparable with the sample thickness [63]. Presence of anisotropy in the system can be highlighted by means of the anisotropy angle (8.11). As an example, in figure 46 the scale dependency of $\theta(k)$ is shown for the mode $j = 2$. The peak of about $\theta \simeq 64°$ at the scale $2\pi/k \simeq 26$ μm, corresponds to the half periodicity of the peak in the Fourier spectrum of the WD. This represents a further evidence for the presence of structures oriented along the y direction, corresponding to a residual of persistent convective WD structures.

In the DSM1 regime, a turbulent state of the emitted intensity is reached [99, 100]. This regime is characterized by enhanced chaotic behaviour, dominated by a fine grained spatial pattern (see figure 45). In figure 45 the eigenfunctions ψ_1 and ψ_9 are shown as an example. The $j = 1$ mode presents again evident traces of structures elongated in the y directions, with characteristic scales $L_x \simeq 31$ μm and $L_y \simeq 39$ μm, representing the residual of the Williams convective structures. In this case, the structures are more strongly distorted and broken, this being more evident as the mode number increases. The characteristic scales for the mode $j = 9$, which display very similar characteristics, are $L_x \simeq 29$ μm and $L_y \simeq 37$ μm. The spectra of the mode $j = 9$ are shown in figure 46. In the x direction, the peak at $2\pi/k \simeq 28$ μm is still present, while the y direction is again characterized by large scale energy. The corresponding anisotropy angle (figure 46) has a maximum at $2\pi/k \simeq 21$ μm, comparable with (but slightly smaller than) the one obtained in the WT case. Moreover, a broad peak is starting to form at small scales around $2\pi/k \simeq 4$ μm, indicating that the field contains small scale structures elongated in the y direction. Thus, even in this turbulent regime, it is still possible to observe the residual presence of large scale convective structures. Moreover, the fine grained organization of the liquid crystal is put in evidence, showing the small scale anisotropy of the sample.

The DSM2 regime is, even at first glance, globally more isotropic and fine-grained than the previous ones (see figure 45). In the example used here, the modes $j = 1$ and $j = 9$ are shown here as representative examples. The structures observed in the WT and DSM1 regimes are no longer present. The eigenfunctions show a rather homogeneously stochastic behavior, with presence of the same kind of structure on all scales. In fact the typical size of the structures does not change with the order j, being $L_x \simeq 30$ μm, $L_y \simeq 36$ μm for both modes. The spectra, shown here for the mode $j = 1$ in figure 46, do not show the peak previously observed, indicating that the residuals of the Williams structures are eventually lost in the DSM2 regime. Anisotropy is visible for both modes at small scales around $2\pi/k \simeq 4$ μm, confirming the previous observation of small scale structures elongated in the y direction.

To summarize, EHD instabilities in NLC represent one of the out–of–equilibrium system, of which there are no many, where the spatio-temporal dynamics can be investigated in some detail through suitable analysis. In the present paper we investigated the scaling behavior of the chaotic pattern generated by the transmitted light intensity in a MBBA nematic liquid crystal experiencing EHD instabilities when the applied voltage is increased. The number of significant POD modes necessary to reproduce the original dataset is a natural measure to describe the degree of complexity of the system. It was found that complexity increases with the applied voltage, with two clear breaks corresponding to the set-up of a weak turbulence and the saturation of the DSM regime respectively. Interesting subleading pattern formation, have been evidenced in the weak turbulence and DSM1 regimes. Although convective structures observed at smaller V_0 are distorted and broken by the action of the chaotic dynamics, the small-scale structures self-organize through a large-scale pattern still representing a kind of large-scale convective rolls. In the DSM2 regime the above pattern is lost by the strong stochastic dynamics even if sub-leading anisotropic properties, already present in the DSM1

regime, still persist. Namely small scale structures are oriented along the William rolls axis direction y even at the highest voltages.

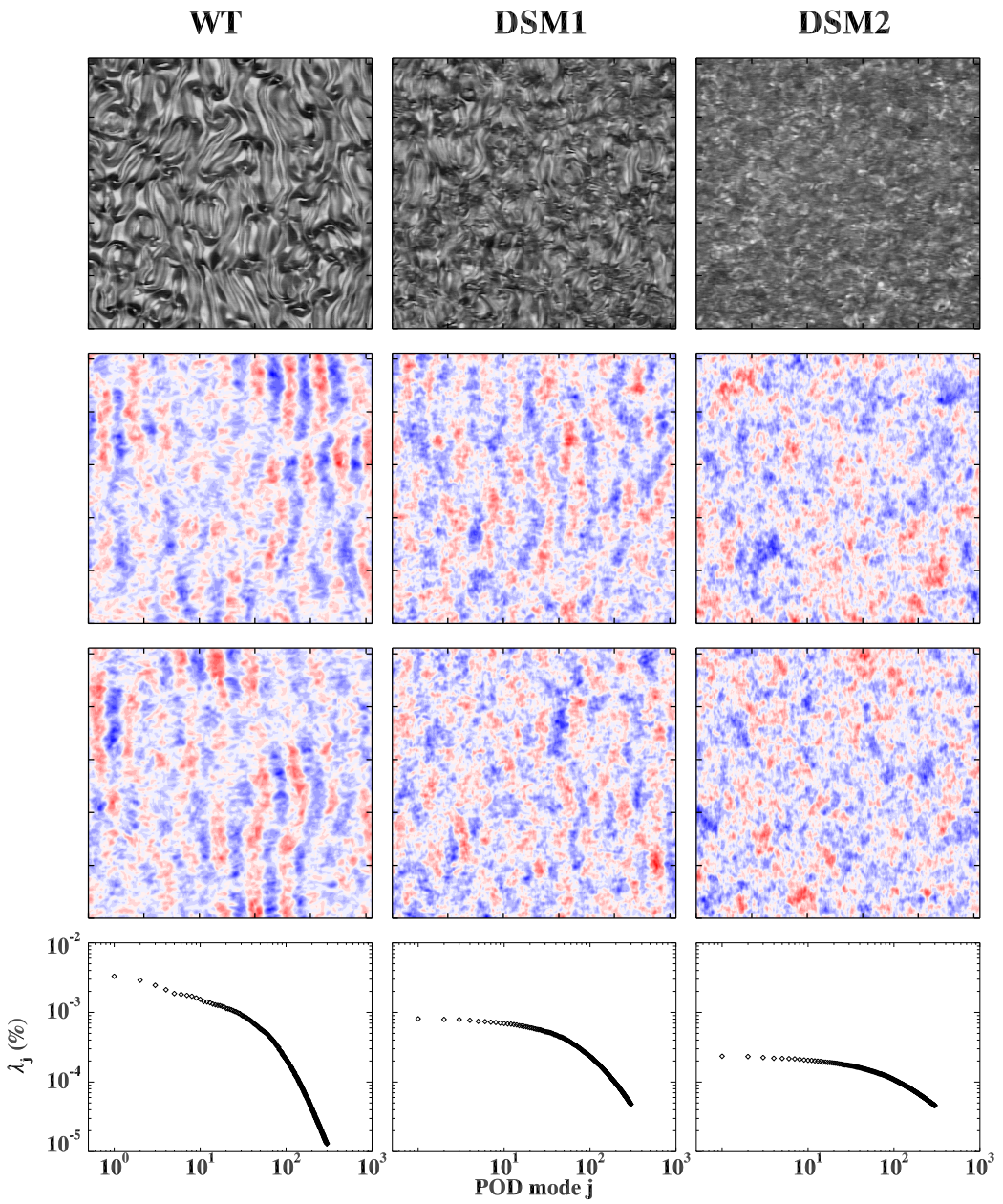

Figure 45: An example of the experimental observation in the three regimes studied $V_0 = 25$ V (WT, left column); $V_0 = 40$ V (DSM1, central column), and $V_0 = 54$ V (DSM2, right column). From top to bottom: a snapshot of the data in the stationary steady state; two POD eigenfunctions of the modes $j = 2, 3$ shown for weak turbulence regime (left column), and modes $j = 1, 9$ shown for both DSM1 (central column) and DSM2 (right column); the eigenvalues λ_j representing the fraction of energy as a function of the mode number j, after removing the mode $j = 0$.

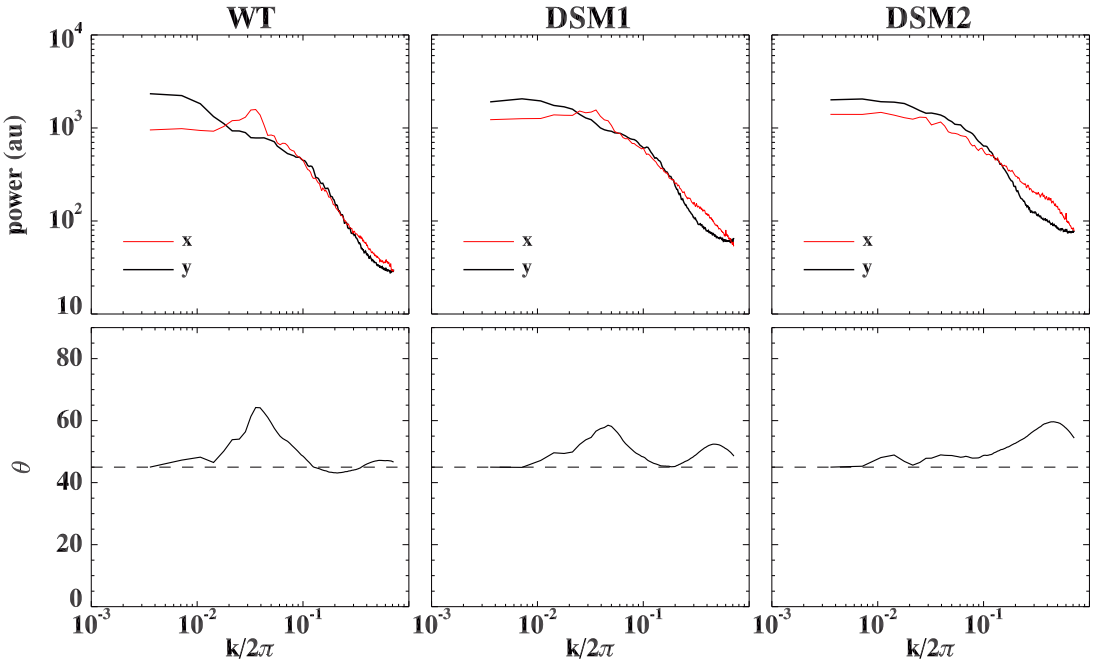

Figure 46: The integrated power spectra, and the corresponding anisotropy angles $\theta(k)$ of the transmitted intensity POD eigenfunctions for three cases studied here. Left panels: weak turbulence regime, mode $j = 2$; central panels: DSM1 regime, mode $j = 9$; right panels: DSM2 regime, mode $j = 1$.

9 DECORRELATION PROCESSES IN EHD TURBULENCE

CONTENTS

9.1 Straining and Sweeping Decorrelation Processes 80
9.2 Experimental Analysis of Decorrelation in EHD Turbulence 81

A major characteristic of turbulence is the rapid destruction of correlations, or coherence, in small scales. Because of their fundamental importance, velocity correlations in space and time have been studied for long time, and along different avenues. One aspect of such investigations, of which there are not many, is the identification of some characteristic scaling time, which would yield a universal form for the various modal time correlations [76]. The same problem has been faced within complex fluids like hydromagnetic fluid flows [142], and in the present Chapter we will investigate the behavior of decorrelation effects in turbulence generated by EHD instabilities [137].

The classical Kolmogorov spectrum of turbulent fluctuations is based on a cascade picture in which the energy transfers between scales much like a series of waterfalls, each one filling a pool that overflows into the next one below [135]. This cascade occurs mainly as a consequence of interactions between eddies of nearly equal size, which means locality in wave-number space, because the size ℓ, namely the usual scale of fluctuations, is related to wavenumber through $k = 2\pi/\ell$. The interactions consist of *straining* motions in which a vortex produces gradients in the velocity that distort other vortices. This is the classical process of decorrelation in turbulence. According to the classical Kolmogorov picture, the decorrelation time in this case corresponds to the eddy-turnover time, that is at a given scale ℓ we have $\tau_{NL} \sim \ell/\delta u_\ell$ (where δu_ℓ represents the characteristic fluctuations across the scale ℓ). By using the Kolmogorov scaling for fluctuations $\delta u_\ell \sim \ell^{1/3}$ we immediately obtain

$$\tau_{NL} \sim k^{-2/3} \tag{9.1}$$

On the other hand, a large-scale flow with velocity u will carry the small-scale vortices but not induces much distortion on their internal dynamics. The direct interactions of the large and small scales consists then of *sweeping* motions which do not involve significant energy transfer in wavenumber space and will not change the form of the energy spectrum. In this case, since te acceleration of fluctuations can be estimated to be $d\delta u/dt \sim (\mathbf{u}\cdot\nabla)\delta u_\ell$, the scaling time for this processes can be estimated to be u/ℓ, and one immediately recovers the scaling of decorrelation time due to sweeping process

$$\tau_{SW} \sim k^{-1} \tag{9.2}$$

The time correlation or equivalently the form of the frequency spectrum (obtained from time series of the velocity at a fixed point) can be stringily influenced by the sweeping effect, since any small-scale fluctuation, which come from the straining motions) will be advected and passed through a probing point, thus introducing strong fluctuations in the time series.

In complex fluids like hydromagnetic turbulence, the influence of wave propagation can be regarded as a sweeping effect [142]. In this case, as noted by Kraichnan [136], waves can both destroy correlations *and* affect the energy transfer, because the time required to effectively realize the cascade is lowered, due to stochastic encounters between fluctuations which are sweeped away. This gives rise to a power spectrum different from the universal $-5/3$ Kolmogorov spectrum. Even for fluctuations generated by Electrohydrodynamic instabilities, we expect that two main processes could takes place in the decorrelation process. The first one is the fragmentation process from which small-scale structures are continuously generated [63], a process which results to be similar to the straining of the usual energy cascade. The second process results in the random motion of both the walls between two Williams domain and the large-scale disclination lines, which move more randomly and even faster as the external voltage increases. This may be viewed as a generalization of nonlocal sweeping effect. Due to these processes, we expect that the sweeping effect will be more important at higher voltages during electroconvective turbulence. Moreover, at variance to hydrodynamic where a large-scale velocity flow can be eliminated through a galilean transformation, large-scale disturbances in EHD turbulence cannot be eliminated, and this introduces a large-scale anisotropy which will make more complex the decorrelation process of fluctuations.

9.1 STRAINING AND SWEEPING DECORRELATION PROCESSES

Given a turbulent field $I(\mathbf{x}, t)$, evolving both in space and time space-time, the information about its decorrelation properties is contained in the two-points, two-times autocorrelation function

$$R(\mathbf{r}, \tau) = \langle I(\mathbf{x}, t) I(\mathbf{x} + \mathbf{r}, t + \tau) \rangle, \tag{9.3}$$

computed at spatial and temporal lags $\mathbf{r}$ and τ respectively (brackets indicating both spatial and temporal average). In the wave vector space, the autocorrelation function can be written as

$$R(\mathbf{k}, \tau) = \langle I(\mathbf{k}, t)^2 \rangle \Gamma(\mathbf{k}, \tau) \tag{9.4}$$

where $\mathbf{k}$ is the wave vector associated to the lag $\mathbf{r}$. The function Γ represents the dynamical decorrelation processes, by describing the time decay of information for each scale k^{-1}, as can be shown in the framework of closure models for isotropic turbulence [76, 77].

As we said before, in the Kolmogorov phenomenological theory of K41 isotropic fully developed turbulence [141], the basic physical process generating the hierarchy of fluctuations at all scales is the nonlinear straining, responsible for the energy transfer toward smaller and smaller scales (the nonlinear energy cascade). The field correlation decay is then attributed to nonlinear interaction among triads of wave vectors [76, 77]. Within this picture, the function Γ has the similarity form

$$\Gamma_{nl}(\mathbf{k}, \tau) = \Gamma_{nl}[\gamma_{nl}(\mathbf{k})\tau] \tag{9.5}$$

where $\gamma_{nl}(\mathbf{k})$ is the scale dependent decorrelation rate of the field, resulting in the exponential decay of the strain dominated decorrelation

$$\Gamma_{nl} \sim \exp(-\gamma_{nl}\tau) \tag{9.6}$$

The Kolmogorov scaling yields a phenomenological relation $\gamma_{nl} \sim k^{2/3}$ for the decorrelation rate (9.1), as observed in numerical results [139]. However, to our knowledge such scaling has not been clearly observed in experimental data so far.

An alternative physical decorrelation mechanism in turbulent flows is the so called random sweeping. A large scale velocity field $\mathbf{u}$ is assumed to advectively transport fluctuations, so that field fluctuations at scale k decorrelate the field at frequency $\omega_0 = ku$ [76, 77, 138]. Therefore, for random sweeping dominated decorrelation, the dynamical function Γ depends on the velocity probability distribution $P(u/u_0)$, so that [142]

$$\Gamma_{sw} = \int d\omega e^{i\omega\tau} \int d(u/u_0) P(u/u_0) \delta(\omega - \omega_0) \tag{9.7}$$

where u is the velocity component along the lag $\mathbf{r}$ and u_0 is its characteristic *rms* value. At large scales, the sweeping velocity can be reasonably assumed to be a Gaussian random variable

$$P(u/u_0) = \frac{1}{\sqrt{2\pi}} \exp(-u^2/2u_0^2) \tag{9.8}$$

By integrating eq. (9.7), it follows that the decorrelation function results

$$\Gamma_{sw} = \exp\left[-\frac{(u_0\tau k)^2}{2}\right] \tag{9.9}$$

In terms of the decorrelation rate (9.2), this result reads $\gamma_{sw} \sim k$. This scaling has been observed in experimental and numerical flows [139, 140], and is believed to be the mechanism controlling decorrelation in fluid turbulence.

9.2 EXPERIMENTAL ANALYSIS OF DECORRELATION IN EHD TURBULENCE

The chaotic dynamics of the system has been studied in the past, suggesting some similarities with the turbulent motion of fluids. Indeed, the scaling behaviour of EHD turbulence has been attributed to a stochastic fragmentation process [63, 143], similar to the generation of small scale structures within fluid turbulence. Therefore, a nonlinear straining phenomenology can be expected to describe the decay of correlation in EHD. On the other hand, a sweeping effect could also be present in EHD, due to the persistent random motion of large scale structures, recently observed up to high voltages as sub-leading contribution [143].

A remarkable difference with respect to fluid dynamics is the intrinsic anisotropy of EHD turbulence. This arises both because NLCs are anisotropic fluids, and because of the large scale oriented Williams structure (persistence of anisotropy has been recently reported for larger voltages [143]). It is thus necessary to study the field properties separately in two directions, parallel $r_{\parallel}$ and perpendicular $r_{\perp}$ to the Williams domain orientation. Correspondingly, $\mathbf{k} = (k_{\parallel}, k_{\perp})$. In strongly anisotropic flows (as for example in magnetohydrodynamics with large scale mean magnetic field [142]), turbulence is usually confined to planes perpendicular to the anisotropy axis. In these conditions, the Kolmogorov decorrelation effect is expected to act perpendicularly with respect to the anisotropy direction, leading to $\gamma_{nl} \sim k_{\perp}^{2/3}$ [142].

In order to explore the decorrelation properties of EHD, two-dimensional images of a sample cell of MBBA [N-(4-Methoxybenzyliden)-4-butylanilin] NLC film have been acquired

by an optical microscope. The sample, $d = 50\mu m$ thick, is planarly aligned, its elongated molecules lying in the plane $\mathbf{x} = (x, y)$. The NLC is stimulated by an oscillating electric field $\mathbf{E} = (V_0/d)\,\hat{\mathbf{z}}$, at frequency $f_0 = 70Hz$, and at different values of $V_0 \in [15, 50]V$. In this experiment the threshold for the activation of Williams domains (with axis in the x direction) is $V_{th} = 7.5V$. The regimes of instability under different experimental conditions (e.g. for different aspect ratio of the cell) can be compared by normalizing the voltage to the threshold value, so that in the following we will use $\epsilon = V_0/V_{th}$. The sample is illuminated by a white light beam polarized along y, and the instantaneous transmitted light intensity $I(\mathbf{x}, t)$ is measured. The data set consists of eight space-time series taken at different V_0, each one about 9 sec long, of $L_x = 461\mu m$ and $L_y = 432\mu m$ snapshots. The (square) pixel size is $\Delta r = 0.9\mu m$, while the images sampling time is $\Delta t = 1/120$ sec. Each time series describes the space-time variation of the refractive index, which is in turn related to the average local distortion of the molecular director field. Figure 47 shows snapshots of the intensity field at four values of the applied voltage V_0, evidencing the increasing degree of complexity of the spatial patterns. It should be noticed that direct measurement of the NLC velocity field is a complicated issue, so that the field is not available for our database.

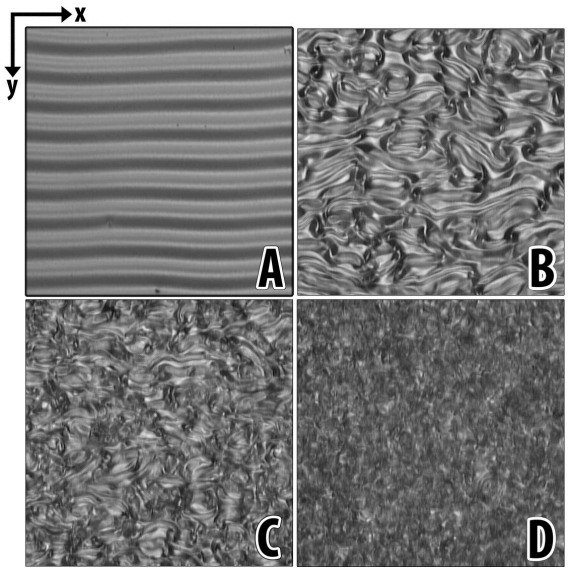

Figure 47: Four snapshots of the intensity field $I(\mathbf{x}, t^*)$ of EHD turbulence taken at a fixed time $t^* = 1$ sec, for different voltages: A) $\epsilon = 1$, B) $\epsilon = 4.67$, C) $\epsilon = 6$, D) $\epsilon = 6.67$.

In order to describe the decorrelation properties of the system, we have calculated from each dataset the two-point, two-times correlation function $R(\mathbf{r}, \tau)$. In the wave vector space, we obtained $\Gamma(\mathbf{k}, \tau)$ for different wave vectors $\mathbf{k}$ and different values of V_0. These are shown in Figure 48 as a function of the time lag τ, for two voltages ($\epsilon = 3.33, 6.67$) and five wave vectors $k_{||} = n(2\pi/L_x)$, in the range $1 \leqslant n \leqslant 50$. From the decay of Γ, it is evident that at large scale (small wave vectors) the field is coherent for long times, while at small scales (large wave vectors) decorrelation is faster. Similar results were found in the perpendicular direction $k_\perp = n(2\pi/L_y)$ (not shown). To explore the occurrence of decorrelation processes in EHD, it is interesting to study the explicit dependence of the decorrelation rate γ on the wave vector $\mathbf{k}$. To this aim, decorrelation rates have been estimated from data as [76]

$$\frac{1}{\gamma(k_\alpha)} = \int_0^\infty \Gamma(k_\alpha, \tau)\, d\tau \tag{9.10}$$

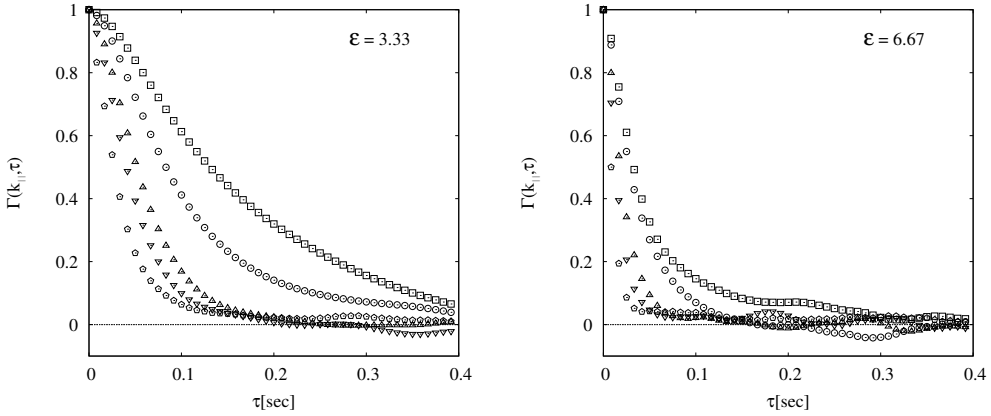

Figure 48: The function $\Gamma(k_{||}, \tau)$ for two different values of ϵ. Symbols refer to different wave vectors $k_{||} = (2\pi/L_x)n$, namely: $n = 1$ (squares), $n = 10$ (circles), $n = 20$ (up triangles), $n = 30$ (down triangles), $n = 50$ (diamonds).

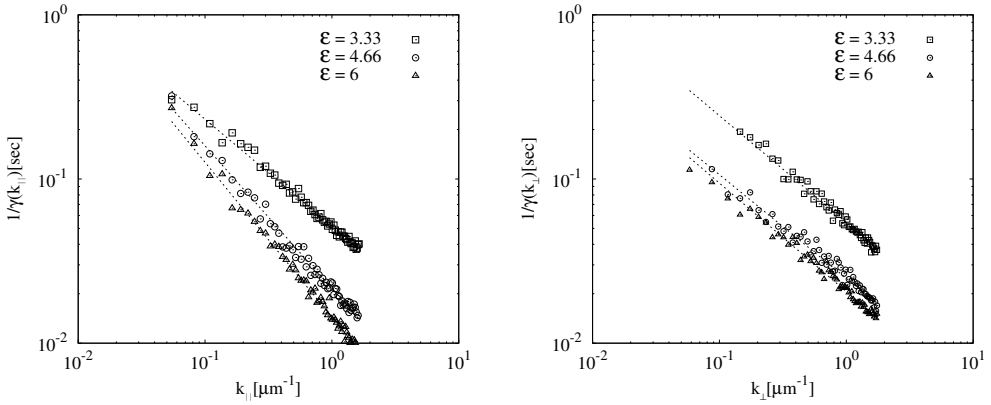

Figure 49: Scaling behavior of the decorrelation rates $1/\gamma(k_{||})$ (top panel) and $1/\gamma(k_{\perp})$ (bottom panel), for three different voltages ϵ. Dashed lines represent power-law fits.

and have been fitted with the generic power-law

$$\frac{1}{\gamma(k_\alpha)} \sim k_\alpha^{-\mu} \tag{9.11}$$

where α indicates the parallel or perpendicular component. In Figure 49 we show the scaling behavior of both $\gamma(k_{||})$ and $\gamma(k_{\perp})$, for three different values of V_0. A power-law scaling range is found up to wave vectors of the order of $k \simeq 5\mu m^{-1}$. The scaling exponents μ, computed from the fit of the decorrelation rates, are plotted in Figure 50, as a function of ϵ. Our results indicate that in the perpendicular direction the measured scaling exponent is compatible with the Kolmogorov value $\mu = 2/3$ at any voltage. This represents experimental evidence of Kolmogorov scaling, suggesting that decorrelation is dominated by a fragmentation mechanism, similar to that generating the nonlinear energy cascade in turbulence [143]. On the other hand, the scaling exponent for parallel decorrelation increases from the Kolmogorov value observed at low voltage ($\epsilon < 3.5$), to intermediate values ($3.5 < \epsilon < 5.5$), up

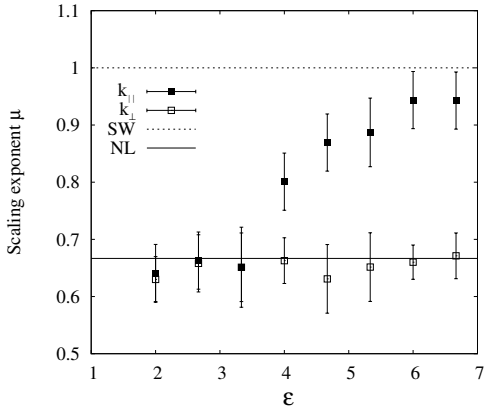

Figure 50: The scaling exponents μ versus the voltage ϵ. Symbols refer to $k_{\parallel}$ (black squares) and $k_{\perp}$ (white square). Full line represents the model value $\mu = 2/3$, predicted for straining decorrelation (NL), while the dashed line represents the model value $\mu = 1$, typical of sweeping decorrelation process (SW).

to values compatible with the Kraichnan exponent $\mu \simeq 1$ for $\epsilon > 5.5$. This suggests that high voltage parallel decorrelation results from a process similar to random sweeping.

It is remarkable that a smooth transition between the two theoretical values is observed in the parallel direction. If we suppose that both random sweeping and nonlinear straining are, in different measure, responsible for the decorrelation in the system, it is possible to introduce a decorrelation function including both effects as

$$\Gamma(k_{\parallel}, \tau) = e^{-(u_0 \tau k_{\parallel})^2/2} e^{-k_{\parallel}^{2/3}\tau} . \tag{9.12}$$

The large scale *rms* velocity u_0 represents the level of fluctuations in the EHD convective process, therefore determining the intensity of the sweeping effect. Since velocity measurements are not available for the sample under study, the fit of the experimental curves with relation (9.12) provides an estimate of the characteristic u_0 as a function of ϵ. Results of the fit are shown in Figure 51. The characteristic velocity responsible for the sweeping increases linearly with the voltage. A change of slope is however observed around $\epsilon \simeq 3.5$, separating the low voltage regimes, where decorrelation is described by $\mu \simeq 2/3$, from the zone where the sweeping contribution is assumed to increase. The kink indicates a change of regime, due to increasing amplitude of the velocity fluctuations activating the sweeping effect, in agreement with the behavior of μ presented in Figure 50. Direct measurements of velocity in an independent similar system have been reported in the past [144, 145]. The same double linear increase of velocity was observed (but not explained), with a kink located at $\epsilon \simeq 4$ [144], in good agreement with our results. This confirms that the values of u_0 obtained here are a reliable proxy for the typical velocity fluctuations of the convective flow, and support out model for the sweeping. With our result, we conjecture that the change of slope of velocity observed in EHD is associated with the threshold set-up of the sweeping effect within a process of transition to turbulence.

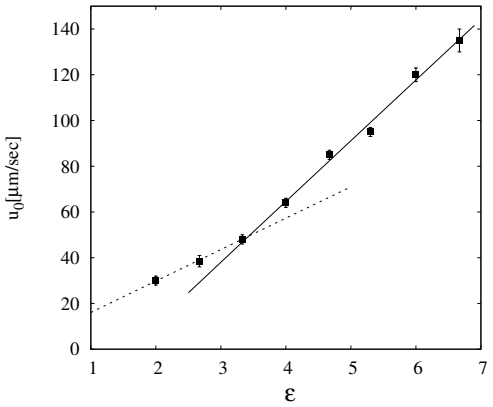

Figure 51: Large scale characteristic velocity u_0 as a function of the normalized voltages ϵ. The straight lines indicate linear fit. The kink location is evaluated at the intersection of the fitting straight lines, for $\epsilon \simeq 3.5$.

10 DYNAMICAL LOCALIZATION OF LIGHT IN NLC

CONTENTS

10.1 Coherent Backscattering and Weak Localization of Light 87
10.2 A Simple Model for the CBS Description 88
10.3 The Cone Shape 90
10.4 Weak Localization in EHD Turbulence 91
10.4.1 CBS Experiments in EHD 92

Light scattering experiments have a long and time honored history in physics. Early experimental investigations into the nature and behavior of light were conducted by Newton, Huygens, Young, Fresnel, and Rayleigh to name a few. Our understanding has progressed from a belief in ether borne vibrations to a self-consistent electromagnetic theory that incorporates all known light scattering phenomena. Light scattering experiments have enjoyed a renaissance since the invention of the laser and have gained further prominence as potential applications of quantum optics, nonlinear optical materials, and photon localization are conceived. It is the possibility of achieving photon localization [1] that has spurred interest in coherent backscattering of light (CBS) as a current research topic.

10.1 COHERENT BACKSCATTERING AND WEAK LOCALIZATION OF LIGHT

CBS is a photon self-interference effect which leads to an enhanced intensity cone in the backscattering direction. A schematic representation of the now classic CBS experiment is illustrated in Fig. 1. Laser light is incident on a dense colloidal suspension containing polystyrene spheres [146], in water, undergoing Brownian motion. The diffuse intensity profile is recorded as a function of backscattering angle leading to the appearance of the CBS intensity cone, whose height is predicted to be twice the incoherent background level. This effective increase in reflectivity reduces the optical energy transported in the forward direction and provides the link with photon localization. This retro reflection enhancement was first observed by A. Ishimaru and Y. Kuga [147] but it was not until the observations of M. van Albada and A. Lagendijk [148] and G. Maret and P. Wolf [149] that its connection with phase coherent time-reversed paths and photon localization was made clear. This connection is sometimes made explicit by referring to CBS as weak photon localization.

Fundamentally, the enhancement is due to the fact that, because of time-reversal symmetry, every path through a random medium has a counterpropagating partner. Light elastically scattered on these two paths interferes constructively, because the path-lengths are necessarily the same. This leads to an enhancement of exactly a factor of *two* in the direction directly opposite to the incidence. CBS is not an interference due to the properties of a single scatterer, but relies fundamentally on multiple scattering. In fact, in the single-scattering regime there cannot be a CBS cone as there cannot be a counterpropagating light path. The "entry" and "exit" points of a multiple-scattering path can then be seen as the two points of a double slit,

which, due to the coherence of the time-reversed paths, necessarily interfere with each other. The different interference patterns corresponding to different light paths in the disordered medium have to be averaged over, which will lead to the shape of the backscattering cone, the averaging will always lead to an enhancement factor of two.

These principles behind the origin of the backscattering cone will strongly influence the transport through a random system. Taking the end points of the counterpropagating paths to coincide somewhere inside the sample, there will be a two-fold enhancement at this point on such a closed loop. This in turn leads to a decreased probability of transport through the system. This effect is what causes *Anderson localization*, *i.e.* the loss of diffuse transport due to increasing disorder. As disorder increases, the probability of forming closed loops on which intensity is enhanced increases. At a certain critical amount of disorder, these closed loops start to be macroscopically populated, which leads to a loss of diffuse transport. This critical amount of disorder has been estimated using dimensional arguments by Ioffe and Regel (1960) to be when the mean free path roughly equals the inverse wavenumber, *i.e.* when $k\ell^\star \sim 1$ ($\ell^\star$ is the transport mean free path). Such a mechanism was first proposed for the transport of 43 electrons in metals, where it was found that an increase in disorder can turn a metal into an insulator.

Historically, the first instances of localization were discussed in the context of electron transport in metals, and thus localization was thought to be a quantum effect. Moreover, due to the fact that localization should always be present in two dimensions and is not influenced too much by the presence of correlations, these studies were carried out in thin films. Eventually however, it was realized that the quantum nature of electrons is not a necessary ingredient for the occurrence of Anderson localization as, in fact, this is purely a wave effect. Thus, it should also be possible to observe localization effects with classical waves, such as light, as was proposed by John (1984) and Anderson (1985). CBS, that is, weak localization, was observed with light shortly thereafter; subsequently, there was a vigorous programme to also observe signs of strong localization of light, because the study of photon transport in disordered media has many advantages over the study of electrons in metals. This is because in the latter case there are alternatives that may also lead to localization: in the case of electrons, a random potential can lead to a trapping of particles, which also strongly affects transport, while not being connected to localization. On the other hand, electrons also interact with each other via Coulomb interaction, so that correlations in electron transport are again not necessarily due to localization effects, but may more likely be explained by electron-electron interactions. In fact, it can be shown that in the presence of particle interactions, the effects of localization vanish. However, as we will discuss below, the photonic system is not completely free either of possible artifacts masking as localization. For instance, light will be absorbed by materials to a certain extent, which leads to a loss of energy transport similar to localization. Furthermore, resonant scattering can lead to a time delay in the scattering process, 34 which leads to a slowing down of transport, which again may be mistaken for localization.

10.2 A SIMPLE MODEL FOR THE CBS DESCRIPTION

The simplest model describing the CBS process is that the photons are undergoing a diffusion-like random-walk with an average step size given by the transport mean free path length $\ell^\star$. However, since light in this experiment behaves as an electromagnetic wave, and not a classical particle, interference between scattering paths must be considered. It is just this interference between time-reversed (momentum-reversed) paths that gives rise to the CBS intensity cone. Figure 2 shows a prototypical scattering path and its time-reversed mate and also illustrates the existence of a path length difference (PLD) between the two.

The nature of the time-reversed scattering path interference depends on the phase difference between the two scattered waves. This phase difference is given as

$$\Delta\phi = \frac{2\pi}{\lambda}\mathrm{PLD} = \frac{2\pi}{\lambda}(d_2 - d_1), \tag{10.1}$$

where λ is the wavelength of the incident radiation in water, PLD is again the path length difference, the distance d_1 is the projection of the vector that points from $\mathbf{r}_1$ to $\mathbf{r}_n$, on $-\hat{\mathbf{k}}_\mathbf{i}$, and the distance d_2 is the projection of vector $(\mathbf{r}_n - \mathbf{r}_1)$ on $\hat{\mathbf{k}}_\mathbf{f}$. The distances d_1 an d_2 are thus given by

$$\begin{aligned} d_1 &= -\hat{\mathbf{k}}_\mathbf{i} \cdot (\mathbf{r}_n - \mathbf{r}_1) \\ d_2 &= \hat{\mathbf{k}}_\mathbf{f} \cdot (\mathbf{r}_n - \mathbf{r}_1), \end{aligned} \tag{10.2}$$

which yields a phase difference of

$$\Delta\phi = \frac{2\pi}{\lambda}(\hat{\mathbf{k}}_\mathbf{f} + \hat{\mathbf{k}}_\mathbf{i}) \cdot (\mathbf{r}_n - \mathbf{r}_1). \tag{10.3}$$

It is evident from this expression that for light scattered directly into the backward direction, $\hat{\mathbf{k}}_\mathbf{f} = -\hat{\mathbf{k}}_\mathbf{i}$, the phase difference between a scattering path and its time-reversed mate is zero, and thus, completely constructive interference results. The qualitative nature of the interference away from the exact backscattering direction can be ascertained by making use of our diffusive model of photon transport within the colloidal suspension. The phase difference becomes, by evaluating the dot product in Eq. (10.3),

$$\Delta\phi = \frac{2\pi}{\lambda} 2 \sin\left(\frac{\theta}{2}\right) R \cos\alpha, \tag{10.4}$$

where θ is the scattering angle measured from the backscattering direction, $R = |\mathbf{r}_n - \mathbf{r}_1|$, α is the angle between $(\hat{\mathbf{k}}_\mathbf{f} + \hat{\mathbf{k}}_\mathbf{i})$ and $(\mathbf{r}_n - \mathbf{r}_1)$, and $|\hat{\mathbf{k}}_\mathbf{f} + \hat{\mathbf{k}}_\mathbf{i}| = 2\sin\left(\frac{\theta}{2}\right)$. Restricting our analysis to the experimentally realized situation of small θ (~milliradians) we obtain

$$\Delta\phi \approx \frac{2\pi}{\lambda}\theta R, \tag{10.5}$$

where we have also used the fact that for a dense suspension $(\mathbf{r}_n - \mathbf{r}_1)$ will be nearly parallel to the sample surface and $(\hat{\mathbf{k}}_\mathbf{f} + \hat{\mathbf{k}}_\mathbf{i})$, yielding $\cos\alpha \approx 1$. The mean square separation between the first and last scatterer in the photon diffusion approximation is given as

$$\langle R^2 \rangle = 6Dt = 6\left(\frac{c\ell^\star}{3}\right) t, \tag{10.6}$$

where D is the photon diffusion coefficient, t is the random-walk time, and c is the speed of light [6]. Using the root-mean-square value for R we obtain the final expression for the phase difference

$$\Delta\phi \approx \frac{2\pi}{\lambda}\theta \sqrt{6\left(\frac{c\ell^\star}{3}\right) t} = \frac{2\pi}{\lambda}\theta\sqrt{2\ell^\star ct} \tag{10.7}$$

where ct represent the total scattering length.

In order for the two partial waves which traverse time-reversed paths to add constructively, their phase difference must be small. This coherence condition may be stated as $\Delta\phi/2\pi << 1$. Thus, there will exist a critical angle θ_c below which this condition will be satisfied and phase coherence maintained. This critical angle is defined as:

$$\theta_c \approx \frac{\lambda}{\sqrt{2\ell^\star ct}}. \tag{10.8}$$

This result has important implications for the shape of the CBS cone and accounts for the cone enhancement factor, the ratio of maximum cone height to background level, of two. As mentioned above, Eq. (10.3) implies that the two partial waves must be added coherently (sum then square) to obtain their contribution to the intensity in the exact backscattering direction, whereas the incoherent sum (square then add) may be used for angles greater than θ_c, leading to the enhancement factor of two. One implication for the cone shape is that paths for which the total path length is large will only contribute coherently within a relatively small angle about the backscattering direction. That is, the critical angle decreases as the total photon path length increases. This implies that any physical phenomenon that affects the long scattering paths, or distribution of path lengths, will manifest itself near the backscattering direction. Some of these phenomena include absorption [150], finite sample size [151], and sample surface reflectivity [152].

Another important result that is easily obtained from Eq. (10.8) is the dependence of the coherent cone width on the transport mean-free-path length. The maximum angular cone width is the critical coherence angle obtained for the smallest total path length. The smallest average path length is $ct = \ell^\star$, yielding a cone width of

$$\theta_{max} \approx \frac{\lambda}{\sqrt{2}\ell^\star}, \tag{10.9}$$

which scales inversely with $\ell^\star$.

10.3 THE CONE SHAPE

Given the nature of the backscattering cone due to interference of photons on time-reversed paths, one can explicitly calculate the shape of the enhancement as a function of angle. In order to do this, the interference patterns, corresponding to two counter-propagating paths with end-to-end distance ρ, need to be averaged weighted by the probability distribution of such an end-to-end distance occurring. Like in a double-slit experiment with slit separation ρ, each of these interference patterns will contribute a factor $1 + \cos(q\rho)$, such that the enhancement above the incoherent background is simply given by the real part of the Fourier transform of the end-to-end distance distribution:

$$\alpha(q) = \int p(q) \cos(q\rho) d\rho. \tag{10.10}$$

In the diffusion approximation, this probability distribution can be calculated to be $1/a(1 - \rho/\sqrt{\rho^2 + a^2})$ in the case of a semi-infinite planar half-space. Here the length scale $a = 4\gamma\ell^\star$ describes how the diffuse intensity penetrates the sample as described by the Milne parameter γ and the transport mean free path $\ell^\star$. The parameter γ can be calculated from the radiative transfer equation to be of the order of ~ 0.71 and in the diffusion approximation is exactly $\gamma = 2/3$. In the following, we will always use the value of $\gamma = 2/3$. This leads to the following expression for the backscattering enhancement:

$$\alpha(q) = \int \left(1 - \frac{\rho}{\sqrt{(\rho^2 + a^2)}}\right) \cos(q\rho) d\rho. \tag{10.11}$$

By integrating Eq. (10.11) we obtain

$$\alpha(q) = \frac{3/7}{(1 + q\ell^\star)^2} \left(1 + \frac{1 - e^{-4/3q\ell^\star}}{q\ell^\star}\right). \tag{10.12}$$

This gives a cone shape in very good agreement with the experiments that will be discussed in next sections. As can be seen from an investigation of the angle dependence, the cone tip is triangular with an enhancement of 1 in the exact backscattering direction. The enhancement then falls off on an angular scale proportional to $1/k\ell^\star$; in fact the full width at half maximum of the curve is given by $0.75/k\ell^\star$. Thus the investigation of the backscattering cone is a very efficient method of determining the turbidity of a sample as given by $1/\ell^\star$.

10.4 WEAK LOCALIZATION IN EHD TURBULENCE

Anderson localization of light is expected to occur at very strong scattering, that is for $\ell \ll \lambda$. For light it is very difficult to find systems which satisfy this stringent condition. In multiple scattering systems it is possible to get close to the condition $\ell \sim \lambda$, where light localization effects due to recurrent scattering have been already observed. In these systems, for each photon path γ there is a non zero probability that a $-\gamma$ path will also exist. The interference between the two propagating waves results proportional to $\Phi \sim exp[i(\mathbf{k}_i + \mathbf{k}_f) \cdot (\mathbf{x}_0 - \mathbf{x}_N)]$, where $\mathbf{k}_i$ and $\mathbf{k}_f$ represent the incident and the outgoing wave vectors respectively, while $\mathbf{x}_0$ and $\mathbf{x}_N$ represent the coordinates of the first and last scatterer [162]. In the CBS condition ($\mathbf{q} = \mathbf{k}_i + \mathbf{k}_f = 0$), the amplitude of the two waves will be the same ($A_\gamma = A_{-\gamma}$) and will interfere constructively, thus leading to an enhancement of the backscattering cone intensity by a factor $|A_\gamma + A_{-\gamma}|^2 = 4|A_\gamma|$. The mean free path ℓ is related to the scattering cross-section S of the scatterers by the following relation $\ell \sim 1/mS$ (m is the concentration of the scatterers).

In a NLC sample thermal fluctuations of the molecular director $\mathbf{n}(\mathbf{r}) = n_0 + \delta\mathbf{n}(\mathbf{r})$ conduct to fluctuations of the dielectric tensor $\epsilon_{\alpha\beta} = \epsilon_\perp \delta_{\alpha\beta} + (\epsilon_\parallel - \epsilon_\perp) n_\alpha n_\beta$, this effect being the main responsible of the recurrent multiple scattering and the localization of light observed in such systems. In the case of thermal fluctuations [156] (and in absence of external stimuli), the ratio of the scattering cross–sections due to the variation of refraction index caused by thermal fluctuation in NLC sample S_{NLC}, and that owing to arbitrary isotropic scatterers S_{iso} is of the order of $S_{NLC}/S_{iso} \simeq 10^6$ [36]. This indicates that, even in the absence of external stimuli, NLCs provide an important scattering environment, which already proved a striking optical feedback (localization) and is responsible for the random laser action observed in the case of several confinement geometries [88, 161]. Thus, liquid crystalline materials, being interesting reconfigurable media able to reveal dynamical localization of light waves are used as model systems for investigating multiple scattering induced by chaotic dynamics.

In this section we present the first experimental observations regarding the photon dynamical localization in several NLCs turbulent regimes. To our knowledge, the systems investigated up to now, were mainly static nano-powdered solutions or biological tissues, without any external control on the disorder. Here, an anisotropic complex fluid is "driven" throughout chaotic regimes by an external electric field giving rise to several dynamical scattering regimes related to dynamical light localization processes. Even though the system is characterized by a spatial stochastic behavior, constructive interference survives exactly in the backwards direction, forming a well defined CBS cone. The central motivation of this study was born from the importance of exploring the process of light waves dynamical localization in turbulent systems. This phenomenon could reveal significant conceived and still un-conceived features both scientifically and technologically in the field of fluid dynamics and applied optics and photonics. Indeed, the liquid crystals offer unparalleled opportunities to investigate chaotic regimes, since under the action of low frequency electrical stimuli provide a controllable cascade of EHD instabilities until the occurrence of a fully developed turbulence. Previous light depolarization studies [163, 164] emphasize that fully polarized

light waves traveling through NLCs in chaotic regimes can overcome a complete depolarization. This depolarization effect is referable to a remarkable process of multiple scattering which induces substantial randomization of the phases in the wave field.

10.4.1 CBS Experiments in EHD

The experimental setup used for the investigations of CBS is represented by an Off-Centered Rotation (OCR) system [165]. The light source was a He-Ne laser ($\lambda = 632.8nm$) impinging onto the NLC sample by means of a preserving polarization beam splitter. The sample consists of a conventional MBBA sandwiched cell (about $52\mu m$) placed behind a quarter wave plate and a bi-convex lens (L1) used to focus circularly polarized light within the sample and also collect the backscattered light waves. We selected circular light polarization for maximizing the efficiency of the scattering events in the sample when the electric field is switched on and the molecular alignment is broken. An optical fibre is placed in the focus of the positive lens (L2) and connected to a photo multiplier tube (PMT) for collecting the signal. A linear polarizer is employed to select one polarization state for the scattered light while avoiding multiple reflections due to the optical elements. The system is placed on a rotating frame; the center of rotation O' represents the center of rotation O of the sample surface mirrored with respect to the plane of the beam splitter 52(a). Figure 52(b) shows the setup after rotation. The incoming beam is directed to O, while after rotation it still arrives to the rotation center of the sample surface O'. With respect to the frame, the incoming direction has changed but the direction of detection is still the same. By rotating the sample around O, the sample surface is kept at a constant angle with respect to the incoming beam 52(b). The experiments were performed by driving the LC samples through the cascade of EHD instability regimes that were previously observed by means of an optical microscope to clearly individuate the electric field parameters (frequency and amplitude) and the relative dynamic regimes. We analyze a sample cell of MBBA NLC filmm[N-(4-Methoxybenzyliden)-4-butylanilin], planarly aligned on plane x, y, placed between two semitransparent electrodes, and a sinusoidal electric field $\mathbf{E} = (0, 0, E_z)$, at frequency $f = 70Hz$, is applied on the sample. The sample is illuminated by a white light beam polarized along the anchoring direction, and it is observed by an optical microscope connected to the images acquisition system. The instantaneous transmitted light intensity reflects the spatial variation of the refractive index of the sample. In Fig. 53 (a) are shown the convective roll structures characteristic of the Williams domains, while Fig. 53 (b) shows the pattern which originates when the rolls become unstable by increasing the amplitude of the electric field (weak turbulent state). Finally Fig. 53 (c), respectively, the turbulent DSM1 and DSM2 regimes, obtainede for higher voltages of the applied electric field. In DSMs cases the structures that originates

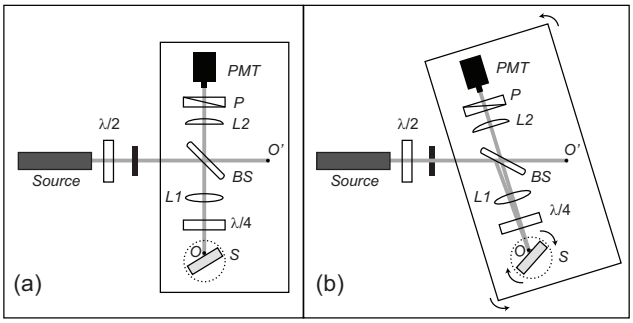

Figure 52: Experimental Set-up. (a) Before rotation and (b) after the rotation of the frame and the sample *S*.

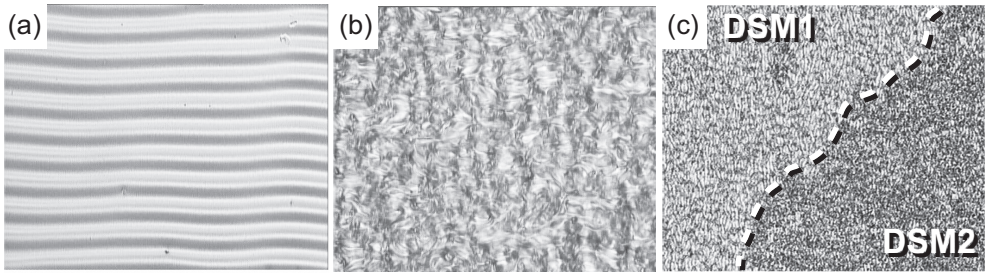

Figure 53: Different electro-hydrodynamical regimes observed under an optical microscope as a function of the applied voltage.

in the sample can be observed only if the focal plane of the microscope coincides with the sample, which means the caustic have no effect on the images formation [166]. Furthermore, for well observing the small scales originates in the turbulent regimes we used an high numerical aperture microscope objective so that the focal depth of the objective was 1/100 the sample thickness. Actually the DSM1 regime is a metastable turbulent state which decays into a DSM2 regime. Tis transition belong to direct percolation universality class (5, B). At a fixed external voltage V_0 the DSM1 regime starts and after a certain lag-time which depends on the applied voltage, the DSM2 "absorbs" the DSM1 regime, and slowly this new state invades all the sample. The measured voltage range for the EHD instabilities at a frequency of 70 Hz were: Williams domains (6V $\rightarrow$ 9V, Fig. 53(a)), weak turbulence (10V $\rightarrow$ 44V, Fig. 53(b)) and DSMs (45V $\rightarrow$ 70V, Fig. 53(c)). The same samples were then analyzed by using the CBS set-up previously calibrated and tested on nano-dispersed powdered solutions (TiO_2) and other NLCs cells in static conditions. For avoiding any artifacts generated by the optical elements interface reflections suitable states of polarization were carefully selected. Additionally, the reflections from the sample glass plates were ruled

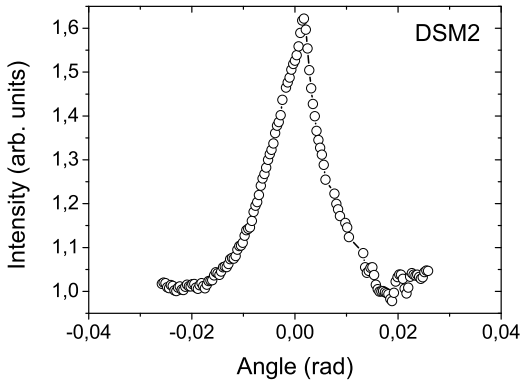

Figure 54: Backscattering cone for DSM2 regime at 70V and f = 70 Hz.

out by rotating the sample of a small angle with respect to the incident light beam, but also in order to mediate on each photon path inside the sample [165]. Upon switching on the low frequency electric field, the multiply scattered light waves surprisingly produced an intense backscattered cone which changed width and amplitude as function of the applied voltage. At low voltage values Williams instability appears. The scattering regime is still polarization sensitive because of the creation of anisotropic scattering areas which are extended over the entire cell thickness. The backscattering cone, with a full width at half maximum (FWHM)

of about 6mrad, measured during the Williams domains, shows an important increment with respect the static case (FWHM about 2mrad) [156]. The coherent cone width increment is strictly related to the scattering mean free path, ℓ. Only in the hyper-diffusive regime (DSM2) ℓ results comparable with the transport mean free path ℓ^*. Figure 54 shows the backscattering cone in the case of the DSM2 regime, where the FWHM results maximum. The excursion through the cascade of EHD instabilities, as evidenced by Fig. 55 (circles), gives rise to a monotonic increase of the coherent cone width. The light waves localized within the distorted loops of the weakly turbulent complex fluid (in the range $10V \rightarrow 44V$) show a scattering mean free path of about 15μm. The three-fold lowering of the mean free path, with respect to the static case, emphasizes the enhancement of the multiple scattering in this dynamic regime, not yet chaotic. In fact, the scattered light waves still preserve

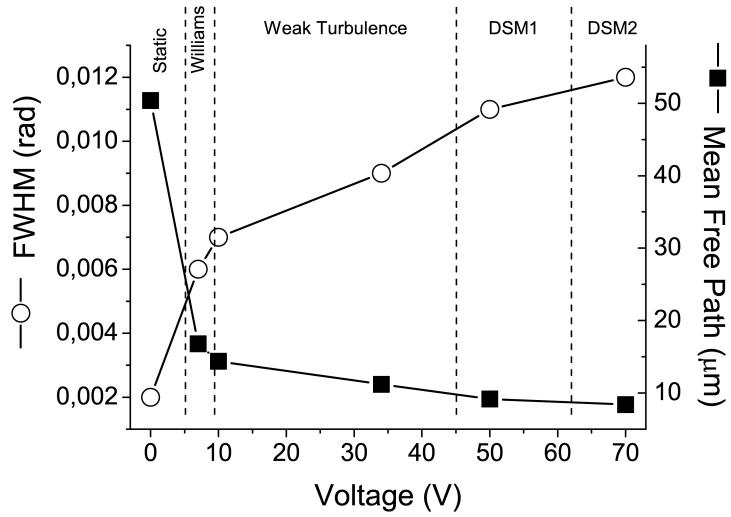

Figure 55: FWHM (circles) and scattering mean free path ℓ (squares) as a function of the applied voltage.

some polarization residual, even though the intensity is importantly reduced with respect the Williams regime. At higher voltages, the spatio-temporal dynamics evolves trough the Hopf bifurcation and the first dynamic scattering mode (DSM1) appears as a rapidly moving grained texture, having a typical size comparable with visible wavelength. Finally, DSM2 nuclei appear and grow until they occupy the entire bulk (Fig. 53(c)).

CBS experiments performed within this fully chaotic regime evidenced striking constructive interference of partial waves traversing momentum-reversed scattering paths in the backscattering direction, accompanied by an almost complete reduction in the amount of light transported throughout the turbulent media. The cone width enlargement during the transition DSM1-DSM2, for a fixed voltage above threshold, emphasizes that a dynamical critical behavior regulates the recurrent multiple scattering process inducing a decrement of the scattering mean free path (about 8μm). In fact, the DSMs bifurcation is regulated by a dramatic director field distortion, manifested as a very strong non-linear flow, since the stresses have surpassed the threshold value of the viscoelastic limit. In conclusion, a remarkable effect of light waves CBS in turbulent anisotropic complex fluids has been reported. The cascade of EHD instabilities in NLCs have been utilized as reconfigurable systems to investigate weak localization phenomena in dynamical regimes characterized by critical behavior. The net reduction of light transport in the forward direction and the robust interference phenomena that survive multiple scattering as evidenced by CBS measurements provide the signature of weak light waves localization effect. This interesting feature opens up fascinat-

ing horizons concerning the opportunity to study random laser action in chaotic systems in presence of high efficiency gain media.

11 CONCLUSION AND REMARKS

Aimed by observations of the retro reflection enhancement of light when a nematic liquid crystals is subject to electrohydrodynamic (EHD) instabilities driven by an externally imposed oscillating electric field, in this thesis we investigated in detail the spatio-temporal stochastic properties of this medium. These information will be used in future for further studies on the anisotropic coherent backscattering. Classical experiments have been obtained by putting a NLC in an oscillaing electric field and collecting the spatio-temporal intensity field $I(\mathbf{x}, t)$, while a confocal fluorescent microscopy technique allows to obtain information on a thin slice inside the sample, that permits to build-up three-dimensional reconstructions of a volume of NLC. High-frequency high-resolution snapshots of the intensity field have been collected at different applied voltages V_0 from experiments.

The Proper Orthogonal Decomposition (POD) analysis, performed for the first time on the NLC medium under EHD turulence, has been used to recover the anisotropic properties of fluctuations. The POD analysis results in a sequence of proper modes ordered by decreasing energy content, whose temporal and spatial eigenfunctions are not given a priori, rather they are obtained from the data. This technique is then particularly suitable to investigate turbulent fluctuations of real field where stationarity and boundary conditions are not ideal. We investigated the scaling behavior of the chaotic pattern generated by the transmitted light intensity in a MBBA NLC. We found that the number of significant POD modes necessary to reproduce about the 99% of the energy is a natural measure to describe the degree of complexity of the system. We found that complexity increases with the applied voltage, with two clear breaks corresponding to the set-up of a weak turbulence regime and the saturation of the Dynamical Scattering Mode (DSM), interpreted as a strong turbulent regime. This means that convective structures observed at smaller applied voltages are distorten and broken by the action of the chaotic dynamics, a fragmentation process which rensemble the occurrence of the nonlinear energy cascade process in the Richardson's phenomenology of usual turbulence in fluid flows. However, at variance to usual turbulence, a real "inertial range" is not observed. In usual fluid flows, as the Reynolds number increases, an inertial region is observed and this is a characteristic of high Reynolds number turbulence. In EHD this is not observed, and the main reason is the fact that the dissipation in EHD is not due to a simple linear ∇^2–term. Rather, the dissipative terms in NLC are nonlinear and anisotropic. This means that the dynamic towards a complex turbulent behavior is different, and is characterized by the dimensionless parameter V_0/V_{th} (being V_{th} the threshold voltage for William Domain to appear). Even when this parameter is a bit larger than unity, the system is driven in a state of weak turbulence. Quite interestingly we found the presence of subleading pattern at small-scales in the weak and DSM1 regimes. In this case the small-scale structures self-organize through a large-scale pattern that still represents a kind of convective roll of fragmented structures with a coherent dynamic. At the highest voltages, in the DSM2 regime, the above pattern is lost, even if subleading anisotropic properties still persist, that is small-scale structures tend to be oriented along the Williams rolls axis direction. This is similar to other anisotropic fluids, as a hydromagnetic fluid, where anisotropy persists even at small scales, at variance to the Kolmogorov assumption of small-scales return to isotropy.

One of the main feature of fluctuations, as observed during EHD turbulence is the presence of intermittency, which are here investigated in detail for the first time. This is a property of turbulence in usual fluid flows which is observed also in our experiments of EHD instabilities. Intermittency means that the probability of standardized fluctuations of the transmitted

intensity, at a given scale, depends on the scale itself. This means that scaling laws of moments of fluctuations are anomalous, that is the scaling dynamics is far from being globally self-similar. We investigate the occurrence of intermittency through the analysis of the PDFs scaling behavior at a given scale r in the different regimes induced by V_0. Our results can be summarized as follows.

1. In the WT regime, PDFs evolve with the lag r from large scale Gaussian towards high winged distribution. This is the typical phenomenology observed in intermittent fully developed fluid turbulence. The non self-similar hierarchy of structures generated at all scales, identified as usual through scaling of fluctuation PDFs, is likely due to nonlinear interactions in the system. Intermittency is often interpreted as the result of non-homogenous distribution of turbulent structures, which accumulate at small scales.

2. On the contrary, non-Gaussian PDFs in both DSM regimes change shape only weakly with the scale, suggesting a kind of turbulence more similar to global self-similarity for both perpendicular and parallel fluctuations (with respect to the original Williams domain direction). This can be interpreted as a saturation of the nonlinear cascade of energy, resulting in the stochastic superposition of structures of the same type on all scales. Similar behaviour is commonly observed in the dissipative range of fluid turbulence. From the comparison between parallel and perpendicular fluctuations, it is also evident that anisotropy is not relevant in the generation of small-scale structures at high voltages.

3. We propose to describe the scaling behavior of PDFs through a model, in which the shape of the distribution function is characterized by a scale dependent parameter $\lambda(r)$. The model is based on the conjecture that a Log-normal distribution can, according to the central limit theorem, describe the statistics as the superposition of scale dependent, local statistics, in a multifractal framework of turbulence. In this view, turbulent structures are interpreted as the result of a fragmentation process through a multiplicative cascade, due to nonlinear interactions, so that large-scale structures break down into smaller and smaller structures. The model is able to reproduce the scaling behavior of experimental PDFs, so that a nonlinear multiplicative cascade process can be invoked to explain the generation of fluctuations in the system, according to earlier conjectures. The scaling laws of the parameter $\lambda(r)$ allow a quantitative description of intermittency in the different regimes and depths inside the sample. Difference between the intermediate voltage intermittent case, and the high voltage quasi self-similar case can thus be quantified.

4. In general, the observed non-Gaussian behaviour is more evident closer to the top boundary of the sample cell. This effect is probably due to the presence of electrode-NLC interface, which strongly influence the fragmentation process. It should be noticed that it is not possible to rule out the possibility that the dynamics at such voltage could be faster than the data sampling, so that correlations could be lost due to low temporal resolution.

Where the origin of intermittency comes down? To answer this main question, I presented results on the study of elastic energy clustering during EHD instabilities in a NLC. A measure describing a surrogate of the elastic energy density were observed to show strong inhomogeneities in their spatial distribution. By extending previous studies, we showed that the coarse-graining energy density can be characterized by a multifractal distribution. In the thesis we analyzed, for the first time, what happens to the whole bulk of the NLC sample under the action of an external electric field, through new sophysticated measurements. We

found that the distortion energy is stronger far from the surface, where small-scale structures tends to concentrate due to the lower influence of the anchoring energy. The turbulent dynamics tends to generate singular structures of the energy density and important clustering effects are observed for high values of the external applied voltage V_0, when NLC is in a fully developed turbulent state. When this state is reached the whole bulk is influenced by the energy distortion. In this case, the elastic energy concentrated in the center of the sample becomes so strong that it influences the anchoring of the NLC at the boundary glass plates. The clustering of elastic energy, induced by the fragmentation process which gives rise to small-scale fluctuations, is the main physical effect responsible for the presence of strong very localized fluctuations, and then to the presence of intermittency.

A very interesting and basic property of turbulent fluctuations, investigated here for the first time, is the occurrence of the spatio-temporal decorrelation processes in EHD turbulence. Note that no many experimentalsituations exists where both the spatial and temporal decorrelations in turbulent fields. The scaling law $\gamma \sim k_{\perp}^{2/3}$ was found for the decorrelation rate in the perpendicular direction, suggesting a straining process resulting from fragmentation of large scale structures. In the direction parallel to the large scale structures a transition occurs at $\epsilon = \epsilon_c \simeq 3.5$. At lower voltages we recover the scaling law $\gamma \sim k_{\parallel}^{2/3}$, while at $\epsilon > \epsilon_c$ an increasingly relevant role of the sweeping effect is recorded, and the scaling exponent approaches $\mu \simeq 1$ at higher voltages. Our conjecture on the role of decorrelation process provides an estimate of the characteristic random velocity u_0, responsible for the sweeping. The velocity linearly increases with the external applied voltage V_0, with a slope change at ϵ_c, in good agreement with independent direct measurements of the characteristic speed previously found in similar systems. The anisotropic crossover between nonlinear straining and random sweeping decorrelation can be related to the transition from a weaker to a stronger turbulent regime in EHD. These results are very interesting from a general point of view, becouse they show that processes as the decorrelation properties of fluctuations, usually related to turbulent fluid flows, are universal. In this perspective, NLC under EHD instabilities, can be seen as a very promising turbulent medium where experiments can be easily performed. I expect that other physical systems, characterized by fragmentation processes which generate a hyerarchy of fluctuations on all scales, can share the same properties.

Finally, I presented first results of the dynamics of coherent backscattering experiments performed within the fully chaotic dynamical scattering mode regime, thus evidenced striking constructive interference of partial waves traversing momentum-reversed scattering paths in the backscattering direction. This is accompained by an almost complete reduction in the amount of light transported throughout the turbulent NLC. The cone width enlargement during the transition between DSM1 and DSM2, for a fixed voltage above threshold, emphasizes that a dynamical critical behavior regulates the recurrent multiple scattering process inducing a decrement of the scattering mean free path ℓ. In fact, the DSMs bifurcation is regulated by a dramatic director field distortion, manifested as a very strong non-linear flow, since the stresses have surpassed the threshold value of the viscoelastic limit.

The remarkable effect of phenomena that survive multiple scattering provide the signature of weak light waves localization effect. This feature, opens up fascinating horizons concerning the opportunity to study random and chaotic laser action in anisotropic systems in presence of high efficiency gain media. Investigation of anisotropic properties of NLC under EHD instabilities, and in particular their statistical properties, will allow us to deeply understand and better modeling the backscattering and the lasing action.

Appendix

A PROPERTIES OF THE POD

CONTENTS

A.1 Span of the Empirical Basis 103
A.2 Optimality 106
A.3 Symmetry 108
A.4 Attractors 110

In much of the literature cited thus far in this chapter the POD is primarily regarded as a tool for the analysis of experimental data. We now wish to view it in a more dynamical context. Thoughout the remainder of the chapter the reader should imagine that the ensembles from which the autocorrelation function and empirical bases are generated, originate from solutions belonging to the *attractor* of a dynamical system such as the Navier-Stokes equation, realised either by a physical or a numerical experiment. In the best case, the attractor will be *ergodic*, which means that time averages and averages over the part of phase space containing the attractor coincide. In this case the initial conditions are "forgotten" as time proceeds, much as in the common hypothesis that certain turbulent flows relax in physical space to "universal equilibrium states" [167].

The following sections describe properties that will be especially important in our use of the POD to derive low-dimensional models. In the first two we characterise the classes of functions that can be represented by empirical bases and explain precisely how such representation preserve properties of the observation from which they are derived nd how they are optimal. We then consider symmetries, showing that in the case of translational invariance (homegeneous directions), the empirical eigenfunctions are simply Fourier modes, and obtaining results on ergodic attractors invariant under more general symmetry groups. We then show how the rate of decay of the empirical eigenvalues determines geometrial properties of the attractor and how theoretical results on the regularity of solutions of governing evolution equations are related to this.

A.1 SPAN OF THE EMPIRICAL BASIS

The first step is understanding what can be done with representations using empirical eigenfunctions is in characterising the class of functions which can be accurately represented by the *relevant* elements of the basis: those containing spatial structures having finite energy on average. This is the set $S = \{\sum a_j \phi_j | \ \sum |a_j|^2 < \infty, \lambda_j > 0\}$, or $\text{span}\{\phi_j | j = 1, ..., \infty, \lambda_j > 0\}$. In this section, equality of functions will be interpreted as almost everywhere in the spatial domain Ω with respect to Lebesgue measure: two functions f and g are equal in this sense if

$$\int_\Omega |f - g|^2 dx = 0; \tag{A.1}$$

This is the mathematical definition of *accurately*. We shall also frequently a second notion of *almost every member of an nsemble with respect to the probability measure underlying the averaging operation* $\langle\cdot\rangle$. This is denoted by *a.e.*. In applications this average will typically be a finite sum

over a set of realisations or an integral over a finite-time experimental run, but the theory is developed in the ideal case of infinite data sets.

A standing assumption in this section is that the averaged autocorrelation $R(x,x')$ is a continuous function. Discontinuities in R can lead to a negative values in the power spectrum[1] and negative energies are unresonable on physical ground. Whe first show that the empirical basis can reconstruct any function that is indistinguishable in the sense of (A.1) from a member of the original ensemble $\{u^k\}$. Let $u \in L^2(\Omega)$ be any such function and ϕ_j be the orthonormal sequence of empirical eigenfunctions. The reconstruction of u will be a function $u_s(u) = \sum_j (u,\phi_j)\phi_j$, belonging to S^2. We need to show that for a.e. u with respect to the ensemble average, we have $u = u_s(u)$; that is:

$$\langle \|u - u_s\|^2 \rangle = 0. \tag{A.2}$$

From the arl value of u, we have

$$\langle \|u(x) - u_s(x)\|^2 \rangle = \langle (u-u_s, u-u_s) \rangle = \langle (u,u) - 2(u,u_s) + (u_s,u_s) \rangle. \tag{A.3}$$

Since the functions u are the members of the original ensemble, we have:

$$\langle (u,u) \rangle = \left\langle \int_\Omega u(x)u^\star(x)dx \right\rangle = \int_\Omega R(x,x)dx \tag{A.4}$$

and also

$$\begin{aligned}
\langle -2(u,u_s) \rangle &= -2\left\langle \int_\Omega u(x) \left[\sum_j (u^\star,\phi_j^\star)\phi_j^\star(x) \right] dx \right\rangle \\
&= -2\left\langle \int_\Omega u(x) \sum_j \left[\int_\Omega u^\star(x')\phi_j(x')dx' \right] \phi_j^\star(x)dx \right\rangle \\
&= -2\int_\Omega \sum_j \left[\int_\Omega \langle u(x)u^\star(x')\rangle \phi_j(x')dx' \right] \phi_j^\star(x)dx \\
&= -2\int_\Omega \left(\sum_j \Re\phi_j \right) \phi_j^\star = -2\int_\Omega \sum_j \lambda_j \phi_j(x)\phi_j^\star(x)dx \\
&= -2\int_\Omega R(x,x)dx.
\end{aligned} \tag{A.5}$$

1 the Fourier transform of R

2 By Parseval's inequality we know that $\sum_j |(u,\phi_j)|^2$ converges

The third term of Eq. (A.3) is:

$$\begin{aligned}
\langle (u_s, u_s) \rangle &= \left\langle \int_\Omega \left[\sum_i (u, \phi_i) \phi_i(x) \right] \left[\sum_j (u^\star, phi_j^\star) \phi_j^\star(x) \right] dx \right\rangle \\
&= \left\langle \sum_{i,j} (u, \phi_i (u^\star, \phi_j^\star) \int_\Omega \phi_i(x) \phi_j^\star(x) dx \right\rangle \\
&= \left\langle \sum_j \int_\Omega u(x) \phi_j^\star(x) dx \int_\Omega u^\star(x') \phi_j(x') dx' \right\rangle \\
&= \sum_j \int_\Omega \left[\int_\Omega \langle u(x) u^\star(x') \rangle \phi_j(x') dx' \right] \phi_j^\star(x) dx \\
&= \sum_j \int_\Omega \lambda_j \phi_j(x) \phi_j^\star(x) dx. \qquad \text{(A.6)}
\end{aligned}$$

Using the continuity of R we can apply Mercer's theorem for the uniform convergence of the series expression for R and interchange summation and integration, obtaining

$$\sum_j \int_\Omega \lambda_j \phi_j(x) \phi_j^\star(x) dx = \int_\Omega R(x, x) dx \qquad \text{(A.7)}$$

Combining Eq. (A.4), (A.5), (A.6) we obtain Eq. (A.2).

We have shown that almost every member of the original ensemble can be reconstructed as a linear combination of empirical eigenfunctions having strictly positive eigenvalues. Now we want to show the converse: that each such eigenfunction can be expressed as a linear combination of observations. This will imply that any property of the ensemble members that is preserved under linear combination is inherited by the empirical basis functions and hence by elements of S.

Let X denote the set of functions (of full measure with respect to the averaging operation) for shich reconstructions satisfying Eq. (A.2) are possible, and let Θ be any functions in S. We claim that there is a sequence $\{b_j\}_{j=1}^\infty$ of real numbers and a set of functions $u^j(x) \in X$ for $j = 1, ..., \infty$ such that

$$\Theta(x) = \sum_{j=1}^\infty b_j u^j(x). \qquad \text{(A.8)}$$

It immediately follows from Eq. (A.8) thai if $\mathcal{P}$ is a closed linear property of a subsset of unctions in $L^2(\Omega)$[3] and all the ensemble members u^k share that property, then the eigenfunctions of the POD also share the property. The converse holds too Eq. (A.8) and this remark characterise the *empirical subspace S*.

It remains to justify Eq. (A.8). Let S′ denote the set of all functions in $L^2(\Omega)$ with representation $\sum_i b_i u^i$ with $u^i \in X$. We will show that $S'^\perp = S^\perp$, from which it follows that $S' = S$, and so the equation indeed holds.

Now $S^\perp$ is exactly the set of functions Θ such that $(\Theta, \phi_i) = 0$ for every ϕ_i with eigenvalue $\lambda_i > 0$. From the first result of this section we have $u(x) = \sum b_i \phi_i(x)$ where $\lambda_i > 0$ for a.e. u. Thus we have $(\Theta, u) = 0$ a.e. and so $(\Theta, \sum_i b_i u^i) = 0$. This show that $S^\perp \supset S'^\perp$.

3 *i.e.* all $u \in L^2(\Omega)$ with property $\mathcal{P}$ from a closed linear subspace

To show $S^\perp \supset S'^\perp$ and hence conclude $S^\perp = S'^\perp$, assume that $(\Theta, u) = \int_\Omega \Theta(x')u^\star(x')dx' = 0$ for a.e. u. Therefore for a.e. u we have $u(x)\int_\Omega u^\star(x')\Theta(x')dx' = 0$, and taking the average we get

$$\int_\Omega \langle u(x,t)u^\star(x',t)\rangle\Theta(x')dx' = 0 \tag{A.9}$$

which, form the eigenvalue equation (8.6), implies that $(\Theta, \phi_i) = 0$ for every i such that $\lambda_i > 0$.

The classic example of a property which passes from the data ensemble to the empirical basis is incompressibility. if the autocorrelation tensor $\mathbf{R} = \langle \mathbf{u}(\mathbf{x},t) \otimes \mathbf{u}^\star(\mathbf{x}',t)\rangle$ is formed from realisations of divergence-free vector field $\mathbf{u}$, then the empirical eigenfunctions $\mathbf{ffi}_j(\mathbf{x})$ are also divergence-free. This will be very useful when we project the Navier-stokes equations onto a subspace spanned by a collection of these eigenfunctions. Other important properties inherited by the eigenfunctions include those of satisfying linear boundary conditions, such as no-slip or no-penetration condition on fixed surfaces.

We now have a characterisation of the span of the eigenfunctions whit strictly positive eigenvalues. This linear space S exactly coincides with that spanned by all realisations $u^k(x)$ of the original ensemble a.e. with respect to the measure induced by the averaging operations. From this wee see that the set of empirical eigenfunctions $\{\phi_j | \lambda_j > 0\}$ need not from a complete basis of $L^2(\Omega)$. While S may be infinite dimensional, it is generally only a subset of the "big" space $L^2(\Omega)$ in which we are working. It is complete only if one include the kernel of the operator $\mathfrak{R}$[4], but in doing so one loses the major advantage of the POD, for in many application one can argue on physical ground that the realisations $u(x,t)$ do not and should not span $L^2(\Omega)$ (*many strange things may happen in turbulence, but not everything*). In such cases the discussion of this section highlights a strong property of the POD. Its use limits the space studied to the smallest linear subspace that is sufficent to describe the observed phenomena.

A.2 OPTIMALITY

Suppose we have a decomposition of a time-dependent, statistically stationary signal $u(x,t)$ with respect to any orthonormal basis $\Psi_j(x)_{j=1}^\infty$:

$$u(x,t) = \sum_j b_j(t)\Psi_j(x). \tag{A.10}$$

If the $\Psi_j(x)$ are dimensionless, then the coefficients $b_j(t)$ carry the dimension of the quantity u. If $u(x,t)$ is a velocity and $\langle\cdot\rangle$ is a time average, the average kinetic energy per unit mass over the experiment is given by

$$\begin{aligned}\frac{1}{2}\left\langle \int_\Omega u(x,t)u^\star(x,t)dx \right\rangle &= \left\langle \sum_{i,j} b_i(t)b_j^\star(t)\int_\Omega \Psi_i(x)\Psi_j^\star(x)dx \right\rangle \\ &= \frac{1}{2}\sum_i \langle b_i(t)b_i^\star(t)\rangle\end{aligned}$$

and so the average kinetic energy in the j-th mode is given by $1/2\langle b_i(t)b_j^\star(t)\rangle$ (no summation implied).

We can now precisely state optimality for the POD. Suppose that we have a stationary random field $u(x,t)$ in $L^2(\Omega)$ and that $\{\phi_i, \lambda_i | i = 1, ..., \infty, \lambda_i \geqslant \lambda_{i-1} \geqslant 0\}$ is the set of

4 all the (generalised) eigenfunctions with zero eigenvalue

orthonormal empirical eigenfunctions with their associated eigenvalues obtained from time averages of $u(x,t)$. Let

$$u(x,t) = \sum_j a_j(t)\phi_j(x) \tag{A.11}$$

be the decomposition with respect to this basis and let $\{\Psi_j(x)\}_{j=1}^{\infty}$ be any other arbitrary orthonormal set such that

$$u(x,t) = \sum_j b_j(t)\Psi_j(x) \tag{A.12}$$

then the following hold:

1. $\langle a_j(t)a_j^\star(t)\rangle = \delta_{ij}\lambda_i$; *i.e.* the pod random coefficients are uncorrelated
2. for every n we have

$$\sum_{i=1}^{n}\langle a_j(t)a_j^\star(t)\rangle = \sum_{i=1}^{n}\lambda_j \geqslant \sum_{i=1}^{n}\langle b_i(t)b_i^\star(t)\rangle;$$

   i.e. the POD is optimal on average in the class of representations by linear superposition: the first n POD basis functions capture more energy on average than the first n functions of any other basis.

The first assertion derives from the representation of $R(x,x')$, given in Eq. (8.7):

$$\begin{aligned} R(x,x') = \langle u(x,t)u^\star(x',t)\rangle &= \left\langle \sum_i a_i(t)\phi_i(x)\sum_j a_j^\star(t)\phi_j^\star(x')\right\rangle \\ &= \sum_{ij}\langle a_i(t)a_j^\star(t)\rangle\phi_i(x)\phi_j^\star(x') \end{aligned}$$

But we know that

$$R(x,x') = \sum_i \lambda_i\phi_i(x)\phi_i^\star(x'), \tag{A.13}$$

and so, since the $\phi_i^\star(x)$ are an orthonormal family in $L^2(\Omega)$, we see that $\langle a_i(t)a_j^\star(t)\rangle = \delta_{ij}\lambda_i$. The second assertion relies on a result on linear operators. Let $\{\Psi_j(x)\}_{j=1}^{n}$ be n arbitrary orthonormal vectors in $L^2(\Omega)$ that may be completed to form an orthonormal basis. Let Q denote projection onto $\operatorname{span}\{\Psi_1,\ldots,\Psi_n\}$. We can express the kernel R in terms of $\{\Psi_j\}_{j=1}^{\infty}$ as

$$R(x,x') = \left\langle \sum_i b_i(t)\Psi_i(x)\sum_j b_j(t)\Psi_j^\star(x)\right\rangle = \sum_{i,j}\langle b_j b_j^\star\rangle\Psi_i\Psi_j^\star. \tag{A.14}$$

We can then write R in operator matrix notation as

$$R = \begin{bmatrix} \langle b_1 b_1^\star\rangle & \langle b_1 b_2^\star\rangle & \langle b_1 b_3^\star\rangle & \ldots \\ \langle b_2 b_1^\star\rangle & \langle b_2 b_2^\star\rangle & \ldots & \ldots \\ \langle b_3 b_1^\star\rangle & \ldots & \ldots & \ldots \\ \vdots & \vdots & \vdots & \vdots \end{bmatrix}$$

and the product $R \circ Q$ yields

$$R = \begin{bmatrix} \langle b_1 b_1^\star \rangle & \langle b_1 b_2^\star \rangle & \dots & \langle b_1 b_n^\star \rangle & 0 \dots & 0 \dots \\ \langle b_2 b_1^\star \rangle & \langle b_2 b_2^\star \rangle & \dots & \langle b_1 b_n^\star \rangle & 0 \dots & 0 \dots \\ \vdots & \vdots & \vdots & \vdots & \vdots & \vdots \\ \langle b_n b_1^\star \rangle & \langle b_n b_2^\star \rangle & \dots & \langle b_n b_n^\star \rangle & 0 \dots & 0 \dots \\ 0 \dots & 0 \dots & 0 \dots & 0 \dots & 0 \dots & 0 \dots \\ \vdots & \vdots & \vdots & \vdots & \vdots & \vdots \end{bmatrix}.$$

From [168], we know that the sum of the first n eigenvalues of a self-adjoint operator is greater than or equal to the sum of the diagonal terms in any n-dimensional Projection of it:

$$\sum_{i=1}^{n} \lambda_i \geqslant \mathrm{Tr}(R \circ Q) = \sum_{i=1}^{n} \langle b_i b_i^\star \rangle. \tag{A.15}$$

This characterisation is the basis for the claim that the POD is optimal for modelling or reconstructing a signal $u(x,t)$. It implies that, among all linear decompositions, the POD is the most efficient in the sense that for a given number of modes, n, the projection on the subspace spanned by the leading n empirical eigenfunctions contains the greatest possible kinetic energy on average. Moreover, the time series of the coefficients $a_j(t)$ are linearly uncorrelated.

A.3 SYMMETRY

We start by describing a particular kind of symmetry, called homogeneity in the turbulence literature. We say that the averaged two point correlation $R(x,x')$ is *homogeneous* if $R(x,x') = R(x-x')$ *i.e.* R depends only on the difference of the two coordinates: it is translation invariant. In general, homogeneity of a system is defined through multipoint moments. Here we need only second order moments, but it is important to note that, while the ensemble of realisations $\{u^k\}$ may be translation invariant on average, individual realisations are typically not. Homogeneity occurs in both spatially unbounded systems and systems with Aperiodic boundary conditions. In either case we may develop R in a Fourier representation. In the case of a finite domain, we have the series

$$R(x-x') = \sum c_k e^{2\pi i k(x-x')}. \tag{A.16}$$

We can then solve the eigenvalue problem (8.6) by substituting the (unique) representation

$$R(x,x') = \sum c_k e^{2\pi i k x} e^{-2\pi i k x')}, \tag{A.17}$$

which implies that $\{e^{2\pi i k x}\}$ are exactly the eigenfunctions with eigenvalues c_k. Conversely, if the eigenfunctions are Fourier modes we can write Eq. (A.17), which implies Eq. (A.16). However, while homogeneity completely determines the form of the empirical eigenfunctions, the numerical values and ordering of the *eigenvalues* depend upon the Fourier spectrum of the particular data set involved. In summary we can state:

- If $R(x,x') = R(x-x')$ is homogeneous, then the eigenfunctions of the operator $\mathfrak{R} = \int_\Omega R(x,x') \cdot dx'$ are Fourier modes, and vice versa.

This is especially useful in systems where the domain Ω is of higher dimension. For example, if $\Omega \subset R^2$ and the x_1-direction is homogeneous, the problem of finding eigenfunctions in the two-dimensional domain is decoupled into a set of one-dimensional problems by writing

$$R(x_1, x_1', x_2, x_2' = R(x_1 - x_1', x_2, x_2') \tag{A.18}$$

and performing the same procedure as above, yielding an eigenvalue problem for each Fourier wavenumber. In the decomposition of the boundary layer we appeal to homogeneity in the spanwise (x_3) and streamwise (x_1) directions, appropriate to a fully developed flow in, say, a channel or a pipe. Selecting the (finite) domain $[0, L_1] \times [0, L_3]$ in these variables, we may then use a mixed discrete Fourier-empirical decomposition of the form

$$\mathbf{u}(\mathbf{x}, t) = \sum_{k_1} \sum_{k_3} \sum_{n} a_{k_1,k_3,n}(t) e^{2\pi i \left(\frac{k_1 x_1}{L_1} + \frac{k_3 x_3}{L_3}\right)} \phi_n(k_1, k_3; x_2). \tag{A.19}$$

The vector-valued eigenfunctions $\phi_n(k_1, k_3; x2)$ in Eq. (A.19) are obtained by solving an operator equation in which the kernel $\mathbf{R}(x_1 - x_1', x_2, x_2', x_3 - x_3')$ is replaced by its Fourier transform in the x_1 and x_3 directions. In the turbulent boundary layer, as in other problems with one or more homogeneous directions, this decomposition produces structures that are not localised in spanwise and streamwise extent, unlike the (instantaneous) events observed.

Homogeneity or translation invariance is only one of many types of symmetry that physical systems may exhibit. It is an example of a continuous symmetry group, for we may make translations by any distance. Discrete groups are also common: in the case of a boundary layer over a surface treated with riblets - strakes parallel to the mean flow direction - one would have spanwise symmetry only with respect to translations through multiples of the riblet spacing. A jet with a lobed mixer would similarly exhibit symmetry under discrete rotations. However, we stress that while a physical system or a model of it in the form of a dynamical system may well admit such symmetries, we cannot expect either individual observations (solutions) or even ensembles of them to share the full underlying symmetry group. In mathematical terms, the system will generally not be ergodic. A simple example of this can be a reflection symmetric two-dimensional ODE possessing two stable fixed points. Any given solution can only approach one of these, and so to reveal the full structure of the attractor, one must average over a set of initial conditions chosen in light of the symmetry. More generally, if a system has several distinct attractors, the time average of a single solution will reproduce just one of these and so the empirical eigenfunctions generated by time averaging from one experimental run will enjoy less symmetry than the problem as a whole. To make a precise statement characterising the relation between underunderlying symmetries and subspaces spanned by the empirical eigenfunctions. we need the notions of equivariant dynamical systems and invariant subspaces (not discussed here). To undestand this, we need a few preliminaries, which we give in the context of finite-dimensional ODEs. Let

$$\dot{\mathbf{x}}\mathbf{f}(\mathbf{x}) \tag{A.20}$$

be an n-dimensional system and Γ be a symetry group acting on the phase space $\mathbb{R}^n$: the elemnts γ of Γ being $n \times n$ matrices. To say that (A.20) is *equivalent* under Γ means that the equation

$$\gamma\mathbf{f}(\mathbf{x}) = \mathbf{f}(\gamma\mathbf{x}) \tag{A.21}$$

holds for every $\gamma \in \Gamma$. This implies that if $\mathbf{x}(t)$ is a solution of (A.20), then so is $\gamma\mathbf{x}(t)$ (think of the two fixed points of the reflections symmetric system mentioned above). Equivariance

also typically implies that eigenvalues come in multiples, for if **A** denotes the linearisation of **f**, then we have from (A.21)

$$\gamma \mathbf{A}\mathbf{v} = \gamma\lambda\mathbf{v} = \lambda\gamma\mathbf{v}$$

and also

$$\mathbf{A}\gamma\mathbf{v} = \lambda\gamma\mathbf{v}$$

implying that if **v** is an eigenvector with eigenvalue λ, then so is $\gamma\mathbf{v}$. The eigenspaces of the operator $\mathfrak{R}$ are similarly constrained by symmetries, so that one typically expects several distinct eigenfunctions for a given eigenvalue, corresponding to the same structure differently oriented or located in physical space.

After this preamble, we can now give the gist of the result.

- If ϕ_j and λ_j are the empirical eigenfunctions and eigenvalues generated from a set of solutions (experiments) $\{u^k\}$ of a dynamical system equivariant under a group Γ, then a necessary condition for the flow generating $\{u^k\}$ to be ergodic is that each of the finite-dimensional eigenspaces corresponding to a given empirical eigenvalue be invariant under Γ.

The way one might check this condition experimentally would be to:

1. Perform the experiment to measure $R(x, x')$.
2. Decompose $R(x, x')$ using the POD: $R(x, x') = \sum \lambda_i \phi_i(x)\phi^\star(x')$.
3. Check that for every eigenfunction $\phi_j \in N_{\lambda_m}$ =span$\{\phi_j | \lambda_j = \lambda_m\}$ and every $\gamma \in \Gamma, \gamma(\phi_j) \in N_{\lambda_m}$.

Aubry et al. [169] computed POD bases from numerical integrations of the Kuramoto-Sivashinksy equation and concluded that for certain values of the bifurcation parameter the system is not ergodic. On the other hand, if one assumes that a system is ergodic one may use its symmetries to increase the size of the ensemble, generating additional data sets $\{\gamma u^k\}$ from a set of observations $\{u^k\}$ which only represent a limited region of the full attracting set. This approach has been advocated by Sirovich in [170] and adopted in many studies. However, one should be cautious, as there are examples for which the partition into ergodic components is finer than the partition into symmetric components. In this case the image of the basis obtained by one experiment under the symmetry group will not produce the basis obtained by the ensemble average measure. The ergodicity assumption is questionable particularly in cases of "small" systems or special geometries. For example in a square Rayleigh-Benard cell there is a possibility that the rotation direction of the single roll selected at the time of onset may never change throughout the life of the experiment. This indicates that there are at least two distinct and disjoint parts for the support of the invariant measure, each associated with a rotation direction, hence it is not ergodic. Similar phenomena appear to occur in the minimal flow unit of the channel flow simulations by Jimenez and Moin [171].

A.4 ATTRACTORS

If the observations $\{u^k(x)\}$ from which the POD is generated come from a solution (or solutions) $u(x, t)$ of a dynamical system, then the empirical eigenfunctions and eigenvalues contain information on the attractor(s) of that system. We have already discussed symmetries. In this section we develop this observation in several other ways. We first give a probabilistic-geometric interpretation of the location of the dynamics in phase space using Chebyshev's inequality [172]:

Chebyshev's inequality:
Let $\mathbf{x}$ *be a vector-valued random variable, with mean* $\langle \mathbf{x} \rangle$ *and variance* $\sigma^2 = var(\mathbf{x}) = \langle |\mathbf{x} - \langle \mathbf{x} \rangle|^2 \rangle$. *Then for any* $\epsilon > 0$

$$\langle 1_{|\mathbf{x}-\langle \mathbf{x} \rangle| > \epsilon} \rangle = P\{|\mathbf{x} - \langle \mathbf{x} \rangle| \geqslant \epsilon\} \leqslant \frac{\sigma^2}{\epsilon^2},$$

where the indicator function $1_S(\epsilon) = 1$ *if* $S \geqslant \epsilon$ *and* 0 *otherwise.*

Chebyshev's inequality expresses the notion that the variance says something about the frequency of departures from the mean. In our case we define

$$S_n(\epsilon) = \left\{ u \in L^2(\Omega) | \sum_{m=n+1}^{\infty} |(u, \phi_m)|^2 < \epsilon \right\},$$

and

$$W_n(\epsilon) = L^2(\Omega)/S_n(\epsilon).$$

Here $S_n(\epsilon)$ is a slab of thickness 2ϵ around the finite-dimensional space span$\{\phi_1, ..., \phi_n\}$ and $W_n(\epsilon)$ is the rest of phase space, outside this slab. Note that Sn(e) is infinite-dimensional. We will use Chebyshev's inequality to estimate the fraction of the time spent by solutions $u(x,t)$ in $S_n(\epsilon)$. Denote by $\mathbf{x}_n$ the vector-valued random variable

$$\mathbf{x}_n(t) = \{(u, \phi_m)\}_{m=n+1}^{\infty} \tag{A.22}$$

representing the infinite "tail" of the process. Then we have $\langle \mathbf{x}_n \rangle = 0$ and $\sigma^2(\mathbf{x}_n) = \sum_{m=n+1}^{\infty} \lambda_m$ and therefore, by Chebyshev's inequality,

$$P\{u \in W_n(\epsilon)\} = P\{|\mathbf{x}_n| \geqslant \epsilon \leqslant \frac{\sum_{m=n+1}^{\infty} \lambda_m}{\epsilon^2}. \tag{A.23}$$

To obtain a useful result, one lets $\epsilon \to 0$ for fixed n via s subsequence $\epsilon_n \to 0$ satisfying

$$\frac{\sum_{m=n+1}^{\infty} \lambda_m}{\epsilon_n^2} \to 0; \tag{A.24}$$

in other words, the ϵ_n's are chosen such that their squares go to zero slower than the decay of norm in the residual modes. This gives a series of slabs whose thicknesses go to zero while the probability of solutions being in those slabs goes to one. The problem now becomes that of estimating the rate of decay of the residual eigenvalue $\sum_{m=n+1}^{\infty} \lambda_m$ in the tail.The analytical evidence outlined below suggests that, when the POD basis is used for turbulent flows, this residual decays at least exponentially fast asymptotically. This enables us to take a series $\epsilon_n^2 \to 0$, with a slightly smaller exponent. The liesult will be a sequence of slabs with thicknesses going exponentially to zero, while the probability of solutions being in a slab goes exponentially to one. This creates a picture in which an attractor is very thin, although possibly infinite-dimensional. It is reasonable to postulate, even in this case, that the essential dynamics are controlled by a finite number of modes. There is even a technical refinement to this in [173].

In the dynamical systems literature a lot of effort has gone into developing methods for the estimation of dimension of attractors. The underlying idea is that, if the attractor of an infinite-dimensional evolution equation is finite-dimensional, then it should be possible to

extract a finite-dimensional model in the form of a set of ODEs of comparable dimension. It is natural to try to relate the POD to such ideas, and even to define a dimension using empirical eigenvalues. Perhaps the most obvious thing to do is to define a (Karhunen-Loeve) dimension as the number of non-zero eigenvalues in the POD, as suggested by Aubry et al. [174]. However, the number of non-zero eigenvalues is the dimension of the smallest linear subspace containing the dynamics, and it consequently provides only a very crude upper bound for the (Hausdorff) dimension of the attractor. Even if the attractor dimension is finite the linear subspace may not be finite-dimensional. It is easy to construct an example having a limit cycle (of dimension 1) which "twists" around in infinitely many directions in the function space and so generates data having an infinite number of non-zero eigenvalues. Indeed, as Sirovich realised in [175], this naive definition is not very useful. He suggested the following working definition: " ... introduce $\dim_{KL}$..., the number of actual eigenfunctions required so that the captured energy is at least 90% of the total..., and that no neglected mode, on the average, contains more than 1% of the energy contained in the principal eigenfunction mode". Note that the above comments are consistent with the celebrated embedding results of Takens [176] and with the observation that the set of projections of a compact set of Hausdorff dimension k on to a $(2k+1)$-dimensional dimensional subspace is a residual set [177]. In spite of the finite (and possibly low) dimension of the attractor and the set containing it, the POD will generally have positive eigenvalues with eigenfunctions in the complementary subspace, unless the set is "flat" and entirely contained in the $(2k+1)$-dimensional linear subspace. As suggested by Eq. (A.23) and the example mentioned above, we can only expect this to hold probabilistically and in an asymptotic sense.

In connection with Takens's theorem, which is generally applied to the study of phase space reconstructions effected by delay maps, we note that delay maps are highly non-linear (as maps from "true" phase space into the embedding space). The POD spectrum is not invariant under nonlinear coordinate changes and one cannot expect the dimension in the delay map to be related to the number of non-zero POD eigenvalues in any simple way. Berkooz [178] has suggested an approach to this problem via a "conditional POD," but a discussion of this would take us too far afield.

The remark following Eq. (A.23) and (A.24) depends upon exexponential decay of empirical eigenvalues in the infinite tail. Is this a reasonable expectation? In the case of turbulent flows the answer appears to be yes both on physical (Tennekes and Lumley [135]) and on mathematical grounds (Promislow [179], Foias et al. [173]). From a physical viewpoint, exponential decay of the spectrum holds only in the far dissipative range, in which length scales are smaller than the Kolmogorov microscale. This should not be confused with the power-law decay of the intermediate inertial range. If asymptotic decay were substantially slower than exponential, high order spatial derivatives of the velocity field $\mathbf{u}(\mathbf{x},t)$ might not exist. Most fluid mechanicians believe this to be unreasonable in a description of continuum matter. The relevant mathematical concept is regularity of solutions, which describes the rate of decay of the tail of the spectrum of instantaneous solutions of a PDE in wavenumber space. To get a feel for this, consider the linear heat equation with a spatio-temporal "forcing function":

$$u_t = u_{xx} + f(x,t)\ ;\ \ u(x,0) = u_0(x).$$

Solution of this equation effectively requires one to integrate twice in space (and once in time), thereby smoothing the function $f(x,t)$, and the initial data $u_0(x)$. The effect is, of course, more marked the higher the spatial wavenumber. In the Navier-Stokes equation the dissipative term $\nu'\mathbf{u}$ plays a similar role to u_{xx}, its major influence also being in the far dissipative range. In the simplest fluid mechanical situation, where the domain is a rectangular box with periodic boundary conditions and the solutions may be expressed in

a (triple) Fourier series with time-dependent coefficients, Gevrey regularity of class s is the statement that the Fourier coefficients a_k decay at a rate such that the sum

$$\sum_k a_k e^{\tau|k|^2} e^{ik\cdot x}$$

converges for all τ. In this case the energy spectrum also decays exponentially fast at sufficiently high wavenumbers. In the context of turbulent flows this applies to the dissipation region of the spectrum. For an arbitrary (finite) domain one defines regularity in terms of the decay of the modal coefficients associated with the eigenfunctions of the Stokes operator in that domain. The asymptotics of the eigenvalues of the Stokes operator are the same for all "reasonable" domains [180], hence asymptotic results obtained from analysis of the periodic case remain valid. Rigorous regularity results for the Navier-Stokes equations in two- dimensional domains are given in [181]. In three dimensions there are no complete results, but if one assumes that vorticity is bounded above uniformly throughout the flow domain and in time, one can bypass the blow-up problem for solutions and obtain Gevrey regularity in this case too, possibly after solutions have evolved for some time [181]. Equipped with regularity of individual solutions, one still needs to show that the appropriate averages used in the POD are also uniformly exponentially bounded. This can be done [178] and the end result is that Gevrey regularity of solutions of the governing evolution equations implies exponential decay of the empirical eigenvalues. However, as remarked in [173], such exponential decay results apply only to the far dissipative range of turbulence and so are not directly relevant to the low-dimensional models of interest to us, in which we truncate far below that range. For more details see Berkooz [178]. For the sake of completeness we mention an interesting result due to Sirovich and Knight [182] which also concerns the structure of the POD at small spatial scales (high wavenumbers). Foias et al. [99] conclude from the results of [182] that, under certain conditions, the asymptotic form of the empirical eigenfunctions is that of Fourier modes. However, the results of Section (A.1) on the span of the eigenfunctions show that this cannot be true in full generality. Consider an ensemble of realisations that all vanish identically (or fall below experimental error) on a specific Part of the domain. The eigenfunctions themselves will also have to be zero on that part of the domain and so cannot be asymptotically close to Fourier modes in that region.

B DIRECTED PERCOLATION

CONTENTS

B.1 Directed Percolation at First Glance 115
B.2 Directed Percolation as a Stochastic Process 119
B.2.1 Basic Scaling Behavior 119
B.2.2 Universality and the DP Conjecture 120
B.2.3 Simple Mean-Field Approximation 121
B.2.4 Phenomenological Langevin Equation 122

The term *percolation* (from the Latin *percolare* = to filter) means to make a liquid to pass through fine interstices and is often used in the context of filtering[1]. A filter is usually made of a porous substance such as cloth, paper, sand or charcoal, through which a liquid may be passed to cleanse it of the solid or impure matter held in suspension. The retained material accumulates, clogging the pores so that the filter becomes impermeable after some time and needs to be replaced. Therefore, it is important to understand how the transition from percolation to congestion takes place, and we shall use a particular formulation of this problem as a paradigm for absorbing phase transitions.

B.1 DIRECTED PERCOLATION AT FIRST GLANCE

Various simple models for percolation have been introduced and intensively studied. In such models the pores of the filter are represented by the sites of a lattice. Neighbouring pores are connected by small channels which are represented by the bonds of the lattice that connect adjacent sites. In order to mimic irregularities in the network, each of these channels is randomly open with probability p or closed otherwise. An important question would be how the **percolation probability** p, which controls the microscopic connectivity of the channels, influences the macroscopic permeability of the filter.

It turns out that in a sufficiently large system there is a *phase transition* from a macroscopically permeable phase to another phase, where the filter becomes clogged so that the penetration depth is finite. This transition is continuous and takes place at a well-defined **critical threshold** p_c.

As in equilibrium statistical mechanics, the large-scale properties of percolation models close to the critical threshold turn out to be universal, i.e., they are determined by basic symmetries rather than microscopic details of the model. It is this universality which continues to fascinate theoretical physicists.

There are two fundamentally different versions of percolation. In *isotropic* (undirected) percolation, the agent can pass through open channels in any direction, while in *directed percolation* (DP) the water is restricted to flow along a preferred direction in space. For example, in a porous medium such a directed flow may be caused by a gravitational field, forcing the liquid to flow downwards. As shown in Fig. 56, the resulting clusters of wet sites are very different in both cases. Although both models exhibit percolation transitions,

1 The french word *percolateur*=coffee machine makes this even more explicit and, because of the direction imposed by the gravitational field, refers to directed, rather than isotropic, percolation.

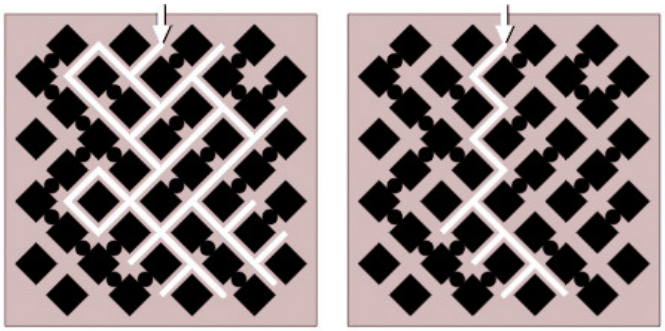

Figure 56: Bond percolation: The figures show a finite lattice in a particular configuration of open and closed bonds. Water is injected from above in the middle, as indicated by the arrows. Left panel: In the case of isotropic (=undirected) percolation the water percolates through open channels in any direction, leading to a certain cluster of wet sites. Right panel: In the case of directed percolation the water can only propagate downwards, leading to a much smaller and more elongated cluster.

they take place at different critical thresholds and are characterized by different universal properties.

The interpretation of DP as a stochastic process becomes possible by virtue of the strict order of cause and effect which allows one to interpret the preferred direction as a temporal coordinate. For example, in *bond directed percolation*, where bonds are randomly blocked, we may enumerate horizontal rows by a temporal index t, commonly referred to as "time", as shown in Fig. 57[2]. Knowing the configuration of wet sites at time t we can compute the next configuration at time $t + 1$ by means of simple probabilistic rules. The same applies to site directed percolation, where sites instead of bonds are randomly blocked[3].

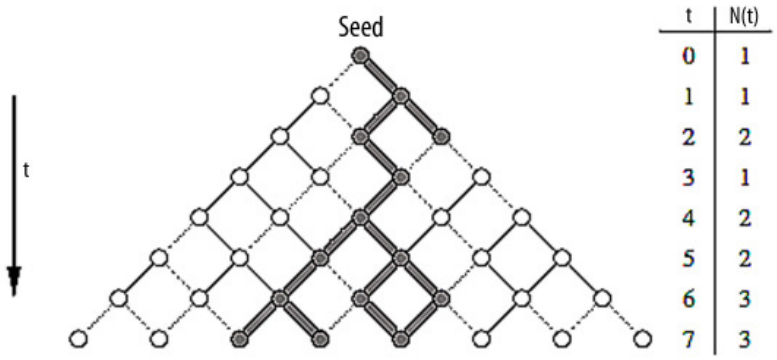

Figure 57: Bond directed percolation as a stochastic process evolving in time. The process shown here starts with a single wet site at the origin. It then evolves through a sequence of configurations along horizontal lines enumerated by a temporal index t. An important quantity to study is the number $N(t)$ of wet sites at time t.

2 It is common to refer to a lattice with d directions perpendicular to the single "time" direction as "$(d+1)$-*dimensional*".

3 In site percolation, the sites of a lattice are occupied with probability p and the occupied sites are linked by nearest-neighbour bonds to form clusters. In bond percolation, all sites are occupied and bonds are drawn between nearest-neighbour sites with probability p.

Interpreting wet (active) sites as particles A and dry (inactive) sites as vacancies $\emptyset$ these probabilistic rules can be regarded as update rules of a *reaction-diffusion process*. For example, if both channels to the nearest neighbours at time $t+1$ are blocked, the trajectory of the particle terminates, meaning that the particle disappears by a death process $A \to \emptyset$. If only one channel is open the particle effectively diffuses to the left or right with equal probability. Finally, if both channels are open the particle duplicates creating an offspring, *i.e.*, it undergoes the reaction $A \to 2A$. However, each site can be occupied by at most one particle. Therefore, if two particles happen to reach the same site, they merge to a single one by a coalescence process $2A \to A$. Therefore, DP can be interpreted as a reaction-diffusion process which involves:

- particle removal (death) $\quad A \to \emptyset$
- offspring production $\quad A \to 2A$
- coalescence $\quad 2A \to A$

combined with single-particle diffusion, as demonstrated in Fig. 58. As will be discussed below, any stochastic particle process that effectively follows this reaction-diffusion scheme belongs generically to the universality class of DP.

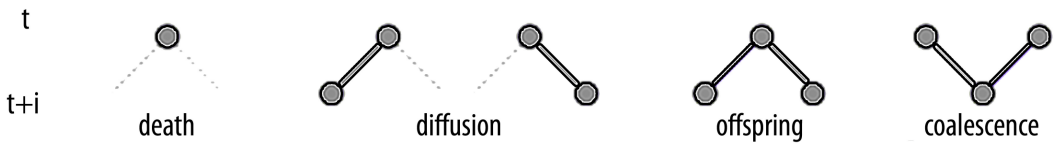

Figure 58: Interpretation of bond directed percolation as a reaction-diffusion process of interacting particles.

Using this dynamical interpretation it is straightforward to generate explicit realizations of DP-clusters on a computer. To this end one simply iterates over all active sites at time t and activates their nearest neighbours at time $t+1$ independently with probability p. If p is small, the generated clusters have the shape of a finite droplet, as shown in the left panel of Fig. 59. On the other hand, if p is sufficiently large, activity may spread over the entire system within a cone-like region in space-time, generating an infinite cluster of active sites (see right panel of 59). However, even for large values of p it may happen that some of these clusters die out at an early stage.

By analyzing the cluster sizes statistically one observes the following phenomenology: Below a certain well-defined threshold $p < p_c$ all generated clusters remain finite, while for $p > p_c$ some of the clusters spread infinitely over the entire system. These two phases are separated by a sharp transition point at a specific critical threshold $p = p_c$ which in the case of bond DP in one space dimension is close to $p = 0.6447$. At this value finite clusters of all sizes are generated. A possible explanation is that the large-scale properties of critical clusters are universal, *i.e.*, they do not depend on the microscopic details of the model under consideration.

It is interesting to study the average number of active particles $\langle N(t) \rangle$. The result is shown in Fig. 60. Below the critical threshold the average number of particles $\langle N(t) \rangle$ increases until it crosses over to an exponential decay. Above the critical point the increase accelerates until it crosses over to a linear increase. Precisely at the critical point $p = p_c$ the corresponding curve in the plot appears to be straight, indicating a power-law behaviour. In fact, it is found that $\langle N(t) \rangle$ measured at criticality increases for large t as t^{Θ}, where the exponent $\Theta \sim 0.302$ is just the slope of the straight line in the plot. For small t, however, especially during

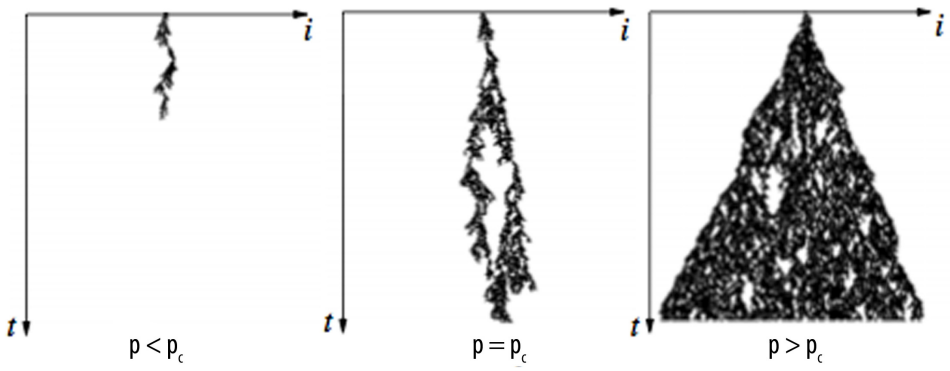

Figure 59: Typical DP clusters grown from a single seed in 1+1 dimensions.

the first few time steps, we observe deviations from the anticipated power-law behaviour. These so-called initial transients are caused by the discrete lattice structure and depend on non-universal details of the model. The asymptotic notation

$$\langle N(t) \rangle \sim t^{\Theta} \tag{B.1}$$

intentionally ignores such initial transients as well as the model-dependent proportionality constant and thus allows one to concentrate on the interesting universal behaviour valid in the limit of large t and for large system sizes. The exponent Θ, however, is the same in all DP models, *i.e.*, it is universal with respect to microscopic details of the model.

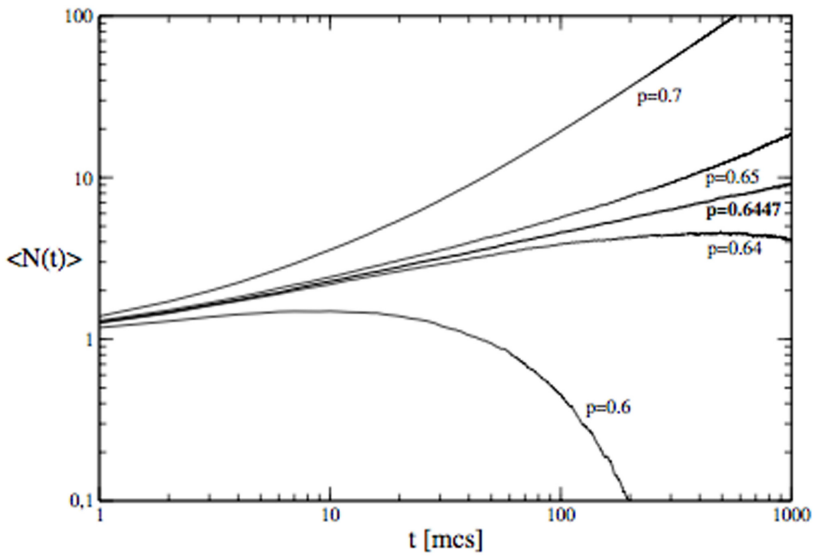

Figure 60: Average number of particles $\langle N(t) \rangle$ as a function of time t (measured in units of Monte Carlo steps) for various percolation probabilities p.

B.2 DIRECTED PERCOLATION AS A STOCHASTIC PROCESS

B.2.1 Basic Scaling Behavior

DP can be interpreted as a stochastic process of diffusing particles which react as $A \to \emptyset$, $A \to 2A$. In addition, each site can be occupied by at most one particle, effectively introducing a coalescence process $2A \to A$. On a descriptive level the DP phase transition may be thought of as being caused by a competition of spontaneous reproduction and self-annihilation of particles. If the rate for offspring production A?2A is sufficiently large, the (infinite) system is able to maintain a fluctuating active state characterized by a non-vanishing stationary particle density $\rho > 0$. Contrarily, if the dynamics is dominated by death processes the system approaches a configuration without particles.

Such a configuration, from where the system cannot escape, is called *absorbing*. More specifically, an absorbing state is a configuration (or a set of several configurations) that can be reached by the dynamics but not be left by them. Obviously such absorbing states cannot obey detailed balance with any other active state, hence the system is by definition out of thermal equilibrium. Therefore, DP is said to display a *non-equilibrium phase transition* from a fluctuating phase into an absorbing state or, more concisely, *an absorbing phase transition*.

As in equilibrium statistical mechanics, it turns out that continuous phase transitions in systems out of equilibrium can be grouped into universality classes which are associated with certain critical exponents. Absorbing phase transitions are characterized by at least three independent critical exponents[4] β, $\nu_\perp$, and $\nu_\parallel$. The exponent β describes how the stationary density of particles in the active phase of an infinitely large system scales close to criticality, *i.e.*:

$$\rho \sim (p - p_c)^\beta. \tag{B.2}$$

Here p is the percolation probability that controls the effective rate for offspring production, while p_c denotes its critical value where the transition takes place. Such a stationary state is characterized by a *correlation length* $\xi_\perp$ and a *correlation time* $\xi_\parallel$. They both diverge close to criticality as

$$\xi_\perp \sim (p - p_c)^{-\nu_\perp}, \quad \xi_\parallel \sim (p - p_c)^{-\nu_\parallel}. \tag{B.3}$$

Since there is no symmetry between space and time, the two exponents $\nu_\perp$ and $\nu_\parallel$ are generally different. In contrast to equilibrium statistical mechanics, stochastic models involve time as an independent degree of freedom on equal footing with the spatial degrees of freedom, allowing one to study dynamical properties such as relaxation phenomena. This requires one to specify an initial state. For example, starting with a fully occupied lattice at the transition $p = p_c$, the density of particles (active sites) decays algebraically as

$$\rho(t) \sim t^{-\alpha} \tag{B.4}$$

where $\alpha = \beta/\nu_\parallel$. Similarly, the spatial correlation length grows as

$$\xi_\perp(t) \sim t^{1/z}, \tag{B.5}$$

where $z = \nu_\parallel/\nu_\perp$ is known as: dynamical exponent.

In finite systems one observes deviations from these asymptotic power laws. For example, on a finite lattice there is always a non-vanishing probability of reaching the absorbing

4 There are actually two exponents β and β', meaning that absorbing phase transitions are generally described by four independent critical exponents. In the case of DP these two exponents coincide because of a special symmetry under time-reversal. See the book "*Non-Equilibrium Phase Transitions Volume* I*: Absorbing Phase Transitions*".

configuration. Typically this leads to a breakdown of the power laws B.4 and B.5 when the correlation length $\xi_\perp$ becomes comparable with the lateral size of the system. Generally such *finite-size effects* set in after a typical time that grows with the system size. For example, if L is the lateral size of the system (so that $N \propto L^d$ is the total number of sites), the absorbing state is reached at a characteristic time t_f that scales as $tf \sim L^z$.

B.2.2 Universality and the DP Conjecture

As mentioned before there are a large variety of models which exhibit a DP phase transition. This means that the term "directed percolation" does not refer to a particular model; rather it stands for a whole universality class of models which display the same type of transition, characterized by a certain set of critical exponents and scaling functions. The DP class comprises diverse types of systems, including models for epidemic spreading, forest fires, catalytic reactions, synchronization of maps, and surface growth, to name only a few. In order to delineate this range of models, Janssen and Grass-berger formulated their celebrated *DP-conjecture*. According to this conjecture, it is thought that a given model should generically belong to the DP universality class if

1. the model displays a continuous phase transition from a *fluctuating* active phase into a *unique* absorbing state,
2. the transition is characterized by a non-negative one-component order parameter,
3. the dynamic rules are short-ranged,
4. the system has no special attributes such as unconventional symmetries, conservation laws, or quenched randomness.

Apart from multicritical extensions of directed percolation (*e.g.* tricritical directed percolation) which violate the above hypothesis in the strict sense, no counterexamples have been found so far. In fact, the DP class seems to be even more general as it has been identified in models that violate some of the four conditions, for example in certain models with several or fluctuating absorbing states or even in spreading processes with several particle species and multicomponent order parameters. This means that the DP universality class is extremely robust.

In contrast to well-known equilibrium universality classes such as the 2D *Ising model*, even in $1+1$ dimensions DP has not yet been solved exactly. Despite its simplicity and robustness all attempts to compute the critical exponents exactly have failed so far. In fact, numerical estimates suggest that the values of the critical exponents might turn out to be irrational numbers, rather than the simple rational values found in 2D integrable systems at equilibrium.

B.2.3 Simple Mean-Field Approximation

Most models that belong to the DP universality class can be interpreted directly as a stochastic particle processes. Let us now introduce effective reaction rates (probabilities per unit time) μ_r, μ_p, and μ_c for particle removal, offspring production, and coalescence:

- $A \to 2A$ with rate μ_p
- $A \to \emptyset$ with rate μ_r
- $2A \to A$ with rate μ_c

Starting with such an effective reaction-diffusion scheme, it is straightforward to set up a simple mean-field approximation in terms of the mean particle density $\rho(t)$, which neglects any spatial information. In this approximation the unary reactions $A \to 2A$ and $A \to \emptyset$ correspond to a linear term for particle gain and loss while the binary coalescence process $2A \to A$ gives rise to a quadratic loss term, leading to the mean-field equation

$$\frac{\partial}{\partial t}\rho(t) = \tau\rho(t) - g\rho(t)^2. \tag{B.6}$$

Here we introduced the control parameter $\tau = \mu_p - \mu_r$ which, as we shall see below, is proportional to the distance from the critical point. Moreover has been used the abbreviation $g = \mu_c$ since in a field-theoretic context this parameter will play the role of a coupling constant.

In the asymptotic limit of large t the solution of the mean-field equation is given to leading order by

$$\rho(t) \simeq \begin{cases} -\tau\left(g - \frac{\tau}{\rho_0}\right)^{-1} e^{\tau t} & \xrightarrow{t\to\infty} 0 \quad \text{if } \tau < 0 \\ (\rho_0^{-1} + gt)^{-1} & \xrightarrow{t\to\infty} 0 \quad \text{if } \tau = 0 \\ \frac{\tau}{g} + \frac{\tau}{g^2}\left(g - \frac{\tau}{\rho_0}\right) e^{-\tau t} & \xrightarrow{t\to\infty} 0 \quad \text{if } \tau > 0, \end{cases} \tag{B.7}$$

where ρ_0 denotes the initial density at $t = 0$. Obviously the steady-state solution $\rho = 0$ corresponds to the absorbing state. For $\tau > 0$ the solution approaches a steady-state with a non-vanishing stationary density of active sites $\rho = \tau/g$ while for $\tau = 0$ one obtains an algebraic decay. Therefore, within mean-field theory the transition takes place at the critical threshold $\tau_c = 0$. Comparing these results with B.2 and B.7 one obtains the mean-field exponents $\beta_{MF} = 1$ and $\alpha_{MF} = 1$, respectively.

In order to obtain the third independent exponent, one has to include an additional term in the mean-field equation which provides spatial information. Since in DP active sites create offspring at nearest neighbours, the particles are subject to an effective diffuse motion. This can be accounted for by adding a term for diffusion in the mean-field equation

$$\frac{\partial}{\partial t}\rho(t, \mathbf{r}) = \tau\rho(t, \mathbf{r}) - g\rho(t, \mathbf{r})^2 + D\nabla^2\rho(t, \mathbf{r}), \tag{B.8}$$

where D is the diffusion constant. Inserting the scaling ansatz $\rho(t, \mathbf{r}) = (gt)^{?1} f(\mathbf{r}/t^{1/z})$, where $z = \nu_\parallel/\nu_\perp$ is the dynamical critical exponent, one obtains a consistent differential equation for f only if $z_{MF} = 2$. Therefore, the mean-field exponents of directed percolation are given by

$$\beta_{MF} = 1, \quad \nu_{\perp,MF} = 1/2, \quad \nu_{\parallel,MF} = 1. \tag{B.9}$$

B.2.4 Phenomenological Langevin Equation

The mean-field exponents are expected to be valid in sufficiently high space dimensions, where diffusive mixing is strong enough to suppress correlations. As we shall see now, the mean-field approximation is actually valid in space dimensions above the *upper critical dimension* $d_c = 4$. To see this let us consider the *phenomenological stochastic Langevin equation* for DP which accounts for fluctuation effects on a coarse-grained level. This Langevin equation can be derived rigorously from the master equation of the contact process and looks like the mean-field equation B.8 extended by a suitable noise term:

$$\frac{\partial}{\partial t}\rho(t,\mathbf{r}) = \tau\rho(t,\mathbf{r}) - g\rho(t,\mathbf{r})^2 + D\nabla^2\rho(t,\mathbf{r}) + \eta(t,\mathbf{r}). \tag{B.10}$$

Here $\eta(t,\mathbf{r})$ stands for a density-dependent Gaussian noise field with the correlations:

$$\langle\eta(t,\mathbf{r})\rangle = 0, \tag{B.11}$$

$$\langle\eta(t,\mathbf{r})\eta(t',\mathbf{r}')\rangle = k\rho(t,\mathbf{r})\delta(t-t')\delta^d(\mathbf{r}-\mathbf{r}') \tag{B.12}$$

where k controls the global noise amplitude. Note that the density appears on the right-hand side of the correlator, meaning that the amplitude of the noise is effectively proportional to $\sqrt{\rho(t,\mathbf{r})}$. This ensures that the absorbing state $\rho(t,\mathbf{r}) = 0$ does not fluctuate. The square-root behaviour is related to the fact that the noise describes *density fluctuations* on a coarse-grained scale, which can be viewed as the sum of individual noise contributions generated by each particle averaged over some mesoscopic box size. According to the *central limit theorem*, the distribution of the sum $\eta = \sum_{i=1}^{N}\eta_i$ of N identically distributed random variables η_i (such that their average and variance are both finite) tends in the limit $N \to \infty$ to a Gaussian. Hence one expects $\eta(t,\mathbf{r})$ to be drawn from a Gaussian distribution with an amplitude proportional to the square root of the number of active sites in the box.

By a dimensional analysis of the Langevin equation, one observes that the noise is irrelevant in $d > 4$, marginal in $d = 4$, and relevant in $d < 4$ dimensions. This means that $d_c = 4$ is the upper critical dimension of directed percolation above which the mean-field exponents are correct. Below d_c fluctuation effects become relevant and the exponents have to be determined by a renormalisation group study of the corresponding field theory.

We note that eq. B.10 is the minimal Langevin equation needed to describe DP. It may also include higher order terms such as $\rho^3(t,\mathbf{r})$, $\nabla^4\rho(t,\mathbf{r})$, or higher-order contributions of the noise. The irrelevance of such higher-order terms can be understood from the renormalisation group (RG), (not explained here see the book "*Non-Equilibrium Phase Transitions Volume I: Absorbing Phase Transitions*" for further informations), and is the origin of universality in DP. Furthermore we note that Langevin equations for systems with absorbing states are difficult to iterate numerically, the most efficient method was proposed by Dornic et al. in 2005 in the paper *Phys. Rev. Lett., 94:100601*.

BIBLIOGRAPHY

[1] W. Zwetkoff, *Acta Physicochim*, URSS **16**, 132 (1942). (Cited on page 5.)

[2] D. McLemore and E. F. Carr, *J. Chem. Phys.* **57**,3245 (1972);
F. Rondelez, *Sol. State Comm.* **11**, 1675 (1972);
W. Flint and E. F. Carr, *Mol. Cryst. and Liquid Cryst.* **22**, 1 (1973). (Cited on pages 5, 21, and 22.)

[3] L. M. Blinov, *Sov. Phys. Usp.* **17**, 658 (1975). (Cited on pages 6, 7, and 9.)

[4] I. Björnstahl, *Ann. d. Phys.* **56**, 161 (1918). (Cited on page 8.)

[5] G. Friedel, *Ann. d. Phys.* **19**, 273 (1922);
H. Zocher and V. Birstein, *Zs. Phys. Chem.* **A142**, 186 (1929);
M. Jezewski, *Zs. Phys.* **51**, 159 (1928);
W. Kast, *Zs. Kristallogr.* **79**, 146 (1931). (Cited on page 8.)

[6] V. K. Freedericksz and V. N. Tsvetkov, *Dokl. Akad. Nauk SSSR 9* **4**, 123 (1935);
V. K. Freedericksz and V. N. Tsvetkov, *Acta Physicochim. URSS* **3**, 880 (1935);
V. N. Tsvetkov, *Uch zap. Leningr. ped. in-ta 10* **5**, (1938);
W. N. Zwetkoff, *Acta Physicochim. URSS* **6**, 885 (1937). (Cited on pages 8 and 22.)

[7] L. K. Visitin' and A. P. Kasputin, *Optika i Spektroskopya* **24**, 1255 (1973). (Cited on page 8.)

[8] G. H. Heilmeier, L. A. Zanoni and L. A. Barton, *Proc. IEEE* **56**, 1162 (1968);
G. H. Heilmeier, L. A. Zanoni and L. A. Barton, *IEEE Trans. Electron Dev.* **ED-17**, 22 (1970). (Cited on page 8.)

[9] F . C. Frank, *Disc. Farad. Soc.* **25**, 19 (1958). (Cited on page 9.)

[10] H. Gruler, T. J. Scheffer, and G. Meier, *Zs. Naturforsch.* **27a**, 966 (1972). (Cited on pages 9 and 10.)

[11] P. D. Berezin, I. N. Kompanets, V. V. Nikitin, and S. A. Pikin, *Eksp. Teor. Fiz.* **64**, 599 (1972). (Cited on pages 9 and 10.)

[12] M. F. Schiekel and K. Fahrenschon, *Appl. Phys. Lett.* **19**, 391 (1971);
R. A. Soref and M. J. Rafuse, *Appl. Phys.* **43**, 2029 (1971). (Cited on page 9.)

[13] C. Mauguin, *Bull. Soc. franc, miner.* **34**, 71 (1911). (Cited on page 9.)

[14] H. J. Deuling, *Mol. Cryst. and Liquid Cryst.* **19**, 123 (1972). (Cited on pages 9 and 10.)

[15] A. Saupe, *Zs. Naturforsch.* **15a**, 815 (1960);
P. Pincus, *J. Appl. Phys.* **41**, 974 (1970). (Cited on page 9.)

[16] F. M. Leslie, *Mol. Cryst. and Liquid Cryst.* **12**, 57 (1970). (Cited on page 10.)

[17] H. Gruler, *Zs. Naturforsch.* **28a**, 474 (1974). (Cited on page 10.)

[18] E. Jakeman and E. P. Raynes, *Phys. Lett.* **A39**, 69 (1972);
Orsay Liquid Crystal Group, *J. Chem. Phys.* **51**, 816 (1969). (Cited on page 10.)

[19] D. McLemore and E. F. Carr, *J. Chem. Phys.* **57**, 3245 (1972);
F. Rondelez, *Sol. State Comm.* **11**, 1675 (1972);
W. Flint and E. F. Carr, *Mol. Cryst. and Liquid Cryst.* **22**, 1 (1973). (Cited on pages 21 and 24.)

[20] W. H. de Jeu and C. J. Gerritsma, *J. Chem. Phys.* **56**, 4752 (1972);
W. H.de Jeu, C. J. Gerritsma, P. Van Zanten, and W. J. A. Goossens, *Phys. Lett.* **A39**, 355 (1972). (Cited on page 22.)

[21] M.F.Grebenkin, G.S.Chilaya,V.T.Lazareva,K.V. Roitman, L. M.Blinov, and V. V. Titov, *Collected papers of the 2nd Ail-Union Scientific Conference on Liquid Crystals (Ivanovo, June 27-29, 1972), IK AN SSSR-IGPI, Ivanovo*, **179** (1973). (Cited on page 22.)

[22] W. H.deJeu,C.J.Gerritsma, and A.M.VanBoxtel, *Phys. Lett.* **34**, 203 (1971). (Cited on page 22.)

[23] S. A. Pikin, *Zh. Eksp. Teor. Fiz.* **60**, 1185 (1971);
S. A. Pikin and A. A. Shtol'berg, *Kristallografiya* **18**, 445 (1973). (Cited on pages 22, 23, and 24.)

[24] P. A. Penz and G. W. Ford, *Phys. Rev*, **A6**, 414, 1 1676 (1972);
P . A. Penz, *4th Intern. Conference on Liquid Crystals, Kent, USA*, **Rept. No. 108**, 1972. (Cited on pages 22 and 24.)

[25] W. Helfrich, *ibid.* **51**, 4092 (1969). (Cited on pages 22, 23, and 24.)

[26] R. Williams, *J. Chem. Phys.* **39**, 384 (1963);
A. P. Kapustin and L. S. Larionova, *Kristallografiya* **9**, 297 (1964):
L. K. Vistin' and A. P. Kapustin, *Kristallografiya* **14**, 741 (1969). (Cited on pages 22 and 26.)

[27] M. Bertolotti, S. Lagomarsino, F . Scudieri, and D. Sette, J. Phys. **C6**, L177 (1973). (Cited on page 22.)

[28] P . A. Penz, *Phys. Rev. Lett.* **24**, 1405 (1970). (Cited on page 22.)

[29] Orsay Liquid Crystal Group, *Phys. Rev. Lett.* **25**, 1642 (1970);
E. Dubois-Violette, P . G. de Gennes, and O. Parodi, *J. de Phys.* **32**, 305 (1971). (Cited on pages 23, 24, and 26.)

[30] P. G. de Gennes, *Comm. Sol. State Phys.* **3**, 35 (1968). (Cited on page 23.)

[31] F. M. Leslie, *Quart. J. Mech. and Appl. Math.* **19**, 357 (1966). (Cited on page 24.)

[32] S. A. Pikin, *Zh. Eksp. Teor. Fiz.* **61**, 2133 (1971). (Cited on page 24.)

[33] C. W. Garland, G. B. Kasting, and K. J. Lushington, *Phys. Rev. Lett.* **43**, 1420 (1979). (Cited on page 25.)

[34] G. B. Kasting, C. W. Garland, and K. J. Lushington, *Phys. (Paris)*, **41**, 879 (1980). (Cited on page 25.)

[35] W. Helfrich, *J. Che. Phys.*, **51**, 4092 (1969). (Cited on page 26.)

[36] P. G. de Gennes, *The Physics of Liquid Crystals*, Oxford, Clarendon (1982). (Cited on pages 25, 26, 31, 52, 57, 63, and 91.)

[37] C. Hilsum and F. C. Saunders, *Mol. Cryst. Liq. Cryst.*, **64**, 25 (1980). (Cited on page 26.)

[38] K. Hirakawa and S. Kai, *Mol. Cryst. Liq. Cryst.*, **40**, 261 (1977). (Cited on page 26.)

[39] S. Kai and K. Hirakawa, *Solid State Commun.*, **18**, 1579 (1976). (Cited on pages 26 and 31.)

[40] E. Bodenshatz, W Zimmerman and L. Kramer, *J. de Phys.*, **49**, 1875 (1988). (Cited on page 26.)

[41] W. Zimmerman and L. Kramer, *Phys. Rew. Lett.*, **55**, 402 (1985). (Cited on pages 26, 27, and 28.)

[42] W. Thom, W. Zimmerman and L. Kramer, *Liquid Crystals*, **18**, 5 (1989). (Cited on pages 26, 27, and 28.)

[43] L. Cesari, *Asymtotic Beahviour and Stabiliti Problem in Ordinary Differential Equations*, Springer, Berlin (1971). (Cited on page 27.)

[44] M. R. E. Proctor and C. A. Jones, *J. Fluid. Mech.*, **188**, 301 (1988). (Cited on page 28.)

[45] H. W. de Jeu and J. van der Veen, *Phys. Lett.*, **A44**, 277 (1973). (Cited on page 29.)

[46] T. Wilson, A.R. Carlini, *J. Microsc.*, **141**, 56 (1988). (Cited on pages 44 and 49.)

[47] G. Guilbault, *Practical Fluorescence, 2nd Ed.*, Marcel Dekker, Inc., New York (1990). (Cited on page 44.)

[48] P. Atkins, *Physical Chemistry, 5th Ed.*, W. H. Freeman and Company, New York (1994). (Cited on pages 44 and 49.)

[49] R. Y. Tsien, A. Waggoner, *Handbook of Biological Confocal Microscopy, 2nd Ed.*, Plenum Press, New York (1995). (Cited on pages 44, 48, and 49.)

[50] M. Minsky, *Scanning*, **141**, 128 (1988). (Cited on pages 45 and 46.)

[51] C.J.R. Sheppard, D.M. Shotton, *Confocal Laser Scanning Microscopy*, Springer, New York (1997). (Cited on pages 46 and 49.)

[52] T. Porter, T. Duff, *Comput. Graphics*, **18 (3)**, 253 (184). (Cited on page 47.)

[53] S. Inoué, K.R. Spring, *Video Microscopy the Fundamentals*, Plenum Press, New York (1997). (Cited on page 48.)

[54] P.L. Becker, *Fluorescence Imaging Spectroscopy and Microscopy*, John Wiley & Sons, Inc.,New York (1996). (Cited on pages 49 and 50.)

[55] L. Song, C.A. Varma, J.W. Verhoeven, *Biophys. J.*, **70**, 2959 (1996). (Cited on page 49.)

[56] D. Axelrod, D.E. Koppel, *Biophys. J.*, **16**, 1055 (1976). (Cited on page 50.)

[57] G. Strangi, S. Ferjani, V. Barna, A. De Luca, C. Versace, N. Scaramuzza, and R. Bartolino, *Opt. Exp.*, **14**, 7737 (2006). (Cited on page 50.)

[58] S. Ferjani, L. S. Valvo, A. De Luca, V. Barna, R. De Marco, and G. Strangi, *Phys. Rev. E*, **78**, 011707 (2008). (Cited on page 50.)

[59] S. V. Shiyanovskii, I. I. Smalyukh, O. D. Lavrentovich, *Computer simulations and fluorescence confocal polarizing microscopy of structures in cholesteric liquid crystals*, Kluwer Academic Publishers, The Netherlands (2001). (Cited on page 50.)

[60] I. I. Smalyukh, R. Pratiba, N. V. Madhustudana, O. D. Lavrentovich, *Euro. Phys. J. E*, **16**, 179 (2005). (Cited on page 50.)

[61] E. Dubois-Violette, P. G. de Gennes and O. Parodi, *J. Physique*, **32**, 305 (1971).

[62] W. Zimmermann and L. Kramer, *Phys. Rev. Lett.*, **55**, 402 (1985).

[63] A. Joets and R. Ribotta, *J. Physique*, **47**, 595 (1986). (Cited on pages 34, 74, 75, 80, and 81.)

[64] R. Ribotta and A. Joets, *Phys. Rev. Lett.*, **56**, 1595 (1986). (Cited on page 74.)

[65] E. Bodenschatz, W. Zimmermann and L. Kramer, *J. Phys. France*, **49**, 1875 (1988).

[66] N. Gheorghiu, I.I. Smalyukh, O.D. Larentovich and J.T. Gleeson, *Phys. Rev. E*, **74**, 041702 (2006).

[67] S. Kai, K. Yamaguchi and K. Hirakawa, *Jpn. J. Appl. Phys.*, **14**, 1653 (1975).

[68] G. Paladin and A. Vulpiani, *Phys. Rep.*, **156**, 147 (1987). (Cited on pages 52 and 54.)

[69] H.E. Stanley and P. Nelkin, *Nature*, **335**, 405 (1988). (Cited on pages 52 and 54.)

[70] R.A. Antonia, E.J. Hopfinger, Y. Gagne and E Anselmet, *Phys. Rev. A*, **30**, 2704 (1984). (Cited on page 51.)

[71] R.R. Prasad, C. Meneveau and K.R. Sreenivasan, *Phys. Rev. Lett.*, **61**, 74 (1988). (Cited on pages 51 and 52.)

[72] R.R. Prasad and K.R. Sreenivasan, *J. Fluid Mech.*, **216**, 1 (1990). (Cited on pages 51 and 52.)

[73] H. Homann, J. Bec, H. Fichtner and R. Grauer, *Phys. Plasmas*, **16**, 082308 (2009). (Cited on page 51.)

[74] K.R. Sreenivasan and C. Meneveau, *Phys. Rev. A*, **38**, 6287 (1988). (Cited on pages 51 and 52.)

[75] V. Carbone, C. Versace and N. Scaramuzza, *Physica D*, **106**, 314 (1997). (Cited on pages 50, 52, and 63.)

[76] A. S. Monin and A. M. Yaglom, *Statistical Fluid Mechanics: Mechanics of Turbulence*, Dover, New York (2007). (Cited on pages 51, 57, 79, 80, 81, and 82.)

[77] W. D. McComb, *The physics of fluid turbulence*, Oxford Univ. Press, New York (1990). (Cited on pages 80 and 81.)

[78] U. Frisch, *Turbulence: the legacy of A.N. Kolmogorov*, Cambridge Univ. Press, Cambridge UK (1995). (Cited on pages 14, 57, 62, and 64.)

[79] K. R. Sreenivasan, *J. Fluid Mech.*, **151**, 81 (1985). (Cited on page 57.)

[80] K. R. Sreenivasan and R. A. Antonia, *Ann. Rev. Fluid Mech.*, **29**, 435 (1997).

[81] F. Anselmet et al., *J. Fluid Mech.*, **140**, 63 (1984).

[82] A. Arneodo et al., *Europhys. Lett.*, **34**, 411 (1996). (Cited on page 57.)

[83] A. Vincent and M. Meneguzzi, *J. Fluid Mech.*, **225**, 1 (1991). (Cited on page 57.)

[84] O. N. Boratav and R.B. Pelz, *Phys. Fluids*, **9**, 1400 (1997). (Cited on page 57.)

[85] R. Bruno and V. Carbone, *Liv. Rev. Sol. Phys.*, **2**, 4 (2005). (Cited on page 57.)

[86] L. Burlaga, *J. Geophys. Res.*, **96**, 5847 (1991).

[87] E. Marsch and C.-Y. Tu, *Nlin. Proc. Geophys.*, **4**, 101 (1997). (Cited on page 57.)

[88] G. Strangi, S. Ferjani, V. Barna, A. De Luca, C. Versace, N. Scaramuzza, and R. Bartolino, *Opt. Exp.* **14**, 7737 (2006). s

[89] S. V. Shiyanovskii, I. I. Smalyukh, O. D. Lavrentovich, *Computer simulations and fluorescence confocal polarizing microscopy of structures in cholesteric liquid crystals*, Kluwer Academic Publishers: The Netherlands (2001). (Cited on page 91.)

[90] I. I. Smalyukh, R. Pratiba, N. V. Madhustudana, O. D. Lavrentovich, *Euro. Phys. J. E*, **16**, 179 (2005).

[91] V. Carbone, *Phys. Rev. Lett.*, **71**, 1546 (1993).

[92] H. Politano, A. Pouquet, and V. Carbone, *Europhys. Lett.*, **43**, 516 (1998). (Cited on page 57.)

[93] R. Camussi et al., *Phys. Fluids*, **8**, 1181 (1996). (Cited on page 57.)

[94] A. Noullez et al., *J. Fluid Mech.*, **339**, 287 (1997). (Cited on page 57.)

[95] B. Protas, S. Goujon-Durand and J. E. Wesfreid, *Phys. Rev. E*, **55**, 4165 (1997).

[96] E. Gaudin et al., *Phys. Rev. E*, **57**, R90 (1997).

[97] L. M. Blinov, *Electro-Optical and Magneto-Optical properties of Liquid Crystals*, Wiley, New York (1983). (Cited on page 57.)

[98] F. Carbone et al., *Europhys. Lett.*, **89**, 46004 (2010). (Cited on pages 52, 57, and 63.)

[99] S. Kai, M. Andoh and S. Yamaguchi, *Phys. Rev. A*, **46**, R7375 (1992). (Cited on pages 63 and 64.)

[100] S. Kai and W. Zimmermann, *Phys. Rev. A*, **46**, 4954 (1992). (Cited on page 75.)

[101] B. Castaing, Y. Gagne, and V. Hopfinger, *Physica D*, **46**, 177 (1990). (Cited on page 75.)

[102] E. Marsch, and C.-Y. Tu, *Ann. Geophys.*, **12**, 1127 (1994). (Cited on page 62.)

[103] Sorriso-Valvo L. et al., *Geophys. Res. Lett.*, **26**, 1804 (1999). (Cited on page 62.)

[104] Sorriso-Valvo L. et al., *Europhys. Lett.*, **51**, 520 (2000). (Cited on page 62.)

[105] Sorriso-Valvo L. et al., *Plan. Space Sci.*, **49**, 1193 (2001). (Cited on page 62.)

[106] L. Sorriso-Valvo, V. Carbone and R. Bruno, *Europhys. Lett.*, **67**, 504 (2004).

[107] Carbone V. et al., Riv. Nuovo Cimento, **27**, 1 (2005).

[108] M. Farge, *Ann. Rev. Fluid Mech.*, **24**, 395 (1992). (Cited on page 62.)

[109] R. Benzi et al., *Phys. Rev.* E **48**, 29 (1984).

[110] R. Benzi et al., *Physica D* **96**, 162 (1996).

[111] G. Amati, R. Benzi and S. Succi, *Phys. Rev. E*, **55**, 6985 (1997).

[112] V. Carbone, R. Bruno and P. Veltri, *Geophys. Res. Lett.*, **23**, 121 (1996).

[113] V. Carbone et al., *Phys.Rev. E*, **62**, 49 (2000).

[114] G. Ruiz, qui. Chavarria, C. Baudet and S. Ciliberto, *Europhys. Lett.*, **32**, 319 (1995).

[115] R. Bruno et al., *Phys. Plasmas*, **14**, 032901 (2007).

[116] J. L. Lumley, *The structure of inhomogeneous turbulence. In A. M. Yaglom and V. I. Tatarski, editors, Atmospheric turbulence and wave propagation*, **166–178**, Nakua, Moscow (1967). (Cited on page 69.)

[117] A. Papoulis, *Probability, Random Variables, and Stochastic processes*, McGraw-Hill, New York (1965). (Cited on page 69.)

[118] A. Rosenfeld, A. C. Kak, *Digital Picture Processing*, Academic Press, New York (1982). (Cited on page 69.)

[119] V. R. Algazi, D. J. Sakrison, *On the optimality of the Karhunen-Loéve expansion*, IEEE Trans. Inform. Theory, **15:319–321** (1969). (Cited on page 69.)

[120] C. A. Andrews, J. M. Davies, G. R. Schwartz, *Adaptive data compression*, Proc. IEEE, **55:267–277** (1967). (Cited on page 69.)

[121] D. H. Gay, W. H. Ray, *Identification and control of linear distributed parameter systems through the use of experimentally determined singular functions*, Proc. IFAC Symp. Control of Distributed Parameter Systems, **173–179**, Los Angeles (1986). (Cited on page 69.)

[122] D. H. Gay, W. H. Ray, *Application of singular value methods for identification and model based control of distributed parameter systems*, Proc. IFAC Workshop on Model Based Process Control, **95–102**, Atlanta (1988). (Cited on page 69.)

[123] R. W. Preisendorfer, *Principal component analysis in meteorology and oceanography*, Elsevier, Amsterdam (1988). (Cited on page 69.)

[124] P. Holmes, *Turbulence, Coherent Structures, Dynamical Systems and Symmetry*, Cambridge University Press, New York (1996). (Cited on pages 71 and 72.)

[125] A. Vecchio et al., *Phys. Rev. Lett.*, **95**, 061102 (2005).

[126] S. Futatani, S. Benkadda, and D. del-Castillo-Negrete, *Physics of Plasmas*, **16**, 042506 (2009).

[127] A. Vecchio et al. *Solar Physics*2292005359.

[128] V. Carbone et al. *Astron. Astrophys.*3812002265.

[129] P.D. Mininni, D.O. Goméz, and G.B. Mindlin, *Phys. Rev. Lett.*, **89**, 061101 (2002).

[130] M.F.A. Azez and A.F. Vakakis, *Journal of Sound and Vibration*, **240**, 859 (2001).

[131] A. Vecchio et al., *Solar Phys.*, **251**, 163 (2008).

[132] P.J.E. Vermeulen and D.P. Casasent, *Optical Eng.*, **30**, 415 (1991).

[133] S.B. Pope, *Turbulent Flows*, Cambridge University Press (2000). (Cited on pages 73 and 74.)

[134] V. Carbone and P. Veltri, *Geophys. and Astrophys. Fl. Dyn.*, **52**, 153 (1990). (Cited on page 73.)

[135] H. Tennekes and J. L. Lumley, *A first course in Turbulence*, MIT Boston (1972). (Cited on pages 79 and 112.)

[136] R. H. Kraichnan, *J. Fluid Mech.*, **5**, 497 (1959). (Cited on page 80.)

[137] F.carbone et al., Phys. Rev. Lett, submitted (2010). (Cited on page 79.)

[138] S. Chen, R. Kraichnan, *Phys. Fluids A*, **1**, 2019 (1989);
M. Nelkin, M. Tabor, *Phys. Fluids A*, **2**, 81 (1990);
V. Yakhot, S.A. Orszag, *Z.-S. She, Phys. Fluids A*, **1**, 184 (1989). (Cited on page 81.)

[139] T. Sanada, V. Shanmugasundaram, *Phys. Fluids*, **4**, 1245 (1992);
W.D. McComb, V. Shanmugasundaram, P. Hutchinson, J. *Fluid Mech.*, **208**, 91 (1989). (Cited on page 81.)

[140] G. Comte-Bellot, S. Corrsin, *J. Fluid Mech.*, **48**, 273 (1971);
S.A. Orszag, G.S. Patterson, *Phys. Rev. Lett.*, **28**, 76 (1972);
C.W. Van Atta, J.C. Wyngaard, *J. Fluid Mech.*, **72**, 673 (1975). (Cited on page 81.)

[141] A.N. Kolmogorov, *C. R. Acad. Sci. U.R.S.S.*, **36**, 301 (1941). (Cited on page 80.)

[142] Y. Zhou, W.H. Matthaeus, P. Dmitruk, *Rev. Mod. Phys.*, **76**, 1015 (2004);
W.H. Matthaeus, Bieber J.W., *Solar Wind Nine*, Ed. S.R. Habbal, R. Esser, J.V. Hollweg and P.A. Isenberg, AIP, 515 (1999). (Cited on pages 79, 80, and 81.)

[143] F. Carbone et al., *EPL*, submitted (2010). (Cited on pages 81 and 83.)

[144] H. Miike et al., *Phys. Rev A*, **31**, 2756 (1985). (Cited on page 84.)

[145] S. Kai et al., *J. Phys. Soc. Jpn.* **38**, 1789 (1975). (Cited on page 84.)

[146] S. John, *Physics Today*, **44**, 32 (1991). (Cited on page 87.)

[147] Y. Kuga, A. Ishimaru, textitJ. Opt. Soc. Am., **A1**, 831 (1984). (Cited on page 87.)

[148] G. Maret and P. Wolf, *Phys. Rev. Lett.*, **55**, 2696 (1985). (Cited on page 87.)

[149] R. L. Liboff, *Kinetic Theory Classical, Quantum, and Relativistic Descriptions*, Prentice Hall, Englewood Cliffs, NJ (1990). (Cited on page 87.)

[150] P. Wolf, G. Maret, E. Akkermans, and R. Maynard, *J. Phys. Fr.*, **49**, 63 (1988). (Cited on page 90.)

[151] M. van Albada, M. van der Mark, and A. Lagendijk, *Phys. Rev. Lett.*, **58**, 361 (1987). (Cited on page 90.)

[152] P. Saulnier and G. W atson, *Optics Lett.*, **17**, 1 (1992). (Cited on page 90.)

[153] P. W. Anderson,*Phys. Rev.*, **109**, 1492 (1958).

[154] F. C. Mackintosh, S. John,*Phys. Rev. B*, **37**, 1884 (1998).

[155] D. S. Wiersma, M. P. van Albada, B. A. van Tiggelen, and A. Lagendijk, *Phys. Rev. Lett.*, **74**, 4193 (1995).

[156] H. K. M. Vithana, L. Asfaw, and D. L. Johnson, *Phys. Rev. Lett.*, **23**, 3561 (1993). (Cited on pages 91 and 94.)

[157] L. V. Kuzmin, V. P. Romanov, and L. A. Zubkov, *Phys. Rev. E*, **54**, 6798 (1996).

[158] N. Scaramuzza, C. Versace, V. Carbone, *Mol. Cryst. Liq. Cryst.*, **266**, 85 (1995).

[159] S. Kai, M. Andoh, and S. Yamaguchi, *Phys. Rev. A*, **46**, R7375 (1992).

[160] S. Nasuno, O. Sasaki, S. Kai, and W. Zimmermann, *Phys. Rev. A*, **46**, 4954 (1992).

[161] G. Strangi, C. Versace, N. Scaramuzza, D. E. Lucchetta, V. Carbone, and R. Bartolino, *Phys. Rev. E*, **59**, 5523 (1999). (Cited on page 91.)

[162] P. E. Wolf, and G. Maret, *Phys. Rev. Lett.*, **55**, 2696 (1985). (Cited on page 91.)

[163] C. Vena, C. Versace, G. Strangi, V. Bruno, N. Scaramuzza, R. Bartolino, Mol. Cryst. Liq. Cryst., **441**, 1 (2005). (Cited on page 91.)

[164] C. Vena, C. Versace, G. Strangi, S. D'Elia, R. Bartolino, Opt. Exp., **15 issue 25** 17063 (2007). (Cited on page 91.)

[165] D. S. Wiersma, *Light in strongly scattering and amplifying random media* (PhD thesis, 1995). (Cited on pages 92 and 93.)

[166] A. Joets, R. Ribotta, *J. Phys.*, **4**, 1013 (1994). (Cited on page 93.)

[167] R. Narashima, *Whither Turbulence? Turbulence at the Crossroads*, Springer, New York (1990). (Cited on page 103.)

[168] R. Temam, *Infinite Dimensional Dynamical Systems in Mechanics and Physics*, Springer, New York (1988). (Cited on page 108.)

[169] N. Aubry, W. L. Lian and E. S. Titi, *J. on Sci. Comput.*, **14**, 483 (1993). (Cited on page 110.)

[170] L. Sirovich, *Quarterly of Applied Math.*, **XLV(3)**, 561 (1987). (Cited on page 110.)

[171] J. Jimenez and P. Monin, *J. Fluid Mech.*, **225**, 213 (1991). (Cited on page 110.)

[172] W. Feller, *An Introduction to Probability Theory and its Applications*, Wiley, New York (1957). (Cited on page 110.)

[173] C. Foias, O. Manley and L. Sirovich, *J. Fluid Mech.*, **198**, 27 (1989). (Cited on pages 111, 112, and 113.)

[174] N. Aubry, R. Guyonnet and L. Lima, *J. Stat. Phys.*, **64(3/4)**, 683 (1991). (Cited on page 112.)

[175] L. Sirovich, *Physica D*, **37**, 126 (1989). (Cited on page 112.)

[176] F. Takens, *Dynamical Systems and Turbulence*, Springer, New York (1981). (Cited on page 112.)

[177] R. Mane, *Ergodic Theory and Differentiable Dynamics*, Springer, New York (1987). (Cited on page 112.)

[178] G. Berkooz, *Turbulece, Coherent Structures, and Low Dimensional Models*, Ph.D. Thesis. (Cited on pages 112 and 113.)

[179] K. Promislow, *Nonlinear Analysis: Theory, Methods and applications*, **16(11)**, 959 (1991). (Cited on page 112.)

[180] P. Constantin and C. Foias, *Navier-Stokes Equations*, Chicago University Press, Chicago (1988). (Cited on page 113.)

[181] C. Foias and R. Temam, *J. Functional Anal*, **87**, 359 (1989). (Cited on page 113.)

[182] L. Sirovich and B. W. Knight, *Proc. Nat. Acad. Sci.*, **82**, 8275 (1985). (Cited on page 113.)